Design and Simulated Performance of the Level 1 Trigger System for the BaBar CP Violation Experiment

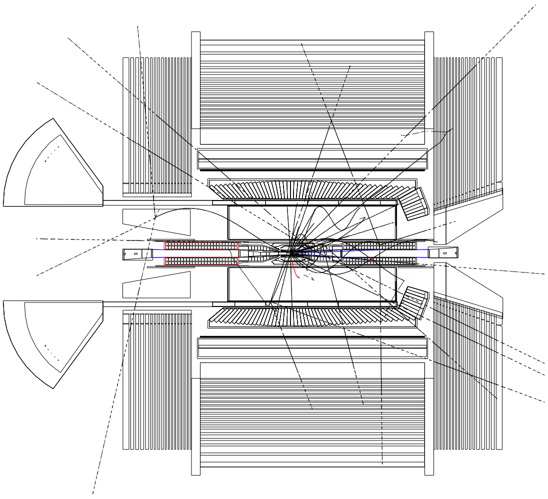

Diplomarbeit (Thesis) Submitted by
Stefan K. Gehrig

Physics Division
Lawrence Berkeley National Laboratory

February 1997

Abstract

In this thesis the results of a complete simulation model of the Level 1 hardware trigger system for the *BaBar* detector are presented.

The Level 1 trigger system must meet three primary requirements. First, a very high efficiency on all $B\overline{B}$ events is crucial, since measuring CP violation at the $\Upsilon(4S)$ resonance with the asymmetric e^+e^- collider PEP-II is the ultimate goal of the *BaBar* detector. Second, the event time has to be reconstructed in the Level 1 trigger, due to the high beam crossing rate at the PEP-II collider ring and the lack of a fast detector element for signaling an annihilation. Last, a trigger rate of less than 2 kHz under all running conditions is required due to the limited data bandwidth of the data acquisition system.

The Level 1 trigger logic was modeled in full detail in a Monte Carlo Simulation, including spatial and temporal correlations of the trigger inputs from the calorimeter and the drift chamber. Efficiency, rate and event time jitter results were obtained on data sets of physics benchmark processes and background processes passed through the *BaBar* GEANT simulation.

The total Level 1 trigger rate from all sources was kept below the required 2 kHz, even under the worst-case background conditions, while maintaining a trigger efficiency of more than 99% for $B^0\overline{B}^0$ CP physics benchmark events after detector fiducial cuts. The event time jitter for inclusive $B^0\overline{B}^0$ events is 181 ns, significantly below the 1 μs specification imposed by the electronics design of the detector subsystems.

These results, together with other results on B^+B^-, $\tau^+\tau^-$ and $\gamma\gamma$ physics presented here, validate the conceptual design of the Level 1 trigger. The Level 1 trigger hardware is scheduled to be installed in 1998.

Acknowledgements

I would like to thank my advisor, Fred Kral, for ample guidance, valuable advice and productive discussions during my year at Lawrence Berkeley National Laboratory. Special thanks also to my supervisor in Germany, Prof. Gerhard Wagner, who made it possible for me to write my thesis abroad. Additionally, I express my gratitude to my supervisor in America, Dr. Morris Pripstein, who initiated this project and also took care of a lot of the paperwork involved.

There were many more people contributing to this thesis. Thanks to the whole *BaBar* collaboration for supplying a great platform to write my thesis on. Especially I would like to thank Alex Montgomery for working with me, coding up large pieces of the simulation used, and also supplying some preliminary graphs for this thesis. Furthermore thanks to Mike Levi, Natalie Roe, Richard Jared, Mike Ronan, Paul Dauncey and Gerry Lynch for their valuable input. Many more contributed but are too numerous to list.

Special thanks to Armin Karcher who helped me a lot getting started, both at work and after work. I also like to thank my roommate, Damica Zemault, for her company, for her mental support, and for having a meal ready for me right after work. Furthermore I like to thank Kerstin Becker and Joel Brown for making this year enjoyable also from a non-physics perspective. Thanks to all the other people I met and got acquainted with during this year.

Last, but not least, thanks to my family and my personal friends in Germany who did not forget about me and kept in touch. Special thanks to Elisabeth Mentler, who supported me on this project, in person when visiting, and via phone or letter from Germany. Also thanks to my e-mailing friends, especially Thomas Weber, Alexandra Schäfke, and Angela Fischer-Brunkow.

Contents

List of Tables

List of Figures

Chapter 1

Introduction

1.1 Introduction to the *BABAR* Experiment

The main goal of the *BABAR* experiment[1] is to measure *CP* violation in the neutral B meson system, which ultimately might explain the imbalance of matter and antimatter in the universe [Nir 92b]. Running at the asymmetric PEP-II e^+e^- collider ring in Stanford, California, *BABAR* is scheduled to begin taking data in 1998. The *BABAR* collaboration consists of about 500 collaborators at 70 institutions in 10 countries. Similar efforts are undertaken by the BELLE collaboration in Japan [BELLE 95].

The long lifetime of the neutral B mesons [MAC 87] and the large B^0 -$\overline{B}^0$ mixing [UA1 87] make it possible to study *CP* violation in this system. In order to discriminate B^0 from $\overline{B}^0$ one needs to determine the decay vertices very accurately. Hence an asymmetric collision is needed which boosts the particles so their decay distance becomes measurable with current techniques. Additionally, a very high luminosity for the accelerator is required to gather enough statistics for the *CP* decay modes in a reasonable timescale.

The Standard Model of Particle Physics explains *CP* violation as a phase in the Cabbibo-Kobayashi-Maskawi (CKM) matrix. Further constraining the parameters of the CKM matrix will put stringent tests on the Standard Model. This might also reveal evidence of physics beyond the Standard Model in case of discrepancies between predictions and measurements.

1.2 Introduction to *CP* Violation

CP violation is one of the most intriguing aspects of high-energy physics today. So far there is only experimental evidence for *CP* violation in the neutral K meson system [Christenson 64]. Theoretical physics provides both interpretations of *CP* violation within the Standard Model and beyond the Standard Model. The *BABAR* experiment aims to measure the *CP* violation

---

[1] The name of the experiment is derived from the fact that the mesons of interest, B and $\overline{B}$ (pronounced “bee” and “bee-bar”), resemble the name of an elephant in a children’s books series.

parameters for the neutral B meson system. By limiting the parameters for the unitarity triangle, one can put stringent tests on the Standard Model.

1.2.1 Theoretical Background on *CP* Violation

Only *CP* violation in the neutral B meson system is discussed here. A more general treatment of *CP* violation is extremely complicated and not very illuminating. The two neutral B mesons have very similar lifetimes as opposed to the two neutral kaons. However, the neutral B mesons differ in mass: One can define [Nir 92a]

$$|B_1\rangle = |B_L\rangle, |B_2\rangle = |B_H\rangle, \tag{1.1}$$

$$\Delta M = M_H - M_L > 0, \tag{1.2}$$

$$M = (M_H + M_L)/2, \tag{1.3}$$

where L and H stand for Light and Heavy, respectively. The two mass eigenstates of the neutral B meson system can be written as:

$$|B_L\rangle = p|B^0\rangle + q|\overline{B}^0\rangle, \tag{1.4}$$

$$|B_H\rangle = p|B^0\rangle - q|\overline{B}^0\rangle. \tag{1.5}$$

The mixing occurs in so-called box diagrams as depicted in Figure 1.1. Defining the decay amplitudes

$$A = \langle f_{CP}|B^0\rangle, \ \overline{A} = \langle f_{CP}|\overline{B}^0\rangle, \tag{1.6}$$

where f_{CP} denotes a final *CP* eigenstate, one can identify three types of *CP* violation in meson decays:

$$|\overline{A}/A| \neq 1 \Rightarrow CP \text{ violation in decay} \tag{1.7}$$

$$|q/p| \neq 1 \Rightarrow CP \text{ violation in mixing} \tag{1.8}$$

$$\lambda = \frac{q}{p}\frac{\overline{A}}{A}, |\lambda| = 1, Im\lambda \neq 0 \Rightarrow CP \text{ violation in the interference of decay and mixing.} \tag{1.9}$$

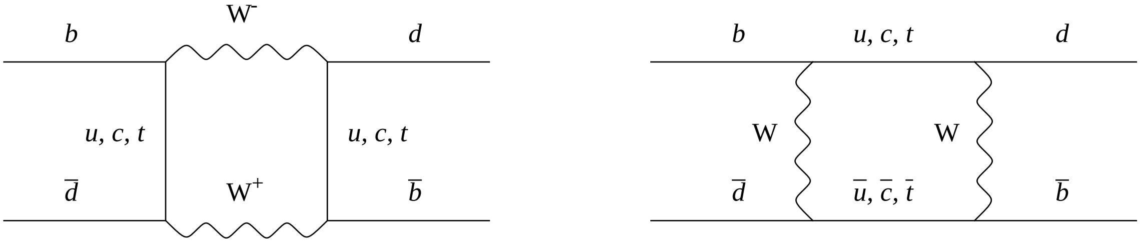

Figure 1.1: Mixing diagrams (box diagrams) for B^0 -$\overline{B}^0$ mixing ($\overline{B}^0 \rightarrow B^0$).

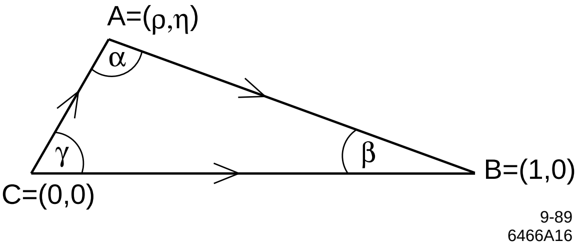

Figure 1.2: The unitarity triangle.

CP violation in decay has not been observed yet. The *CP* violation in the neutral K system represents *CP* violation in mixing, whereas in the neutral B system, *CP* violation in the interference of decay and mixing is expected to be found. From the time evolution of an initially pure B^0 eigenstate one can calculate the probability for an initial B^0 to decay as a $\overline{B}^0$ to be

$$P(t) = \frac{1}{2} e^{-\Gamma t}(1 - \cos(\Delta M t)), \tag{1.10}$$

where $|p/q| = 1$ and the same decay width Γ for B^0 and $\overline{B}^0$ is used. This simple time dependence also requires the dominance of a single weak phase. Likely *CP* decay modes for the discovery of *CP* violation are $J/\psi K_S^0$, D^+D^-, $\pi^+\pi^-$, and $\phi\ K_S^0$.

1.2.2 *CP* Violation in the Standard Model

CP violation would manifest itself in the Standard Model as a phase to the CKM matrix that describes the weak couplings in the three generation Standard Model, expressed in the basis of $-1/3$ charged quark mass eigenstates. The unitary matrix can be written as

$$\begin{pmatrix} d' \\ s' \\ b' \end{pmatrix} = \begin{pmatrix} V_{ud} & V_{us} & V_{ub} \\ V_{cd} & V_{cs} & V_{cb} \\ V_{td} & V_{ts} & V_{tb} \end{pmatrix} \begin{pmatrix} d \\ s \\ b \end{pmatrix} \tag{1.11}$$

Current values of the CKM matrix can be found in [PDG 96]. The unitarity triangle (see Figure 1.2) is a simple geometrical representation of relationships which result from the unitarity of the CKM matrix, e.g.

$$V_{ud}V_{ub}^* + V_{cd}V_{cb}^* + V_{td}V_{tb}^* = 0. \tag{1.12}$$

The triangle represents the equation in the complex plane with one side rescaled to one. The three angles of this triangle are labeled

$$\alpha = arg(-\frac{V_{td}V_{tb}^*}{V_{ud}V_{ub}^*}),\ \beta = arg(-\frac{V_{cd}V_{cb}^*}{V_{td}V_{tb}^*}),\ \text{and}\ \gamma = arg(-\frac{V_{ud}V_{ub}^*}{V_{cd}V_{cb}^*}). \tag{1.13}$$

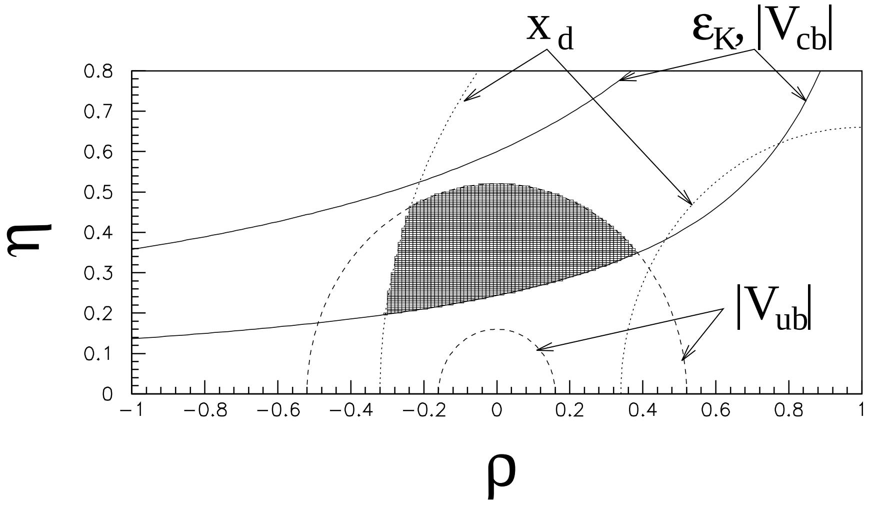

Figure 1.3: Constraints in the Standard Model in the $\rho\eta$ plane. The shaded area corresponds to that allowed for the apex of the rescaled unitarity triangle.

The main goal of BaBar is to measure and overdetermine the quantities of the unitarity triangle, thereby probing the Standard Model. According to the current knowledge of the quantities V_{ij} one can already restrict their values and give a valid range [TDR 95]. Figure 1.3 shows possible ranges of values for ρ and η, the coordinates of the unitarity triangle apex.

There are several theories of *CP* violation beyond the Standard Model but since the Standard Model is still consistent with all observations so far, their description is beyond the scope of this brief introduction.

1.2.3 Measuring *CP* Violation

To measure *CP* violation in the B meson system, BaBar makes use of the relatively long lifetime (1.56 ps [PDG 96]) of the B^0 meson. One B^0 meson is tagged, i.e. unambiguously identified as either B^0 or $\overline{B}^0$, by its decay products (typically a μ,e, or K). The other B^0 meson is required to be the antiparticle due to the quantum numbers of the parent $\Upsilon(4S)$ at the instant of the decay of the first B^0. By looking at the spatial distance between the two particle decay vertices, one can calculate the time difference of the decay, provided a good spatial resolution. With the known time dependence of B^0 -$\overline{B}^0$ mixing (see Equation 1.10), it is possible to determine whether the later decaying particle underwent an inversion of particle type or not. The same equation applies with negative t, when the first particle decays to a *CP* eigenstate and the second to a tagging state. Determination of the decay sequence is crucial; otherwise the asymmetry disappears. In order to measure the time difference of the two decays using distance information with current techniques, it is necessary to build an asymmetric B factory which boosts the particles and allows them to move with almost the speed of light.

CP violation is then established by having different counts for B^0 and $\overline{B}^0$ for *CP* decay channels, i.e. decays into *CP* eigenstates. This can be quantified with the time-dependent asymmetry relation

$$A(B \rightarrow \ f_{CP}, t) = \frac{\Gamma[\overline{B}^0(t) \rightarrow \ f_{CP}] - \Gamma[B^0(t) \rightarrow \ f_{CP}]}{\Gamma[\overline{B}^0(t) \rightarrow \ f_{CP}] + \Gamma[B^0(t) \rightarrow \ f_{CP}]} = \mathrm{Im}\lambda \ \mathrm{sin}\Delta\mathrm{Mt}, \tag{1.14}$$

where Γ denotes branching ratios and f_{CP} denotes a final *CP* eigenstate.

CP eigenstates have eigenvalues for the *CP* operator of either $+1$ or -1. Typical tagging modes are semileptonic decays with $B^0 \ \rightarrow \ l^+X$ or $\overline{B}^0 \ \rightarrow \ l^-X$, where l denotes any lepton. Other tagging modes use kaons. A more detailed description on measuring *CP* violation can be found in [Burchat 91].

1.3 Other Physics Studies at the *BABAR* Experiment

An asymmetric B factory with a detector system that has excellent spatial, momentum and energy resolution is suitable for a great variety of interesting physics. Running on the resonance energy $\Upsilon(4S)$ with the anticipated luminosity enables studies of various physics processes (see Table 1.1). Due to the high statistics of B decays, *BaBar* can improve the branching ratio determinations for B decay modes. Searches for rare B decays are also possible.

Of the physics processes listed in Table 1.1, the τ decays are of special interest besides the B decays. Searches for rare τ decays with the luminosity of PEP-II will become competitive. Determination of branching ratios and asymmetries for τ decays to a high accuracy can be achieved due to the high statistics of events. Lorentz structure measurements, e.g. V-A tests, can be performed by measuring correlations (e.g. spin correlations) between the two decay products of the taus.

Charm physics will also contribute to the rich physics program. Two-photon physics studies beyond invariant masses of 2 GeV/c^2 become possible as well, which is a not so well investigated area yet.

1.4 Triggering on All Physics Processes

Modern collider experiments would yield an unmanageable amount of data if they recorded all detector responses continually. Therefore these systems have a trigger system selecting the physics events of interest and discarding the rest. The main challenge of the trigger lies in an effective discrimination of physics events against background events. Only the triggered data will be kept for further processing. High trigger efficiency on physics of interest is desirable, but, at the same time, as few background events as possible should be recorded.

Trigger decisions have to be made quickly to avoid buffering too much data. Buffering is necessary because the data might include an event of interest. Therefore the first trigger

Process	cut	cross section σ [nb]	trigger rate [Hz]
$B\overline{B}$ events	-	1.2	4
$\tau^+\tau^-$ events	-	0.8	2
$\mu^+\mu^-$ events	-	0.8	2
$q\overline{q}$ events	-	2.8	8
Bhabhas	$\theta > 17°$	44	132
$\gamma\gamma$ signal events	$\theta > 17°$	2.4	3
$\gamma\gamma$ background	$\theta > 17°, p_{\mathrm{t}} > 0.1\,\mathrm{GeV}/c$	15	45

Table 1.1: Cross sections of processes at the $\Upsilon(4S)$ resonance. Listed are all processes that contribute to the trigger rate originating from the interaction point. The quoted trigger rate corresponds to a luminosity of $3 \cdot 10^{33} cm^{-2} s^{-1}$ and might be lower than $\sigma \cdot 3\frac{\mathrm{Hz}}{\mathrm{nb}}$ due to untriggered events. Bhabha and $\gamma\gamma$ events are expected to be prescaled before being recorded. Listed cross sections can be found in [BELLE 95]. The $\gamma\gamma$ background cross section estimate differs slightly from the rate prediction for the BaBar experiment (50 Hz), where the BaBar rate estimate uses trigger rates from earlier experiments at PEP scaled by the change in luminosity.

algorithms usually operate massively parallel in hardware (see e.g. [H1 92]), like the Level 1 trigger in the BaBar experiment. For BaBar only about 20 Hz of “interesting” physics events is expected due to the relatively small cross sections (see Table 1.1), while the beam crossing rate is 238 MHz. Trigger decisions are based on a subset of detector data that has to be analyzed quickly. In the case of BaBar, a drift chamber and a calorimeter transmit data to the trigger. The BaBar trigger system has to be capable of triggering on **all** physics processes while keeping triggers on background events low.

This thesis mainly describes the lowest level trigger system, the Level 1 hardware trigger, for the BaBar detector. An overview of the physics program that is accessible with the BaBar detector is given in this chapter. The detector components are introduced in Chapter 2. The requirements for the BaBar trigger system and the strategies how to meet them are detailed in Chapter 3. The event simulation method used here to verify the performance of the trigger is explained in Chapter 4. The trigger algorithms of the Level 1 trigger system are described next, with focus on drift chamber and global trigger algorithms in this thesis. Chapter 5 describes the drift chamber trigger algorithms, including some simulation results leading to specific choices of trigger algorithms, and Chapter 6 describes the global trigger algorithms. Chapter 7 shows the simulation results using the algorithms that were identified to be the most suitable in the previous chapters. These results led to the approval of the current electronics implementation model of the Level 1 trigger by meeting all requirements set forth to ensure efficient data taking.

Chapter 2

The *BABAR* Detector

2.1 Overview

The BaBar detector has to yield excellent spatial, momentum and energy resolution and has to operate in the asymmetric e^+e^- collider PEP-II with luminosities up to $10^{34} cm^{-2} s^{-1}$. To meet these requirements BaBar consists of a silicon vertex tracker next to the beam pipe for vertex determination, a drift chamber and a superconducting solenoid for momentum determination, a Cherenkov detector for particle identification, a calorimeter for energy determination, and a muon and neutral hadron detector for particles that pass through the calorimeter. The solenoid produces a 1.5 T magnetic field for the inner detector components.

Figure 2.1 shows a cross-sectional view of the detector. The BaBar coordinate system is a right-handed orthonormal system with its origin at the interaction point. The positive z direction points in the direction of the high-energy beam. θ and ϕ are the polar and azimuthal angles, respectively. The x direction points away from the center of the e^+e^- collider ring and the y direction points upward.

2.2 The Asymmetric e^+e^- Collider Ring

The BaBar experiment runs at the asymmetric e^+e^- collider ring PEP-II at the Stanford Linear Accelerator Center (SLAC). The high-energy beam of electrons is operated at 9.0 GeV and the low-energy beam of positrons is operated at 3.1 GeV. This yields a center-of-mass energy of 10.58 GeV which corresponds to the mass of the $\Upsilon(4S)$ resonance. The asymmetric energies produce a particle boost in the forward direction of $\beta\gamma = 0.56$. The polar angle of 90° for photons in the center-of-mass frame corresponds to an angle of 60° in the laboratory frame. The time between two beam crossings is 4.2 ns which makes e^+e^- annihilation essentially continuous from the view point of the detector electronics.

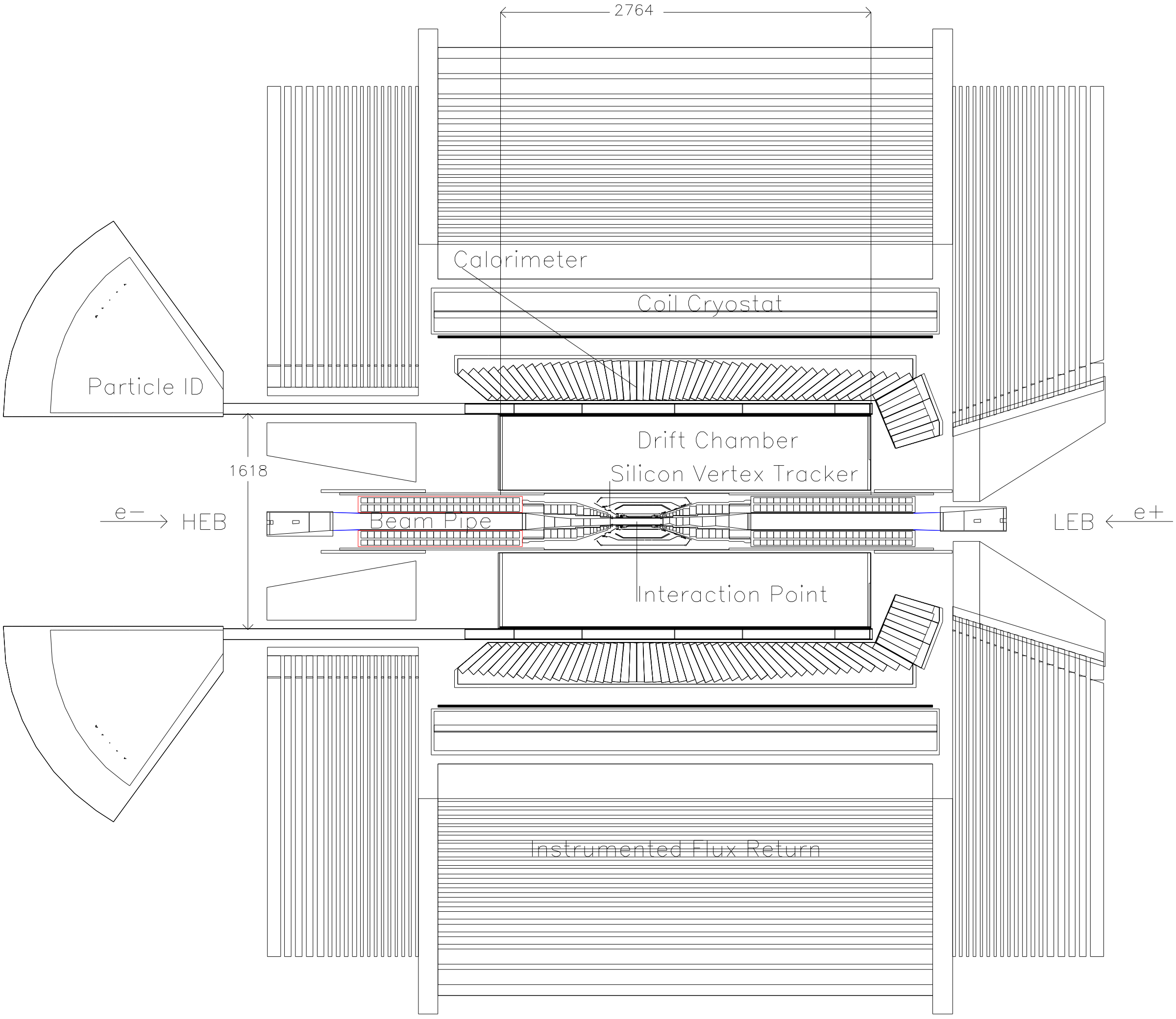

Figure 2.1: x-z view of the BaBar detector. high-energy electron beam comes from the left, low-energy positron beam from the right.

2.3 Silicon Vertex Tracker

The silicon vertex tracker is needed to measure the decay vertices of the two neutral B mesons to a high accuracy. In addition, it is the main tracking element for particles below $100\,\mathrm{MeV}/c$ momentum transverse to the beam direction. With a boost of the center-of-mass system of $\beta\gamma = 0.56$ and the mean lifetime of the neutral B mesons of about $200\,\mu\mathrm{m}$, a vertex resolution of $80\,\mu\mathrm{m}$ is desired. The silicon vertex tracker consists of 5 layers of double-sided silicon microstrip detectors. It covers polar angles between 17 and 150°. The readout electronics is placed outside these polar angle limits. The silicon vertex tracker registers electron-hole pairs that are produced by a charged particle traversing the diodes of the silicon microstrip detector.

2.4 Drift Chamber

Since the drift chamber information is used extensively in this thesis, the drift chamber is described in more detail.

2.4.1 Drift Chamber Functions and Requirements

The main tasks for the drift chamber are momentum determination and pattern recognition. A very good momentum resolution is desirable for efficiently reconstructing B^0 decays. Moreover, the pulse height information from drift chamber signals is used to measure the mean ionization loss (dE/dx), which helps discriminating kaons from pions at low momentum.

In a drift chamber, sense wires are at a positive potential in a gaseous surrounding. When a charged particle traverses the chamber, particles of the gas become ionized and travel toward these wires. On their way they ionize more electrons (provided the electric field is strong enough) and cause an avalanche that can be sensed as an electrical current. Field wires around the sense wires in the drift chamber shape the electric field to make it uniform. Then precise measurements of the drift time, combined with the sense wire signals, yield a good spatial resolution. A small-cell, low-mass drift chamber minimizes multiple scattering and hence performance degradation in the drift chamber and in the outer detectors.

2.4.2 Drift Chamber Geometry

The *BaBar* drift chamber is 280 cm in length, and occupies the radial space between 23 and 80 cm. Forty layers of sense wires fill this volume of 7104 drift cells. The 40 layers are grouped in 10 superlayers with four layers each. Superlayers differ in wire orientation. Axial superlayers are parallel to the beam, whereas stereo superlayers are at a small angle ($< 10°$) to the beam to enable a determination of the z-position. Wire orientation alternates per superlayer, beginning with axial superlayer 1, positive-stereo superlayer 2, negative-stereo superlayer 3, axial superlayer 4 and so on. Table 2.1 shows the numbers of cells per layers in the drift chamber and their orientation. Figure 2.2 depicts the drift chamber cross-sectional view. The drift chamber exhibits a 16-fold rotational symmetry in the x-y plane. The trigger further subdivides every sixteenth of a superlayer into two supercells, leading to 32 supercells per superlayer. One of the drift chamber wedges with its wire pattern is pictured in Figure 2.3 in the x-y view. Note that consecutive layers are staggered by a half cell.

The drift chamber cells have either a hexagonal (center layers) or pentagonal (outer layers) shaped field and the maximum drift time in the envisioned operating mode (sense wires at 2025 V) is about 600 ns. Isochrones for a typical BaBar drift cell are shown in Figure 2.4. The 21664 field wires in the drift chamber are made of gold-coated aluminum, whereas the 7104 sense wires are made of tungsten.

SL	Layer	Orientation	Cells/Layer	SL	Layer	Orientation	Cells/Layer
1	1	A	96	6	21	V	192
1	2	A	96	6	22	V	192
1	3	A	96	6	23	V	192
1	4	A	96	6	24	V	192
2	5	U	112	7	25	A	208
2	6	U	112	7	26	A	208
2	7	U	112	7	27	A	208
2	8	U	112	7	28	A	208
3	9	V	128	8	29	U	224
3	10	V	128	8	30	U	224
3	11	V	128	8	31	U	224
3	12	V	128	8	32	U	224
4	13	A	144	9	33	V	240
4	14	A	144	9	34	V	240
4	15	A	144	9	35	V	240
4	16	A	144	9	36	V	240
5	17	U	176	10	37	A	256
5	18	U	176	10	38	A	256
5	19	U	176	10	39	A	256
5	20	U	176	10	40	A	256
				10	40	Total	7104

Table 2.1: Superlayer numbering, layer numbering, number of cells per layer and their orientation. A means axial layer (parallel to the beamline), U means at a positive angle with respect to the beamline, V means at a negative angle.

The drift gas consists of a 80:20 Helium:Isobutane low-mass gas which provides space point resolution of less than $100\,\mu$m with the current geometry. The front-end electronics of the drift chamber is mounted on the rear endplate where the signals for the trigger are produced.

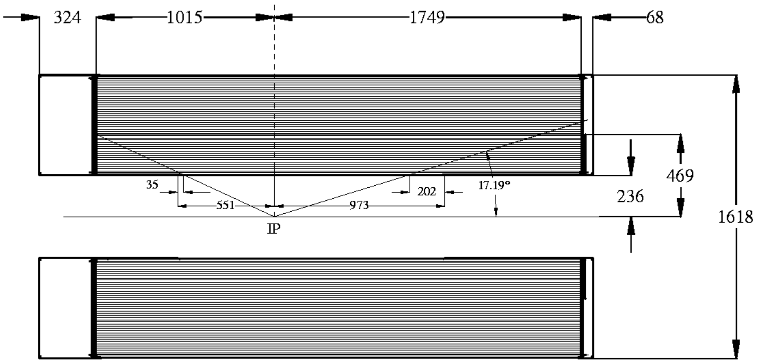

Figure 2.2: Drift chamber geometry in the r-z view. The chamber is offset in z from the interaction point, with more tracking volume in the forward direction to account for the boost.

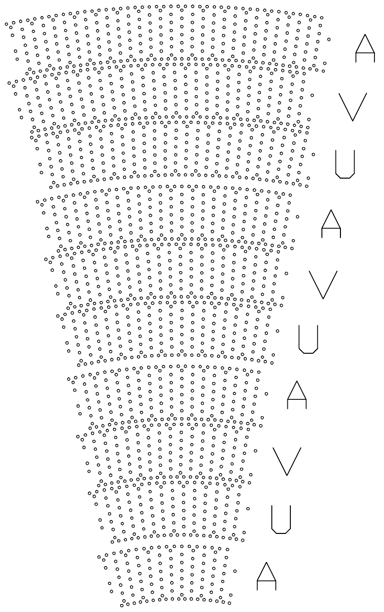

Figure 2.3: Wire pattern of one sixteenth of the drift chamber in the x-y view.

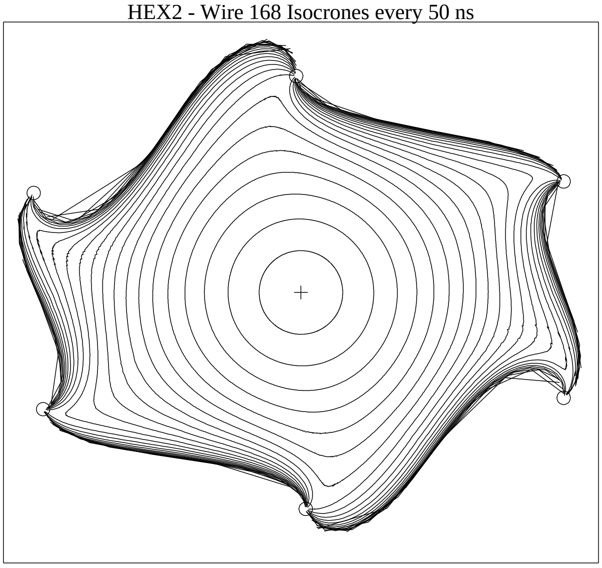

Figure 2.4: Isochrones at a 50 ns increment for a single drift cell in the BaBar drift chamber. The sense wire is at the center surrounded by 6 field wires. The twist is caused by the 1.5T magnetic field parallel to the sense wire.

2.4.3 Drift Distance to Time Relationship

The individual drift cells vary in size, shape and voltage from layer to layer, due to the variation in the geometry of the field and sense wires in different layers. Thus drift cells in different layers have different relationships between drift time and drift distance. In Figure 2.5, the relationship between drift distance and drift time is plotted for three cases: the average of all 40 layers as well as two cases that have large deviations from the average, layer 1 of superlayer U2 and layer 3 of superlayer A4. Note that the drift time can thus vary by as much as 100 ns for large drift distances.

The drift time relationship was obtained from a detailed simulation of the cells of each layer and their analog and digital electronics [Innes 96]. Each signal was compared to a differential FADC comparator[1] that was found to have a Gaussian jitter of 6 ns. The drift times were sampled at a 3.7 MHz frequency and passed to the drift chamber trigger.

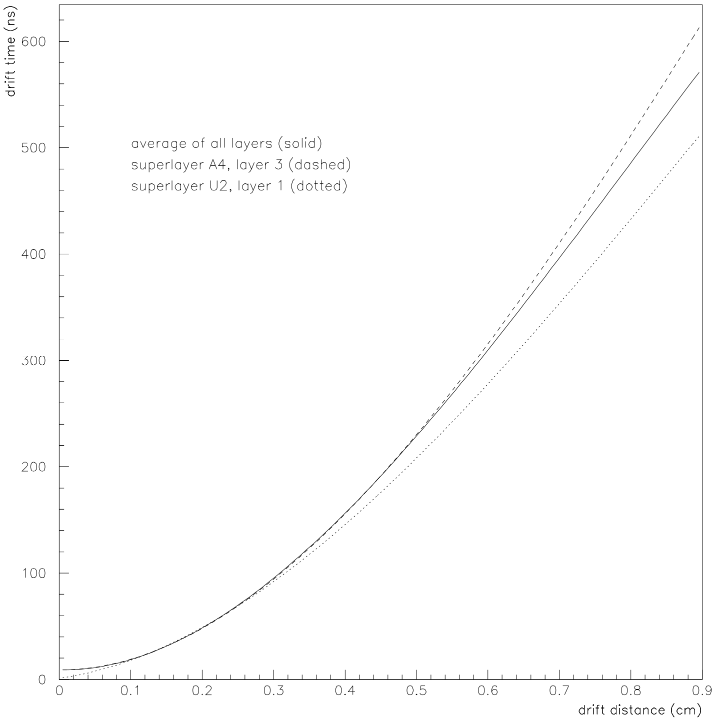

Figure 2.5: Drift time versus drift distance. A plot of the drift time as a function of drift distance for the average of all layers in all superlayers (solid line) as well as for the two layers with the largest deviations from the average, layer 3 of superlayer A4 (dashed) and layer 1 of superlayer U2 (dotted). Above 0.9 cm, the drift time curves saturate at the maximum drift time.

---

[1] The difference between the current sample and the sample that occurred two 67-ns buckets earlier was required to exceed 2 FADC (Flash Analog to Digital Converter) counts.

2.5 Particle Identification System

The particle identification system consists of a Cherenkov counter. This ring-imaging Cherenkov detector is called Detection of Internally Reflected Cherenkov Light (DIRC). Particle identification is necessary to discriminate pions from kaons above 0.7 GeV/c and from protons above 1.3 GeV/c.

When a particle traverses a medium at a speed higher than the speed of light for that medium, it radiates light at an angle of $\theta = \cos^{-1}(1/\beta \mathrm{n})$, where $\beta = v/c$ and n is the refraction index of that medium. Knowing the momentum and the speed, one can extract the rest mass of the particle. The glass bars of the DIRC are located between drift chamber and calorimeter. Photomultiplier tubes are located at the end of a water tank in the backward region of the detector (see Figure 2.1).

2.6 Calorimeter

The electromagnetic calorimeter (EMC) consists of a cylindrical barrel section and a forward conic endcap. The barrel is located directly outside the DIRC. The main material in front of the calorimeter is the DIRC which covers 0.18 radiation lengths out of 0.23 total. Barrel and endcap combined consist of 6660 CsI(Tl) crystals. Since the photons coming from a π^0 decay show a soft energy spectrum, it is necessary to measure energies down to 20 MeV. On the other hand the crystals were designed in length such that only minimal rear leakage for electrons occur, i.e. more than 16 radiation lengths.

When a charged particle traverses a CsI(Tl) crystal, energy loss via bremsstrahlung occurs. These emitted photons typically undergo pair production and the cycle repeats with the electrons and positrons. The result is an electromagnetic shower along the path of the charged particle. To measure these showers, the light emission of every crystal is read out by two independent silicon photodiodes. Each crystal is wrapped with a reflecting material on its sides.

2.7 Muon and Neutral Hadron Detector

The Instrumented Flux Return (IFR), the muon and neutral hadron detector, uses the flux return iron of the superconducting solenoid as an absorber. It is divided into backward endcap, barrel and forward endcap and consists of 20 iron plate layers of 2 to 5 cm thickness. The active detector elements are Resistive Plate Counters (RPC) that are located in the gaps between the iron plates.

An RPC consists of a gas gap between two Bakelite plates, one connected to ground, the other to 8 kV. If a charged particle traverses the RPC a quenched spark occurs that produces a signal. Neutral hadrons are detected by their charged secondaries via interaction or decay (e.g. K_L^0).

2.8 Electronics

The electronics system includes all front-end, trigger, and data acquisition electronics. The environment of the high-luminosity PEP-II machine poses certain unique challenges to this system [Butler 96]. PEP-II beam crossings occur at a rate of 238 MHz, which, in terms of the response time of the electronics, is essentially continuous, unlike previous e^+e^- colliders. The rate of recorded physics events, on the other hand, will be less than 100 Hz. The trigger system has to determine the interesting time slices to read out by looking at a reduced set of detector data. The high beam crossing rate requires data buffering to avoid deadtime losses while making trigger decisions. To record an event in the *BaBar* experiment, approximately 200,000 signal channels have to be read out (see Table 2.2).

System	Number of Channels
Vertex Detector	140,000
Muon System (IFR)	42,000
DIRC	10,000
Calorimeter	7,000
Drift Chamber	7,000

Table 2.2: Channel count for each detector system.

The actual detector response is recorded with the front-end electronics. The data acquisition system transmits this data to the so-called online farm for further processing if the trigger system has sent an accept signal. The online farm consists of a network of commercial processors to monitor the detector and to perform some of the trigger selection algorithms.

2.8.1 Front-End Electronics

In the *BaBar* nomenclature, the front end is that portion of the electronics from the signal source on the detector through the digitizer. The raw detector signals are appropriately processed and transmitted to the readout modules, which are housed in standard VME crates. The readout modules buffer the data in case the detector-mounted electronics is not equipped with buffers (calorimeter only).

2.8.2 Trigger

The *BaBar* trigger system has a multi-level trigger architecture, which is typical for high luminosity experiments (see e.g. [CLEO 91]). There is no detector signal to indicate an e^+e^- annihilation. So the first level of the trigger system has to select the interesting physics events by using only a subset of the detector information within a short period of time ($12\,\mu$s in *BaBar*) to avoid overwriting the circular buffers of the front-end electronics. The only practical method for delivering a first level trigger signal in less than 12 μs is to use a hardware processor operating on a reduced representation of a subset of the data (trigger primitives). The Level 1 trigger in *BaBar* uses only detector information from drift chamber and calorimeter. Information from the silicon vertex tracker to determine the z-position cannot be used because the data bandwidth to transmit the 140,000 channels of the silicon vertex tracker is too large to be processed in less than 12 μs [Levi 94]. The maximum average acceptance rate for the Level 1 trigger is required to be less than 2 kHz. Hooks for an optional Level 2 trigger performing primary vertex cuts are built into the system in case the Level 1 Accept (L1A) rate is too high for subsequent systems. After the L1A signal all detector buffers are read out (event build). A Level 3 trigger running on commercial processors in the online system refines the selection and further rejects events using software algorithms. The whole trigger process and the data flow are illustrated in Figure 2.6.

2.8.3 Data Acquisition

The readout modules contain large memories. For systems with detector-mounted buffers, these memories store events after the L1A and are used to hold data that are ready for readout. The calorimeter system also uses this memory to buffer data during the Level 1 trigger latency.

The data acquisition system has an event data path, by which all event data pass from the system electronics to the event collection system, and a trigger data path to communicate with the trigger processor. In addition, high-speed clock paths for synchronization and slow control data paths for controlling the process from the online farm are available. The data acquisition interfaces are very similar across the systems. The crates for each detector system have similar readout modules, a fast control distribution module, and a readout controller.

For each event, an event-assembly network moves the approximately 25 kbytes of event data, from the data sources to the Level 3 processor farm. At a Level 1 trigger rate of 2.0 kHz, this technology is expected to be able to transport approximately 50 Mbytes/s of data. This type of technology is easily upgradable and can accommodate the needs of luminosity, trigger processing, and bandwidth upgrades.

The Fast Control System (FCS) supplies the data acquisition system with clocks, strobes, error indications, and other control signals. The *BaBar* clock is set by the accelerator 476 MHz radio frequency signal (exactly twice the beam crossing rate). All other clocks are derived from that signal, e.g. the trigger clock of 7.4 MHz is equivalent to 32 beam crossings. FCS also issues the actual L1A signal based on the trigger word sent by the Level 1 trigger consisting of 30 trigger lines. The individual trigger lines can be prescaled (mostly masked but accepting a predetermined fraction) under high background conditions and the final L1A signal is produced by `OR`-ing all trigger lines after such prescaling.

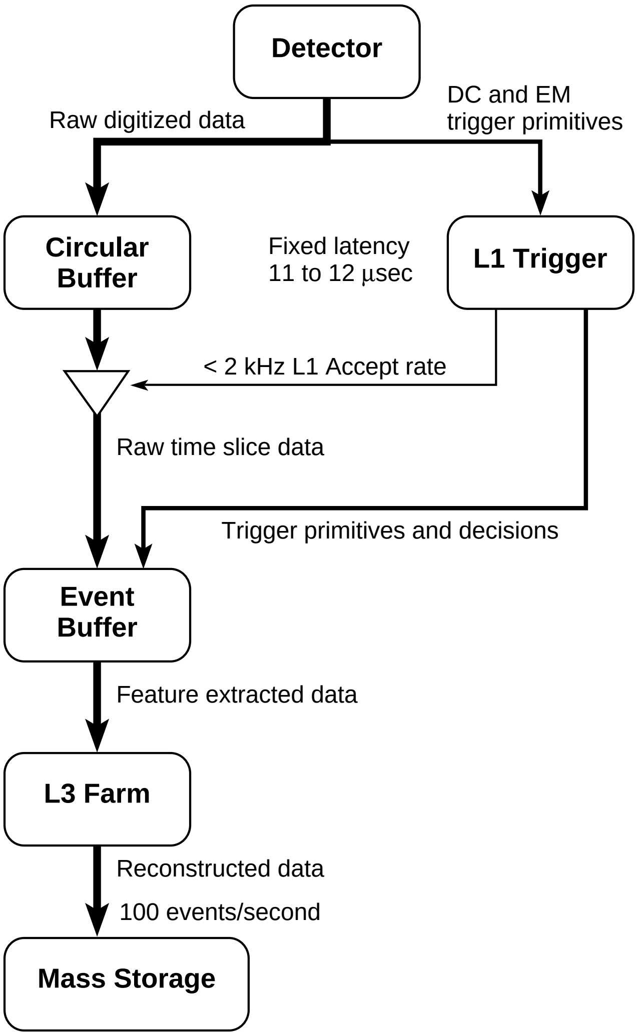

Figure 2.6: Trigger structure and data acquisition data flow, showing levels and buffers. Data to the Level 1 trigger consist of drift chamber and calorimeter trigger primitives. See text for a discussion of Level 2 options.

Chapter 3

The Trigger System

3.1 Overview

This chapter starts by describing the requirements for the BaBar trigger system (see also [Trigger 96, Gehrig 96c]). Next the design to meet these requirements is explained. At the end, the Level 1 trigger components are introduced.

3.2 Trigger System Requirements

The complete trigger system needs to be efficient, selective, measurable, accurate, stable, and flexible. These attributes are necessitated by the requirements for physics analysis and the requirement for trigger rates. The trigger system must also make a fast and accurate determination of the time of the event since there is no fast detector element signaling an e^+e^- annihilation event.

3.2.1 Physics Requirements

The relative importance of the attributes listed above varies for different physics data sets. For asymmetry measurements and searches, it is more important to have a high efficiency rather than a well-known efficiency. For branching ratio and cross-section measurements, precisely measured efficiencies are crucial. The principal trigger requirements for each data set are listed in Table 3.1. In addition to the key physics events, a number of other reference events are recorded for uses such as luminosity determination, detector calibration, beam monitoring, and trigger performance studies. These impose additional requirements on the trigger and are listed at the bottom of the table.

Efficient, Selective: While the primary mission of the BaBar experiment is the study of *CP* violation in B decays, the trigger is designed to select a large number of processes that may be important. Because of their relatively high multiplicities, it is straightforward to achieve high trigger efficiencies for Υ and $c\overline{c}$ events. The challenge for the trigger lies in

Physics Data Samples	Goals
$B\overline{B}$ from the $\Upsilon(4S)$: *CP* Channels	High Efficiency
$B\overline{B}$ from the $\Upsilon(4S)$: Non-*CP* Channels	Precise Efficiency, High Efficiency
B Physics at the $\Upsilon(5S)$	High Efficiency
Charm Physics	Precise Efficiency, High Efficiency
Continuum $q\overline{q}$	Precise Efficiency (Background Subtraction)
τ Physics: Rare Decays & Asymmetries	High Efficiency
τ Physics: Branching Ratios	Precise Efficiency
$\gamma\gamma$	Precise Efficiency

Other Data Samples	Purpose and Comments
Bhabhas: Two Detected Prongs	Luminosity, Calibration, High Efficiency
Bhabhas: One Detected Prong	Calibration, Beam Monitor
$\mu^+\mu^-$	Luminosity, Calibration
Cosmic Rays	Calibration
Beam Backgrounds	Beam Monitor, Trigger Studies
Random Events	Trigger Studies

Table 3.1: Principal trigger goals for each type of data sample.

making the trigger selective enough to trigger on low multiplicity $\tau^+\tau^-$ and $\gamma\gamma$ events, while keeping the rate of accepted background events low. The efficiency requirements for each type of physics data sample are summarized in Table 3.2.

To ensure high efficiencies in offline analysis and to maximize background rejection, trigger algorithms also need to have sharp efficiency turn-on curves. For example, the efficiency as a function of cluster energy should approximate a unit step function as closely as possible to allow a highly selective trigger.

Measurable, Accurate: There are several ways to facilitate precise and accurate offline measurements of the trigger efficiency. First, the geometry of the detector and the readout electronics for each system contributing to the trigger are designed with trigger considerations in mind. Second, the trigger and data acquisition systems are designed to

- use orthogonal selection criteria as much as possible,
- use redundant selection criteria,
- record all useful trigger primitives and decisions for accepted events,
- accept prescaled numbers of events with looser criteria,
- accept a prescaled number of rejected events,
- have a sharp efficiency turn-on as a function of the selection variables, and

Physics Data Samples	ε	$d\varepsilon$	f
$B\overline{B}$ from the $\Upsilon(4S)$: CP Channels	99%	0.5%	1
$B\overline{B}$ from the $\Upsilon(4S)$: Non-CP Channels	99%	0.5%	1
B Physics at the $\Upsilon(5S)$	99%	0.5%	1
Charm Physics	95%	2%	1
Continuum $q\overline{q}$	95%	2%	5
τ Physics: Rare Decays	90%	10%	1
τ Physics: Asymmetries	95%	0.5%	5
τ Physics: Branching Ratios	95%	0.1%	1
$\gamma\gamma$ Physics: Exclusive Meson Pairs	90%	3%	5
$\gamma\gamma$ Physics: All-Neutrals	80%	5%	5
$\gamma\gamma$ Physics: Exotic Resonances	90%	4%	1
$\gamma\gamma$ Physics: Tagged	90%	5%	1

Table 3.2: Principal efficiency requirements for each type of physics data sample. Listed are the minimum efficiency requirement, the efficiency precision ceiling and the maximum tolerable prescale factor.

- be straightforward to model with simulations.

Finally, the online system will be designed so that the recorded trigger primitives and decisions are readily available for offline analysis.

Use of the trigger results for precision physics measurements depends crucially on the trigger system accurately working as a whole. Like the other systems that deliver signals to the data acquisition system, the trigger system is designed with sufficient monitoring, calibration, and diagnostic testing capabilities so that trigger decisions and trigger data are known to be correct.

Stable: To allow measurement of efficiency from the data, stability of efficiencies for some minimum period of time is desired. This is motivated by the need for large enough partial data samples to calculate efficiencies. It also makes it operationally less complicated to do efficiency determination analysis.

Flexible: Because PEP-II machine conditions will vary over the course of the experiment, the trigger needs to be flexible. Under momentary severe background conditions, saturation of the bandwidth should result in deadtime in such a way that a diminished number of whole events are collected rather than a larger set of partial events.

3.2.2 Requirements on Backgrounds and Trigger Rates

In addition to the requirements motivated by physics issues listed above, the total Level 1 trigger output rate — the sum of the rates for the physics and diagnostic processes listed in Table 3.1 and the rates for background processes — must be below 2 kHz. This limit is derived from the limited bandwidth of the data acquisition system.

The main background processes that produce charged tracks traversing the drift chamber and calorimeter are

- physics backgrounds from asymmetric bhabhas with only one detected charged track and two-photon events below $\gamma\gamma$ energies of interest,
- beam-induced backgrounds from hadronic photoproduction interactions of lost beam particles, electromagnetic interactions of lost beam particles,
- beam-gas collisions at the interaction point, and
- cosmic rays.

The main sources of occupancy in the silicon vertex tracker, drift chamber, and calorimeter are

- particles from small-angle radiative Bhabhas, and
- beam-induced background from lost beam particles.

The rates of physics events from e^+e^- annihilation scale with the luminosity, whereas those of beam-induced backgrounds scale with the beam current and the pressure of the residual gas inside the PEP-II beam pipe.

Physics backgrounds are evaluated at the design luminosity of $3 \cdot 10^{33}$ cm^{-2}s^{-1}, and the trigger and data acquisition system must be upgradable for higher luminosities. Because of their variable nature and because of uncertainties in the predictions, beam-induced backgrounds pose more stringent design requirements. The trigger and data acquisition system should not have substantial impact on the physics program as long as data are useful. Based on simulation of the occupancies in the silicon vertex tracker as functions of lost-particle rate, pattern recognition becomes seriously compromised at ten times the nominal background rate.

3.2.3 Requirements on Latency and Jitter

Along with the requirements for trigger efficiencies and rates, the trigger algorithm must also satisfy specifications for latency and jitter. These specifications [Kral 96a] require that the time elapsed between the PEP-II beam crossing that causes a Level 1 Accept to be generated in the Fast Control System for an interesting event and the arrival of that L1A at the input connector of the Readout Module (ROM) be no more than 12 μs (see Figure 3.1). Thus, the trigger algorithms must be sufficiently fast so that when they are implemented in hardware, the total time to trigger on an event is less than this requirement.

In addition, the maximum allowed jitter for the trigger is 1.008 μs. Thus, the signal must arrive at the input connector of the Readout Module between 10.992 and 12 μs after the beam crossing that produced the event of interest, as shown in Figure 3.1 on the right. So the trigger algorithms must be able to determine the time of an event to within this accuracy.

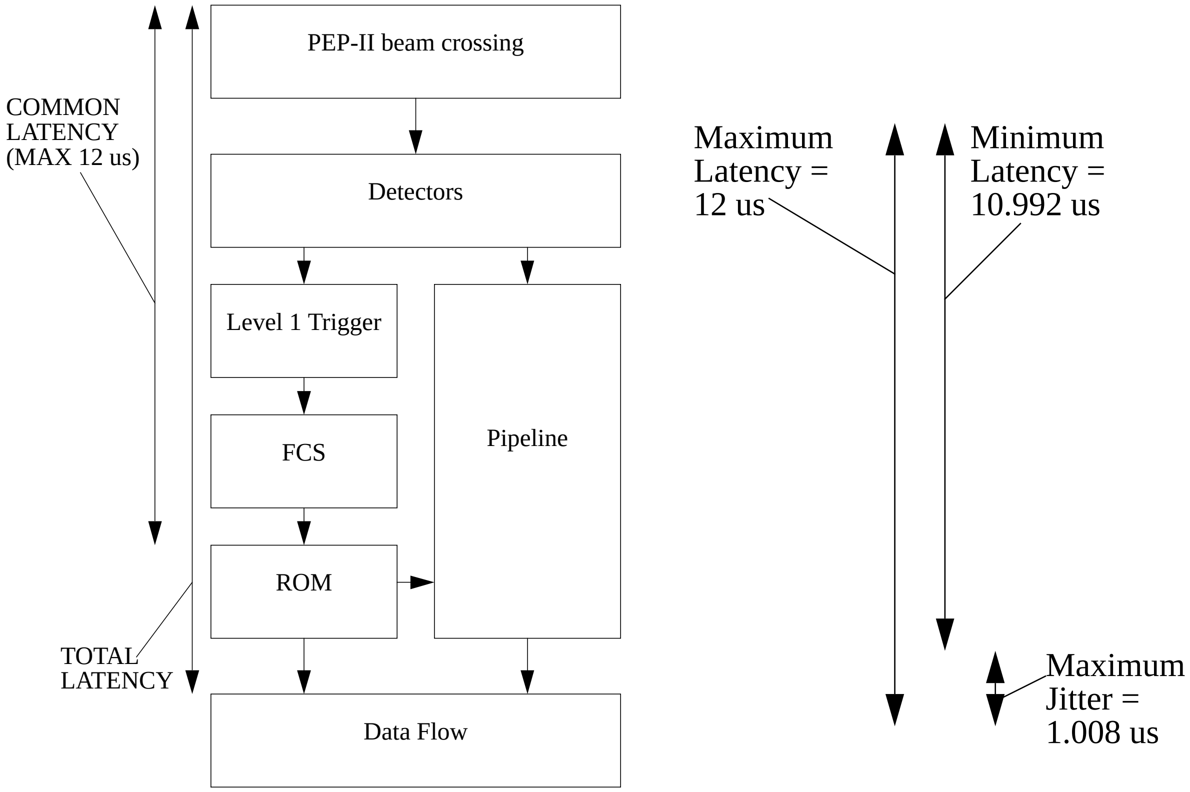

Figure 3.1: Common latency versus total latency for the complete Level 1 system (left). Maximum common latency, minimum latency, and resultant maximum jitter window allowed for the trigger system (right).

3.3 Trigger System Design

3.3.1 Level 1 Trigger Strategy

The Level 1 trigger selects events based on event selection criteria that separate physics events, which have particular event signatures, from background. To do this, the trigger builds trigger objects in the drift chamber and calorimeter, and then combines these objects to form trigger lines. These lines are easily redefinable, and can also be prescaled, in order to improve trigger performance under severe background conditions. Several benchmark processes in the areas of B, τ, and $\gamma\gamma$ physics and for background events in the BaBar detector are identified in this section. These define what trigger lines should be used.

Event Selection Criteria

Event signatures are used to separate signal from background. Combinations of the following global event properties are used in the Level 1 trigger as general event selection criteria:

- charged track multiplicity,
- calorimeter cluster multiplicity, and
- event topology.

At higher trigger levels, a primary cut on the vertex position is performed. These selection criteria have associated thresholds for the following parameters: charged-track transverse momentum (p_{t}), energy of calorimeter clusters (E_{clus}), solid angle separation (ϕ), and track-cluster match quality. The trigger definition can contain selection criteria that differ only by the values of thresholds, such as the E_{clus} threshold values. A small fraction of random beam crossings and events that failed to trigger are also selected for diagnostic purposes.

When these selection criteria alone are not sufficient to reduce the trigger rate below the required value while simultaneously meeting all other requirements (such as when backgrounds are severe but data are useful for physics), further steps can be taken to prevent swamping downstream systems. Prescaling factors can be applied to trigger selection lines to ensure that the available bandwidth is filled with interesting events. Additionally, it is straightforward to change the global logic combinations of event selection criteria in each trigger line, and it is also be possible to vary selection parameters.

Trigger Objects

Table 3.3 lists “trigger objects” which are potentially definable at Level 1 from the event selection criteria and which have been determined to be useful in constructing global trigger definitions. Here only objects from the drift chamber and calorimeter are listed, since vertex detector information is only available at higher levels of the trigger system. For a given trigger level, the global selection filter is a logical `OR` of a number of specific trigger selection

Tracks in the Drift Chamber		Example cuts
A tracks	Tracks that reach the outer layers of the drift chamber.	na
A$'$ tracks	A tracks above a certain p_t threshold.	$p_\mathrm{t} > 0.800\,\mathrm{GeV}/c$
B tracks	Tracks that reach the middle layers of the drift chamber.	na

Clusters in the Calorimeter		Example cuts
M clusters	Clusters with energies $\geq$ minimum ionizing particles.	$E_\mathrm{clus} > 0.120\,\mathrm{GeV}$
G clusters	Clusters with energies above those of M clusters.	$E_\mathrm{clus} > 0.160\,\mathrm{GeV}$
E clusters	Clusters with energies well above those of G clusters.	$E_\mathrm{clus} > 0.500\,\mathrm{GeV}$
X clusters	Clusters in forward endcap for background veto.	$E_\mathrm{clus} > 0.120\,\mathrm{GeV}$
Y clusters	Clusters in backward barrel from asymmetric $e^+e^-(\gamma)$.	$E_\mathrm{clus} > 2.000\,\mathrm{GeV}$
G-M clusters	G clusters with M clusters back-to-back in ϕ.	see above
E-M clusters	E clusters with M clusters back-to-back in ϕ.	see above

Matches Between the Drift Chamber and Calorimeter		
A-M matches	A tracks correlated in ϕ with barrel M clusters.	see above
A$'$-M matches	A$'$ tracks correlated in ϕ with barrel M clusters.	see above
B-M matches	B tracks correlated in ϕ with barrel or endcap M clusters.	see above
A-G matches	Electron tags, also including A$'$-E, B-G etc.	see above

Table 3.3: Trigger objects for the Level 1 trigger.

lines, where each line is the result of a boolean operation on any combination of trigger objects.

The types of trigger objects may be arranged in the following hierarchy:

1. Drift chamber charged particles with explicit ϕ-separation cuts;
2. Drift chamber charged particles with explicit p_t and ϕ-separation cuts;
3. Calorimeter clusters with explicit E_clus and ϕ-separation cuts;
4. Charged particles correlated between the drift chamber and calorimeter M or X clusters, with explicit matching in ϕ; and
5. Special triggers for calibration, monitoring, and diagnostics.

Note that both detectors have implicit p_t and θ cuts due to their fiducial acceptances. More refined selection cuts, applied to the full data set, may be made in Level 3.

Note that with this set of trigger objects there is no event selection based on θ-position available, except for the X and Y clusters.

Trigger Lines

Table 3.4 shows some trigger lines that are used in the current trigger strategy along with the criteria used for each line. The multiplicity of each object is represented by its letter, e.g. A is the number of A tracks. A star (*) next to a trigger object indicates that a minimum angular separation was required in order to count more than one object (typically 90°). Note that every A track also counts as a B track and that clusters above a certain threshold also pass all thresholds below. Back-to-back topologies among clusters are written the same way as track-cluster matches, e.g. E-M means an E cluster back to back with an M cluster. An &-symbol denotes requiring clusters and tracks in coincidence, a non-orthogonal selection-criterion. Using the notation of Table 3.3, one can describe any trigger criterion that the Level 1 trigger is capable of producing.

Under severe backgrounds each of the trigger lines will be subject to individual prescaling, which may have to be used to reduce rates for the looser definitions, while still collecting all events satisfying more stringent definitions. The final Level 1 Accept is formed after any such prescaling.

Trigger Line Name	Trigger Criterion
Drift Chamber Trigger Lines	
Open drift chamber trigger (D_2)	$(A \geq 1$ & $B \geq 2)$ `OR` $A \geq 2$
3A trigger	$A \geq 3$
D_2' trigger	D_2 & $A' \geq 1$
$D_2'^{*}$ trigger	D_2' & $B^{*} \geq 2$
2A$'$ trigger	$A \geq 2$ & $A' \geq 1$
Calorimeter Trigger Lines	
Open calorimeter trigger (C_2)	$M \geq 2$
C_2' trigger	E-$M \geq 1$
3M trigger	$M \geq 3$
Asymmetric bhabha trigger (Y trigger)	$Y \geq 1$
2G* trigger	$G^{*} \geq 2$
Trigger Lines using both Drift Chamber and Calorimeter	
2M&1A trigger	$M \geq 2$ & $A \geq 1$
2M&1A$'$ trigger	$M \geq 2$ & $A' \geq 1$

Table 3.4: Sample trigger lines and their definitions.

Benchmark Processes

In order to evaluate the efficiency of selection algorithms, a set of physics processes has been identified to serve as trigger benchmarks. The BaBar physics program focuses on studies using $\Upsilon(4S)$, $\Upsilon(5S)$, $q\overline{q}$, $\tau^{+}\tau^{-}$, $\gamma\gamma$, and $\gamma\gamma^{*}$ events. While the primary mission of the BaBar experiment is the study of *CP* violation in B decays, the trigger is designed to accept a large number of processes that may be important. The trigger benchmarks represent processes that are difficult to distinguish from background. Other similar processes have, or are expected to have, higher efficiencies.

For $B^0\overline{B}^0$ *CP* studies, the most difficult tag to trigger on is $\overline{B}^0 \rightarrow \mu X$ because of its low charged-track multiplicity and low cluster energy compared to the electron or kaon tags. The low-multiplicity decay $B^0 \rightarrow \pi^+\pi^-$ was chosen as a *CP* study decay mode to test the efficiency of the simple particle counting trigger algorithms. The high-multiplicity decay $B^0 \rightarrow D^+D^-$ was chosen to test algorithms that require fast tracks.

For other B-physics, the rare decay mode $B^+ \rightarrow \tau^+\nu, B^- \rightarrow X$ was identified as very challenging due to its relatively low charged-track multiplicity.

For $\tau^+\tau^-$ studies, events in which both taus decay to one charged track are the most difficult to select. To measure the muon branching ratio, events with $\tau^- \rightarrow \mu^-\bar{\nu}\nu$ occurring jointly with $\tau^+ \rightarrow e^+\nu\bar{\nu}$ are used. This is a worst-case decay for the purpose of the benchmark table, as the measurement is not expected to be statistics limited. The other $\tau^+\tau^-$ benchmark is an untagged event for which each tau decays to one charged pion, used to measure spin correlations for V−A tests and other Lorentz structure measurements.

For two-photon physics, the first $\gamma\gamma$ benchmark was chosen as $\pi^+\pi^-$ production with invariant mass greater than $2\,\mathrm{GeV}/c^2$. The second $\gamma\gamma$ benchmark was chosen as $\pi^0\pi^0$; triggering on this process relies almost entirely on the calorimeter trigger. The $\gamma\gamma^{(*)}$ benchmark with the generic $KK\pi$ as the final state represents the search for exotic mesons. For the simulation the $K^\pm K^0_s\pi^\mp$ final state was picked ; The final $\gamma\gamma^{(*)}$ benchmark represents single-tagged, high-q^2 production of the pseudoscalar meson $\eta(550)$, with decay to the mixed state $\pi^+\pi^-\pi^0$. Such low-mass states are very difficult to trigger on, but the resulting rate should still be sufficient for QCD studies.

3.3.2 Level 3 Trigger

The Level 3 trigger is part of the online farm and consists of a network of commercial processors. Input are the Level 1 trigger data and the full event data for events that passed the Level 1 trigger. Output to mass storage is the full event and trigger data of events accepted by Level 3.

Level 3 trigger algorithms have all event information available. Several strategies can be pursued here. First, a cut on the vertex position can be made to reject events that did not originate at the interaction point. This can be done with either drift chamber or silicon vertex tracker information. A drastically reduced data set could be used very efficiently for the silicon vertex tracker [Grace 95]. Also, a refined event time determination is useful to reject background events with tracks or clusters from different beam crossings (see Appendix A). Furthermore, matching silicon vertex tracker and drift chamber tracks can help in discriminating background from physics events. Matches with other detector components might also reduce background rates. The maximum logging rate for writing events to mass storage is 100 Hz. Contrasting this number with the maximum trigger rate of 2000 Hz of the Level 1 trigger, a background rejection ratio of 1:20 has to be achieved on this level.

In case the Level 1 trigger rate exceeds 2000 Hz, the Level 2 trigger option would come into effect. It would be envisioned to use only drift chamber information from the Level 1 trigger to perform preliminary vertex cuts to reduce the rate.

A handle on all-neutral background events, where calorimeter data would be needed for further discrimination, is not expected to be needed. Studies assuming $\times 10$ worse background conditions than anticipated showed that this rate is around 70 Hz, which is already low enough for a Level 3 input rate.

3.4 Level 1 Trigger Components

This section gives an overview of the components of the Level 1 trigger system. Three main parts can be identified: drift chamber trigger, calorimeter trigger and global trigger. The drift chamber trigger finds charged tracks and the calorimeter trigger finds energy clusters. Both sets of information are combined in the global trigger for the final Level 1 trigger decision. Figure 3.2 depicts the main components of the Level 1 trigger. Note that the trigger also receives a signal from the IFR for use in cosmic ray detection. The main components of the drift chamber trigger are explained later in this section. Figure 3.3 is a display of a typical event that illustrates the trigger decision process.

3.4.1 Calorimeter Trigger

The calorimeter trigger is based on towers (groups of contiguous crystals) as opposed to single crystals because the center crystal of a shower will contain at most about 80% of the shower energy [SLAC 93]. The better estimate of the total energy deposited in a tower compared with a crystal means that any energy threshold cut applied in the trigger is more precise, which is not only better for background rejection, but is also important for understanding and modeling the trigger response accurately.

The algorithm for the calorimeter Level 1 trigger [Kral 94a] is summarized in this section. It is based on fixed towers of mostly 8×3 crystals [Dauncey 96b] and performs three functions: local tower energy summing to form primitives, cluster formation, and time feature extraction.

Local Tower Summing

Each tower, consisting of the signals of an 8×3 group of crystals [Kral 94a, Gehrig 96c], will be read out by a single calorimeter readout module, and the calorimeter trigger primitives will be constructed from tower sums formed on the board. There are 40 towers in ϕ and six towers in θ along the barrel. For the endcaps, including a potential future backward endcap, there are 40 towers in ϕ and two in θ. This gives a total of $40 \times 6 + 40 \times 2 = 320$ towers. The trigger sampling rate is the same as the data digitization rate (3.7 MHz).

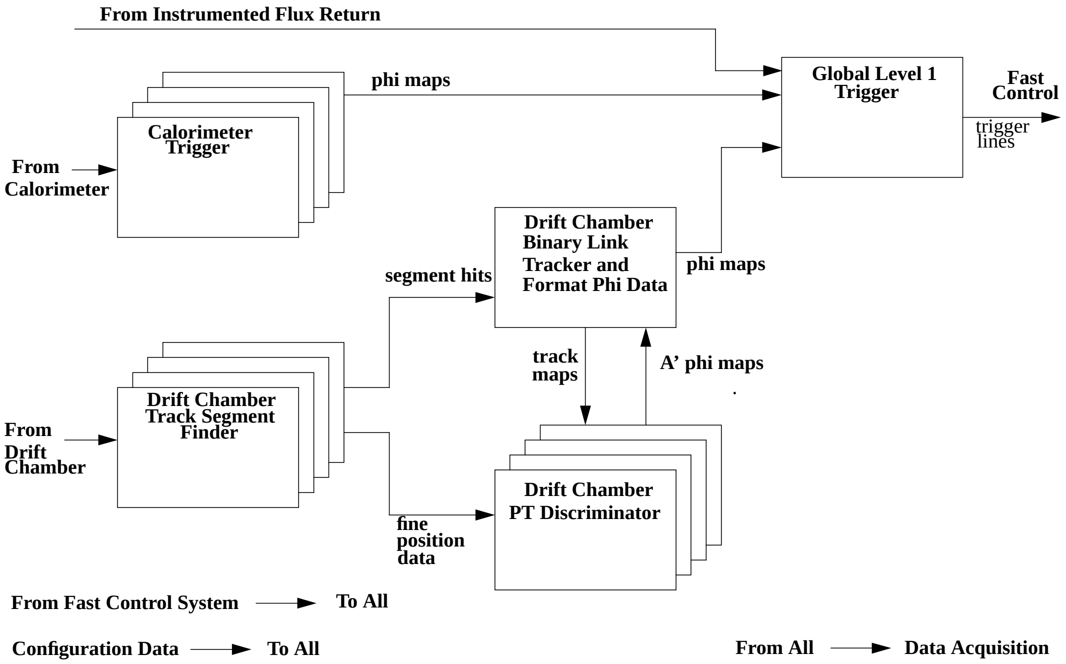

Figure 3.2: Level 1 trigger components. Each box represents one or more boards in the hardware implementation.

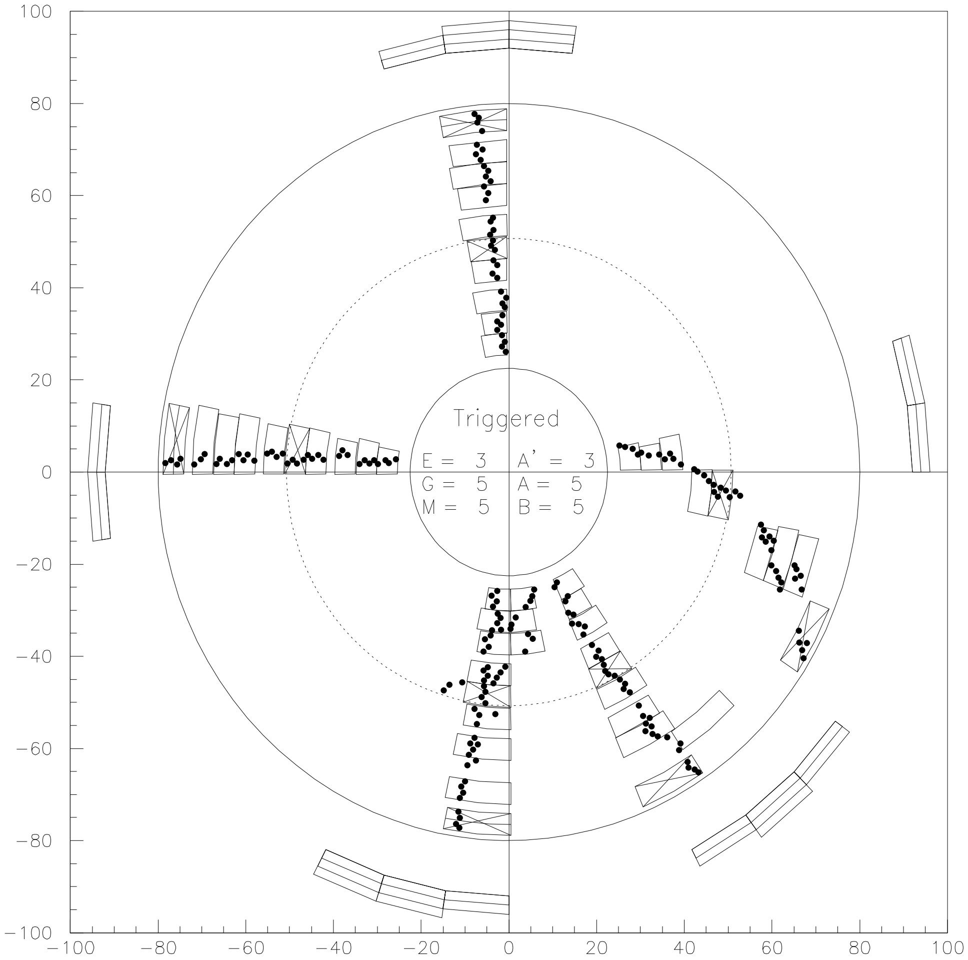

Figure 3.3: Example of a trigger response to a simulated $B^0\overline{B}^0$ event showing the drift chamber and calorimeter in an x-y view. Boundaries of supercells that were hit are drawn. Crosses mark ϕ locations of A tracks and B tracks. A cross with a bar through marks ϕ locations of A′ tracks. There were cell inefficiencies simulated. Cluster ϕ positions are marked outside the drift chamber. Two arcs indicate G clusters and three arcs indicate E clusters. Note the overlap inherent in the calorimeter trigger algorithm.

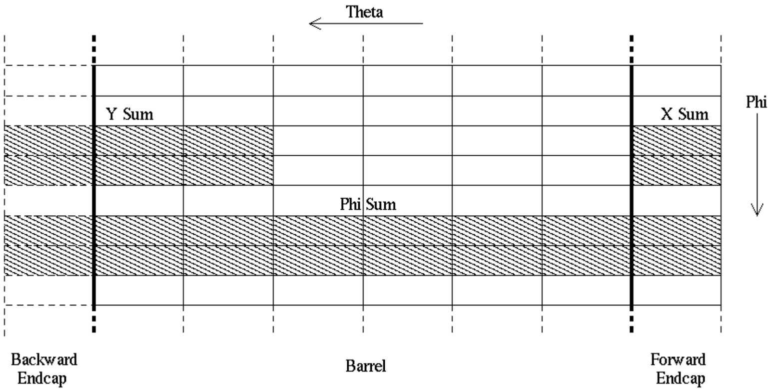

Figure 3.4: Division of tower sums into clusters in the calorimeter trigger. Only a subset of the ϕ bins is shown. The backward endcap (tower sums in dashed lines to the left) is a possible upgrade for the calorimeter.

For each time sample, the 24 channels of data are calibrated and converted to a cruder energy scale of 16 bits using a look-up table. This table allows a large degree of flexibility; an individual channel threshold cut can be trivially applied to remove low-energy backgrounds. The 24 outputs are summed using a programmable logic device to give a total tower energy for each sample in 16 bits. These sums form the calorimeter trigger primitives.

Cluster Formation

Due to energy sharing between towers, the towers are considered in neighboring pairs in ϕ, after summing up all θ tower sums. This yields 40 energy clusters for the trigger. The special X and Y clusters indicate energy deposits in the very forward and backward direction, respectively. Y clusters catch low-angle bhabhas where the electron in the forward direction is outside the detector's acceptance and X clusters help reducing background in case of unforeseen high background rates in the forward endcap. The division of the tower sums into clusters is pictured in Figure 3.4. There are five separate energy thresholds for clusters in the trigger: an M cluster (above a low energy consistent with a minimum ionizing particle, 120 MeV), a G cluster (higher than M, e.g. 150 MeV), an E cluster (significantly higher in energy), a Y cluster (for asymmetric bhabhas in the backward barrel), and an X cluster (for optional background discrimination in case of very high background in the forward direction). These correspond to the trigger objects in Table 3.3.

Time Feature Extraction

The time of the energy arrival in the calorimeter has to be determined. This is done for every single ϕ strip. The energy deposit of a particle causes a certain calorimeter response in time that depends on the energy deposited. To determine the energy arrival time a finite impulse response filter (FIR) is used. It takes the eight most recent energy samples of every ϕ strip and multiplies each entry with a certain weight. The time is determined by the zero-crossing of the FIR output. To get a better time estimate, the FIR output is linearly interpolated running at a 7.4 MHz clock, twice the digitization speed.

3.4.2 Drift Chamber Trigger

The drift chamber trigger consists of three main components (see Figure 3.2). Receiving the digitized hit signals from the drift chamber, the track segment finder links hits together within a supercell. It supplies the binary link tracker (BLT) with one bit per supercell to indicate whether a track went through that cell. The BLT itself links these supercells together to form tracks. The PT discriminator as the third main component receives fine position information from the segment finder and determines whether a found track is above or below a certain transverse momentum threshold [Gehrig 96a].

Track Segment Finder

Segment finding is used frequently as an initial part of drift chamber trigger algorithms (see e.g. [ZEUS 92]). For *BaBar*, we also use crude drift time information. Hence different drift times for different wires have to be taken into account, which is done in a calibration step. The track segment finder receives the raw drift chamber hits as input. These hits start counters that count for a full drift time to produce at least one tick where all hits corresponding to one event are on. There are 1776 segment finders producing segments for every pivot cell (third cell within a superlayer) in the drift chamber. Segments that have adjacent hits in 3 or 4 out of 4 layers per superlayer are assumed to have a track traversing. These segments are sampled every 3.7 MHz. The other components of the segment finder run at the trigger clock speed, 7.4 MHz. The segment finder waits to report the “best” segment found for one drift time (typically the segment where all hits were on). The timing of these segments is latency adjusted and stretched to ensure coincidences in further processing.

Binary Link Tracker

The BLT receives a map of hit supercells as input. It uses a track linking algorithm developed by K. Kinoshita [Kinoshita 89] for the CLEO II experiment [CLEO 91] that is simple, fast, and easy to implement in hardware. Starting in superlayer 1 (closest to the interaction point), the algorithm moves radially outward looking for hits in any of the five neighboring supercells in the previous superlayer. Isolated segments and tracks traversing far away from the interaction point are rejected this way.

PT Discriminator

For other experiments, performing p_t cuts on tracks is typically done on the resolution level of one drift cell (see e.g. [H1 92]). The PT discriminator in BaBar needs more detailed information to determine the transverse momentum of a track accurate enough to yield a sharp turn-on curve in the momentum region 300 – 1000 MeV/c. This fine position is made available by the segment finder. Using the fine position information from the axial superlayers it selects tracks that stay within certain limits (predetermined by the p_t threshold value chosen). The PT discriminator runs at 3.7 MHz.

3.4.3 Global Trigger

The global trigger combines the calorimeter and drift chamber trigger data to make the final Level 1 trigger decision. First the global trigger combines tracks and clusters ϕ maps to match tracks and clusters. In the next step all trigger objects are counted. Using that information trigger decisions are made depending on the multiplicities of the trigger objects producing 30 trigger lines. Final object counts for an example event are shown in Figure 3.3. In a final step, the trigger line yielding the best time information is selected, sending the time to the Fast Control System. The Level 1 Accept signal is issued by the Fast Control System after prescaling.

Chapter 4

Event Simulation Method

4.1 Overview

Level 1 trigger design choices are motivated by results from Monte Carlo simulations. These simulations are the major source of information to verify the performance of selected algorithms. The first part of this chapter introduces the simulation tools.

To verify the performance of trigger algorithms, physics benchmark processes were selected (see Section 3.3.1). The simulation tools used here produce events over the full solid angle. For physics analysis, only a subset of these events is of interest. Hence the trigger algorithms only need to trigger on those events. So we need to apply so-called fiducial cuts to limit the efficiency estimates to the "interesting" events. This is explained in Section 4.3.

4.2 Event Simulation Tools

4.2.1 GEANT

BaBar uses the standard particle physics simulation tool GEANT [CERN 95] to track particles and simulate the detector response. GEANT has the following features: It consists of packages to construct the detector geometry using a set of 15 different volume types. Charged and neutral particles can be tracked through the detector simulating the full variety of interactions. In addition, packages to define and digitize track hits, and to display the results are included. Various event generators were used to feed particle four vectors to GEANT. For $\Upsilon(4S)$ events, the event generator JETSET was used and for $\tau^+\tau^-$ decays, the event generator KORALB was used (see [TDR 95] and references therein). Several other event generators were used for background sources (see Figure 4.1).

4.2.2 The *BaBar* Simulation Environment

The generation of an e^+e^- collision and the interface to GEANT is handled by the package BEGET. It is also possible to overlay simulated background hits on physics events.

Subsequent GEANT simulation of the detector response is done by the BBSIM package [BBSIM 96]. In this simulation, raw drift chamber and calorimeter hits were produced. In a second step, algorithms were implemented for a full tick-based digitization and trigger timing model. The trigger simulation consists of the software packages trgFrame (hit mixing), trgDC (drift chamber and global trigger) and trgEM (calorimeter trigger) [trgFrame 96, trgDC 96b, trgEM 96]. Figure 4.1 shows a data flow diagram of the simulation tools introduced in this section.

4.2.3 Simulating Cell Inefficiencies

Drift chamber cell inefficiencies are implemented by randomly removing hits, which is conservative compared to removing hits at the less efficient edges of cells. Comparison of random inefficiencies and inefficiencies correlated to cell edges showed that random inefficiencies always yield a worse trigger efficiency.

4.2.4 Background Simulation

The trigger simulation used, as explained above, the full GEANT simulation of the BABAR detector for the detector response simulation [BBSIM 96]. Background sources are described in Section 3.2.2. Cosmic rays occur rarely and are independent of beam bunch crossings. Interactions due to lost beam particles close to the interaction point, beam gas interactions, and radiative bhabhas occur in synchronization to beam bunch crossings. Beam gas interactions, simulated by interactions with nitrogen (main air component), yield a very low trigger rate (see Chapter 7) and don't produce much occupancy. In earlier simulations radiative bhabhas had little impact on both trigger rates and occupancies in the detector systems [Dauncey 96a]. Hence only the lost beam particle background is simulated for overlaying background on physics events: Lost beam particles are overlayed on physics events at random beam crossings by appending the GEANT hit data accordingly (hit mixing).

Mixing background onto the physics event can lead to multiple hits on a drift chamber wire. An optimistic re-enabling model allows a drift cell to receive a hit signal again right after another hit signal was received (no deadtime). The other extreme is not to allow any more hit signals to come from this drift cell in the same event (equivalent to $2.5\,\mu$s deadtime). Both possibilities were simulated and the results remained almost unchanged. This is due to the fact that a drift cell is very unlikely to be hit twice in $2.5\,\mu$s. For all studies here optimistic re-enabling was assumed.

For trigger rate studies, all event sources mentioned above were simulated overlayed with lost beam particle background. Synchrotron radiation produced near the interaction point has negligible impact on trigger rates (see [TDR 95], Chapter 12).

Lost Beam Particle Background

Bremsstrahlung and Coulomb scattering of beam particles from residual gas molecules in the beam pipe can result in high-energy beam particles and photons striking material near

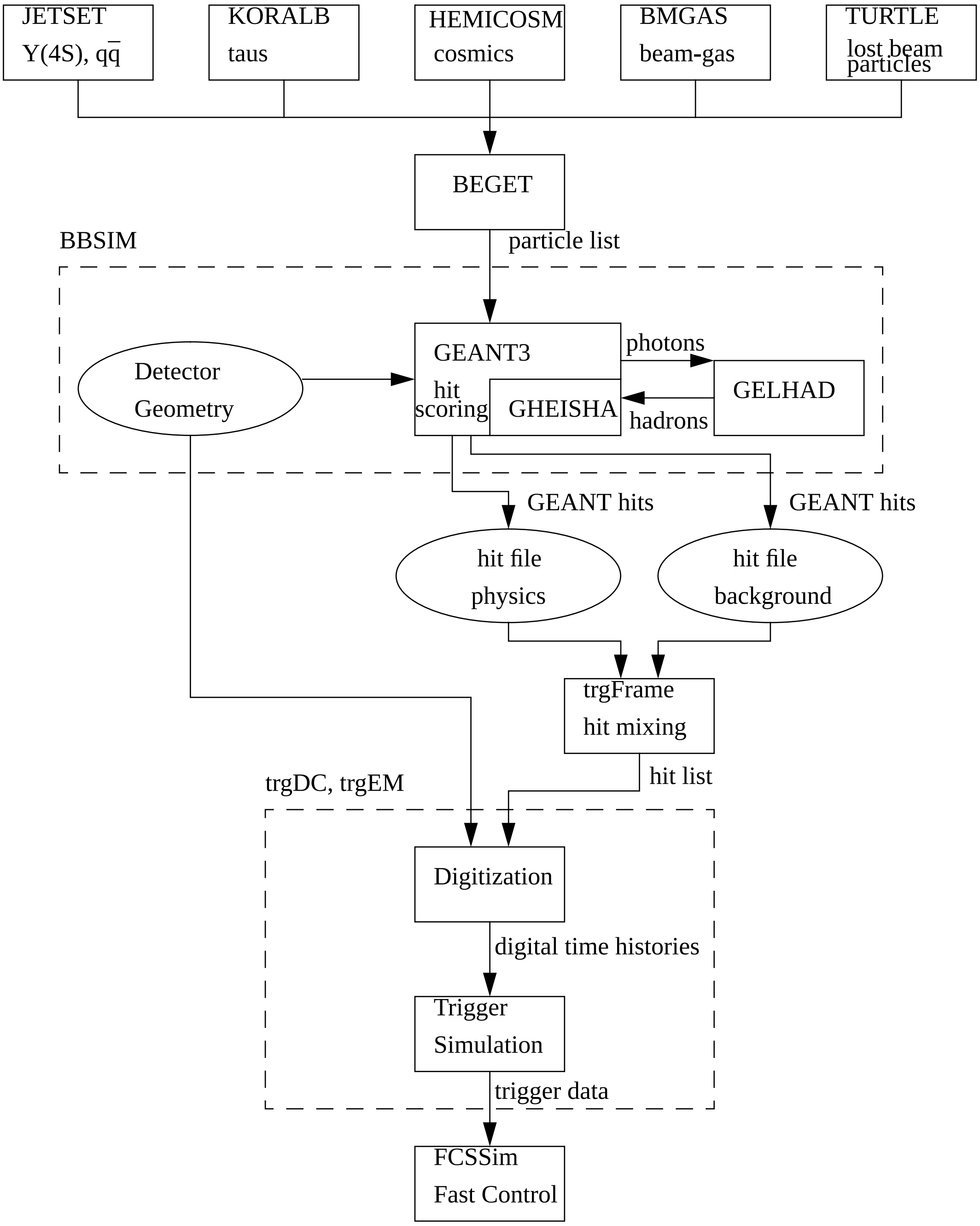

Figure 4.1: Context diagram of the BaBar simulation environment.

the interaction point (lost beam particles). Such lost beam particles are obtained via the accelerator simulation package TURTLE. These particles can either interact hadronically or electromagnetically. Simulations of lost beam particles use the GEANT package GHEISHA called by the *BaBar* package GELHAD to perform photoproduction of hadrons. This model, based on photon-nucleon interactions, conserves charge and energy, but in general, momentum conservation is violated. Above 150 MeV the photon in the model is replaced by a pion that interacts with the nucleus. For a more detailed description see [TDR 95], Chapter 12, and references therein.

All lost-particle backgrounds were simulated with a non-uniform beam line pressure profile and a recent model of the interaction region, unlike the studies in [TDR 95].

To promote a photon-to-hadron conversion in the simulation in worst-case studies, the cross sections of photoproduction were enhanced by a factor of 10. In order to investigate the nature of these showers the GEANT data of the produced particles were analyzed. The main particles producing trigger rates are protons (40%), deuterons (20%), and pions (20%). Tritons and alphas also occur in the simulations but are not found in data of the TPC experiment at PEP [Ronan 96, Lynch 89]. Figure 4.2 shows an x-z scatter plot of the vertices of hadronic interactions that produced triggers. Since the vertices for both original photoproduction cross section and ×10 enhanced cross section originate from roughly the same locations, the vertices of the hadronic interaction seem not very dependent on the cross section strength.

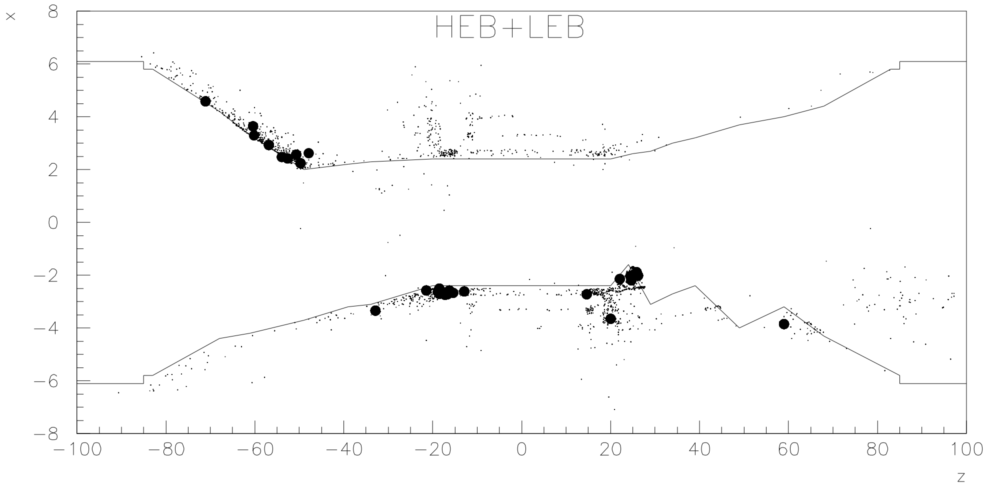

Figure 4.2: Photoproduction vertex information in the x-z plane: Overlaying this information with the beam pipe model shows that most tracks originate at the copper around the B1 magnets, which is indicated by the lines in the figure. For the high-energy beam (HEB) no open triggers are produced for $|z| > 100cm$. Only 1 % of the LEB triggers originated outside this window. 100,000 events were generated, 1651 passed the open DC trigger for the HEB. For the LEB also 100,000 events were generated and 1121 passed the open DC trigger (small dots in the figure). For the HEB at nominal cross-section 1,000,000 beam crossings were simulated that produced 85 open triggers for nominal background. For the LEB 2,000,000 beam crossings were simulated that produced 10 triggers (large solid circles in the figure).

Comparing these vertices to the beam pipe model it turns out that almost all hadronic interactions that trigger occur in the copper layer of the B1 permanent magnets. These are used to separate high and low-energy beam to prevent multiple crossings with one bunch. The boundaries of the copper layers are indicated by the lines in Figure 4.2. The B1 magnets extend from 20cm to 60cm in z on both sides of the interaction point. This result also shows that primary vertex determination in the x-z plane is an excellent means to discriminate background from physics events in the Level 3 trigger.

4.3 Fiducial Cuts for Physics Events

The requirements for the trigger efficiencies apply to physics events that are of interest for physics analysis. In order to select these events from all events generated over the full solid angle, we identify some particles from every benchmark process to be crucial to the physics analysis. These particles have to be within the geometric acceptance of the detector system that identifies it. Table 4.1 shows the geometric acceptances that were used for the detector subsystems and the particles identified by those detectors. These cuts are referred to as fiducial cuts.

Detector	Particles	p_t or p (GeV/c), E (GeV)	$\cos(\theta_{\min})$	$\cos(\theta_{\max})$
Drift Chamber	K_s^0, D	$p_t > 0.080$	-0.93	0.97
Calorimeter	γ, e	$E > 0.020$	-0.78	0.96
DIRC	π	$p_t > 0.250$	-0.84	0.90
IFR	μ	$p > 0.650$	-0.88	0.96

Table 4.1: Geometric acceptances of the BaBar detector subsystems and the particles identified by those detectors. These cuts represent simplified versions of cuts that will be made in eventual physics analyses.

The benchmark process $B^0 \to D^+D^-$ has many decay channels. In this case we only require that the D mesons point into the geometric acceptance of the drift chamber as a crude fiducial cut. If π^0 is one of the decay products we require 2 photons in the geometric acceptance, since this decay channel has a 99% branching ratio. Table 4.2 summarizes the fiducial cuts for all benchmark processes.

Benchmark process	Required particles
$B^0 \to \pi^+\pi^-$, $\overline{B}^0 \to \mu$X	π^+, π^-
$B^0 \to D^+D^-$, $\overline{B}^0 \to$ X	D^+, D^-
$B^+ \to\ \tau^+\ \nu\ , B^- \to\ X$	e, μ or all π's as daughter particles from τ
$\tau^+ \to e^+\nu\bar{\nu}$, $\tau^- \to \mu^-\bar{\nu}\nu$	e, μ
$\tau^+ \to \pi^+\bar{\nu}$, $\tau^- \to \pi^-\nu$	π^+, π^-
$\gamma\gamma \to \pi^+\pi^-$, $\mathrm{W}_{\gamma\gamma} > 2\,\mathrm{GeV}/c^2$	π^+, π^-
$\gamma\gamma \to \pi^0\pi^0$, $\mathrm{W}_{\gamma\gamma} > 2\,\mathrm{GeV}/c^2$	4 γ's
$\gamma\gamma^{(*)} \to X(1420) \to KK\pi$	$K^{+/-}, \pi^{-/+}, K_s^0$ or 4 charged particles
$\gamma\gamma^{(*)} \to \eta(550) \to \pi^+\pi^-\pi^0$	π^+, π^-, all occurring γ's

Table 4.2: List of particles required in the fiducial volume of benchmark processes.

Chapter 5

Drift Chamber Trigger Algorithms

5.1 Drift Chamber Trigger Overview

This chapter is devoted to the algorithmic description of the drift chamber trigger and its performance. The performance results reported here motivated the current design of the Level 1 trigger. First the segment finder algorithm is described. Next the track linker (BLT) algorithm is explained and its performance shown. In the final section the PT discriminator algorithm is introduced and its effectiveness demonstrated.

The segment finders produce a map of segment hits for the BLT and report fine position data to the PT discriminator. The map of linked hits produced by the BLT serves as input to the PT discriminator in addition to the fine position data of the axial superlayers from the segment finder. From this information, the PT discriminator makes a decision whether the track found by the BLT is below or above a certain $p_{\rm t}$ threshold. The BLT and the PT discriminator report ϕ maps of A tracks, B tracks and A$'$ tracks used in the track multiplicity counter in the global trigger. Figure 5.1 illustrates the main functions of the drift chamber trigger.

5.2 Track Segment Finder

We need a method for determining where tracks pass through the drift chamber for the Level 1 trigger. This is done by looking for “segments” in each supercell, then linking supercells with valid hits (trigger primitives) together to form tracks (trigger objects).

5.2.1 Segment Finder Template

The search for segments is organized in terms of pivot cells. Physically, pivot cells are the cells in the third radial layer—the pivot layer—of each superlayer. The complete segment finder consists of 1776 segment finder template circuits, one for each pivot cell. The template circuit processes data from cells in its template to find track segments that pass through its pivot cell and neighboring cells in the other three layers.

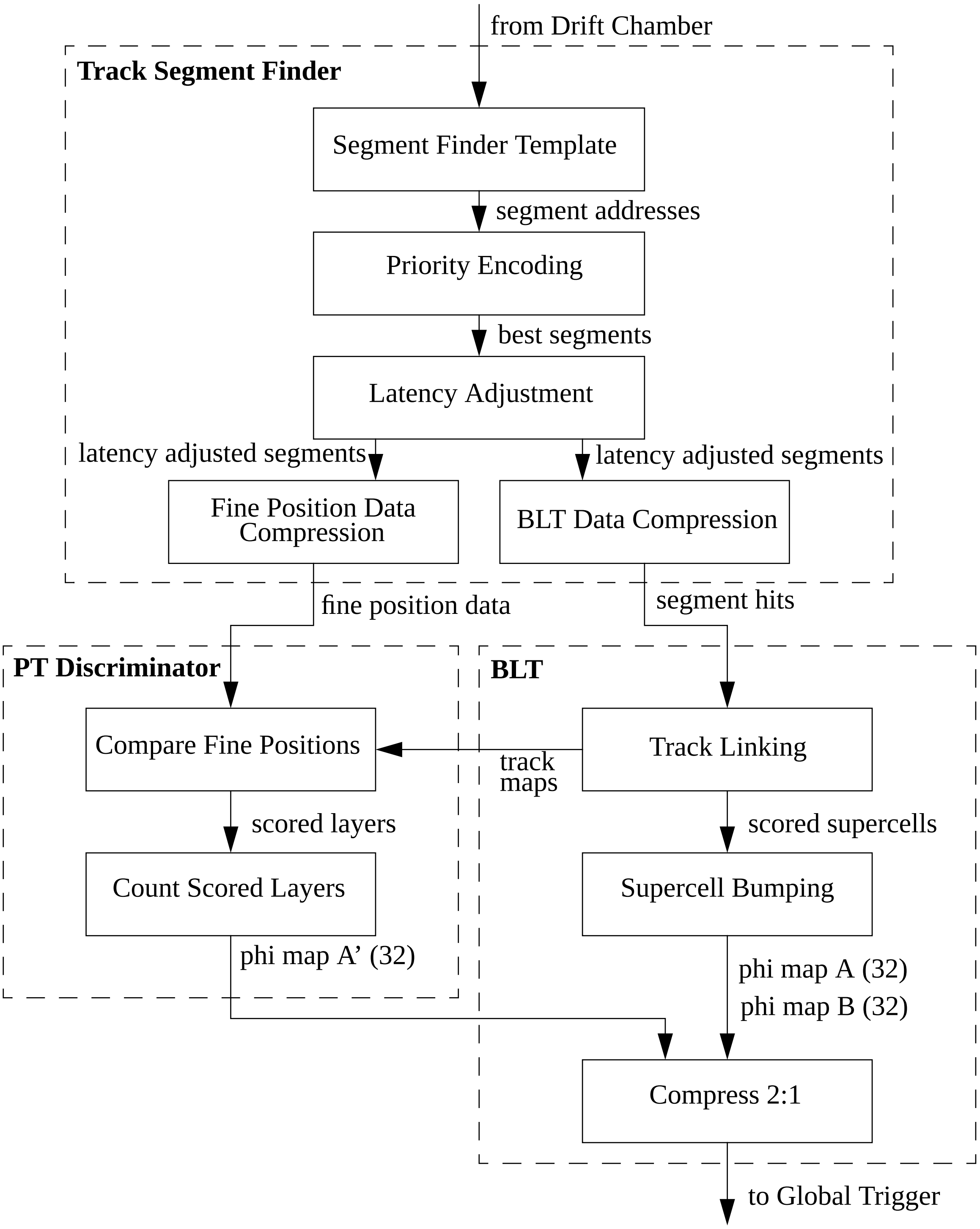

Figure 5.1: Block diagram of the functions of the drift chamber trigger. All functional blocks shown here are described in this or the next chapter.

Each segment finder template circuit has eight channels, each of which receives digital-discriminator output signals from one of eight neighboring drift chamber cells. These are, for example, the cells numbered 0 through 7 (the template) in Figure 5.2, where cell 4 is the pivot cell.

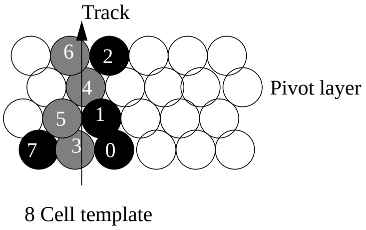

Figure 5.2: Segment finder cell template. The segment finder looks for tracks passing through each of the pivot cells in the third layer of each superlayer and returns an address based on which of the eight surrounding cells in the template were hit. In this case, the track went through cells 3, 5, 4, and 6, giving an address of 120.

Each segment finder template circuit continually peruses the signals from its eight channels, looking for 'valid' segment patterns of hits that can be interpreted as track segments. Sets of valid segment patterns are stored in segment pattern memories.

Typically, valid segment patterns consist of hits, close together in time and in three or four neighboring cells, that lie on what are pre-defined as acceptable tracks within a supercell—i.e. tracks that traverse the supercell within pre-defined azimuthal angles, ϕ. To assure coincidence in time of all hits belonging to one track, the hits have to be extended for a full drift time with a one-shot.

The algorithm is based on an *a priori* definition of the range of valid tracks[1] that could possibly traverse each pivot cell. In the template shown in Figure 5.2, the cells 0–3 and 5–7 are the only cells that could possibly be hit when traversed by a particle on a valid track that passes through cell 4. The signals from these eight cells (template) are therefore processed as a group.

Allow the template to slide laterally so that '4' now identifies an adjacent pivot layer cell. A new group of eight cells can now be identified: the new '4' and seven more. Note that, of the seven, all are also associated with at least **one** other pivot cell and are therefore shared between template circuits. In particular, the cells labeled '7,' '3' and '0' are associated with **two** other pivot cells and template circuits.

There are 256 possible segment patterns for a template. Using the constraint mentioned above, there are 112 valid 3/4 segment patterns where 1 layer was missed and 57 valid 4/4 segment patterns containing hits in each of the four layers. The segment finder described here is referred to as the one-shot segment finder.

---

[1] That is, tracks having p_t within the range of acceptance. See Reference [Kral 94b].

Figure 5.3 shows the segment finder algorithm put to work using a typical simulated $\tau^+\tau^-$ event developing in time, sampled with a 269 ns period. The hits disappear more abruptly than they appear. This is due to the fact that the distance to drift time relationship is not linear (see Section 2.4.3).

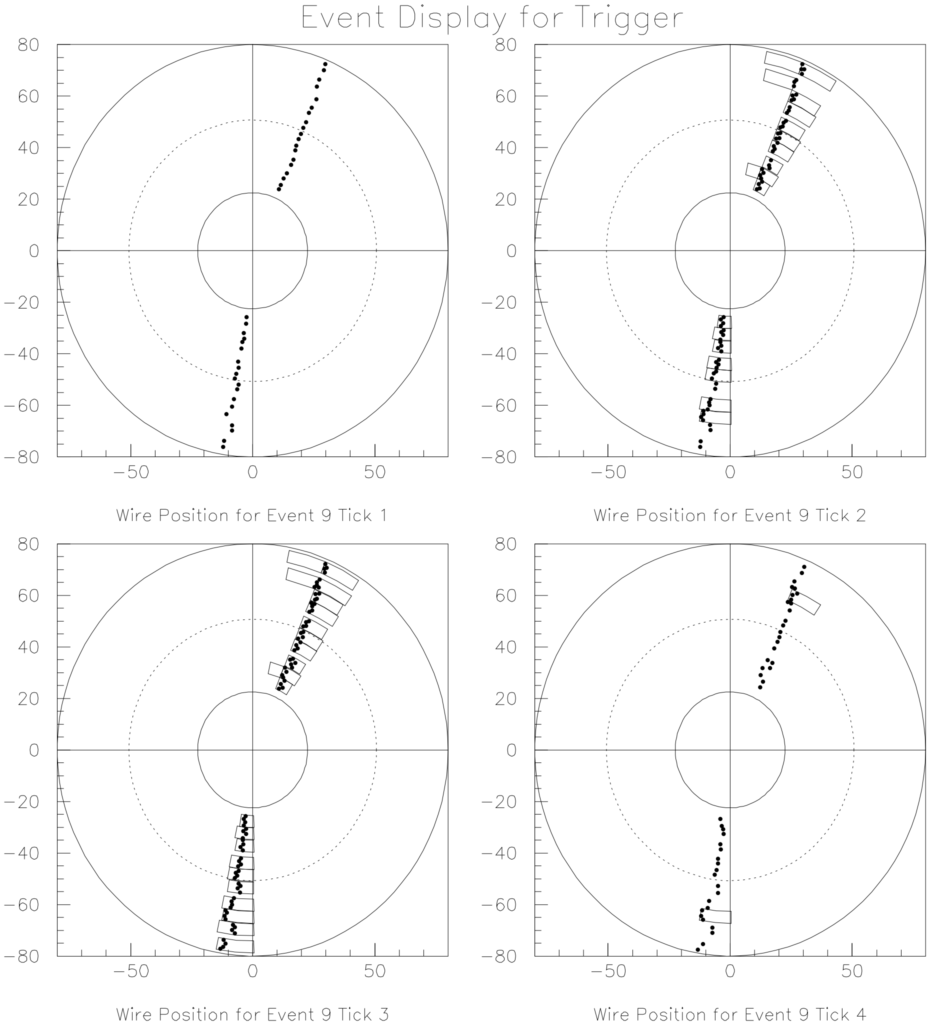

Figure 5.3: Drift chamber x-y view for a simulated $\tau^+\tau^-$ event. The small circles indicate wire hits and the rectangles indicate supercells with valid segments (with hits in at least 3 out of 4 layers per supercell). Time evolution with a 3.7 MHz sampling frequency is shown here; the hits stay on for 3 ticks.

5.2.2 Counter-Based Segment Finder

Here we use two bits per cell to give drift time information for the track, instead of just using one to report whether the cell was hit or not. The address reflects how much time has passed since the wire was hit. By incrementing a counter every 269 ns (64 beam crossings) after a hit, we can thus obtain an approximation of the drift time. This is shown on the lower right hand corner of Figure 5.4. From the drift time and the relationship shown in Figure 2.5, we can thus obtain a better axial (ϕ) position resolution, as well as a better time-of-event resolution than in the one-shot case. This approach produces 65536 addresses instead of 256. There are 62721 valid 3/4 segment patterns and 41715 valid 4/4 segment patterns. Of those 4/4 patterns, 367 report a calibrated address as defined in the next section.

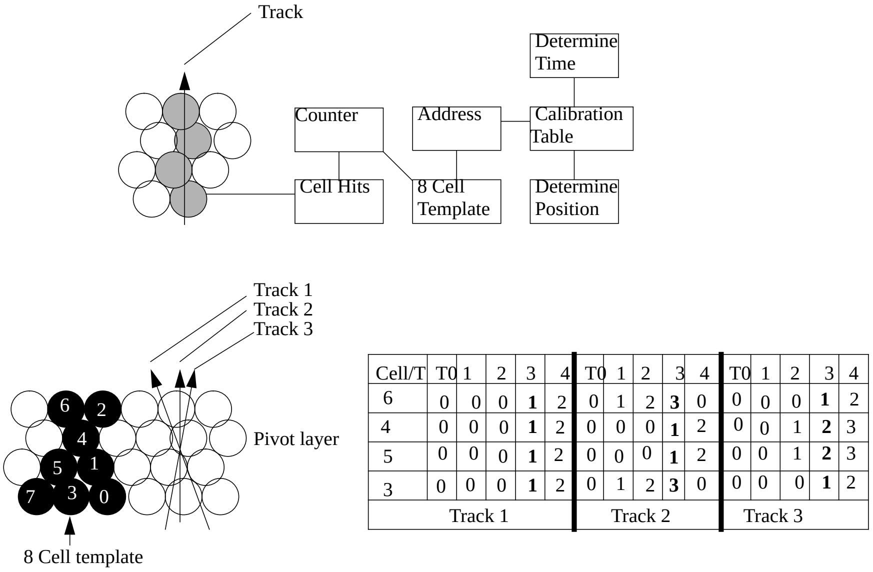

Cell/T	T0	1	2	3	4	T0	1	2	3	4	T0	1	2	3	4
6	0	0	0	**1**	2	0	1	2	**3**	0	0	0	0	**1**	2
4	0	0	0	**1**	2	0	0	0	**1**	2	0	0	1	**2**	3
5	0	0	0	**1**	2	0	0	0	**1**	2	0	0	1	**2**	3
3	0	0	0	**1**	2	0	1	2	**3**	0	0	0	0	**1**	2
Track 1						Track 2					Track 3				

Figure 5.4: The counter-based segment finder (top) passes the cell hits to a self-triggered 2-bit counter that increments every 269 ns and then resets, thus giving a 16-bit address that contains information about the drift time elapsed in each cell. Example tracks (bottom left) are shown with their corresponding addresses as they evolve in time (bottom right).

5.2.3 Calibration of the Counter-Based Segment Finder

Since tracks with different positions and different event times can share the same address, we need to find the average position and time for each address. We do this by using 25000 single-muon events, tracked through the drift chamber in BBSIM [SRT 96], and recording the true positions of all of the tracks for each address, as well as the times the addresses occurred relative to the true event time[2]. From this we calculate for each address the average

---

[2] Each event has a random phase (0-31 beam crossings when running at 7.4 MHz), which is accounted for in the calibration.

and standard deviation of the position in ϕ measured in cell widths, as well as the average latency (t_i) and its standard deviation (σ) measured in beam crossings. In addition, we calculate the 100% width confidence intervals (the window over which values in time were found for that address) and corresponding latencies for each address. Since the geometry and distance-to-time functions differ from one superlayer to the next, we do this separately for each superlayer. These results are then stored for every address into a calibration table, which is used for subsequent runs with the same geometry and timing parameters. The calibration table can be constructed from real beam data when they become available.

One important timing parameter that one could alter is the clock speed of the segment finder. The counter-based segment finder was tested at 7.4 MHz (134 ns/tick) and 3.7 MHz (269 ns/tick). Since the 2-bit counter frequency is fixed (higher counting frequency yields more counter bits for the same drift time and thus more than 16 bits of address), sampling at a higher frequency than the counting frequency does not yield much improvement in timing resolution of the segments.

To account for cell inefficiencies, the segment finder accepts not only segments with hits in all four layers, but also segments with hits in three out of four layers that have a valid parent with hits in all four layers. The valid parents are determined by iterating through all possible missed hits in the layer missed (including pivot cells in adjacent templates), adding each missed cell, and checking to see if this makes a valid parent. Using this method, 6517 of the 3/4 segment patterns can be calibrated by averaging over the latencies of all possible parents and recalculating σ appropriately. For the PT discriminator, the minimum and maximum ϕ average positions of the 4/4 parents for every 3/4 segment pattern with any calibrated 4/4 parent are stored.

Figure 5.5 shows the standard deviation of the latency for each address versus the number of times that particular address was obtained for the track trajectories used in the calibration procedure. We see that for addresses that occur frequently (towards the right side of the plot), we usually obtain a σ of less than about 67 ns (16 beam crossings). Thus an individual segment can determine the event time to an RMS (root mean square) better than 67 ns (see Appendix A). The position resolution of addresses that occur frequently is usually less than about 1 mm (see also Figure 5.5).

5.2.4 One-Shot Segment Finder vs. Counter-Based Segment Finder

Comparing the performances of the one-shot segment finder as introduced in Section 5.2.1 with the counter-based segment finder, the one-shot segment finder has several shortcomings:

- The one-shot segment finder has only very crude time information (accurate to one drift time) and thus a latency adjustment as introduced in Section 5.2.5 is not possible. This increases the event time jitter: The one-shot segment finder was found to have a jitter of about 400 ns [Chiam 95] even with no background sources present and without cell inefficiencies. On the other hand, the jitter for the counter-based segment finder is 181 ns for $B^0\overline{B}^0$ events (see Section 7.4.2) even with worst-case background and cell efficiency assumptions.

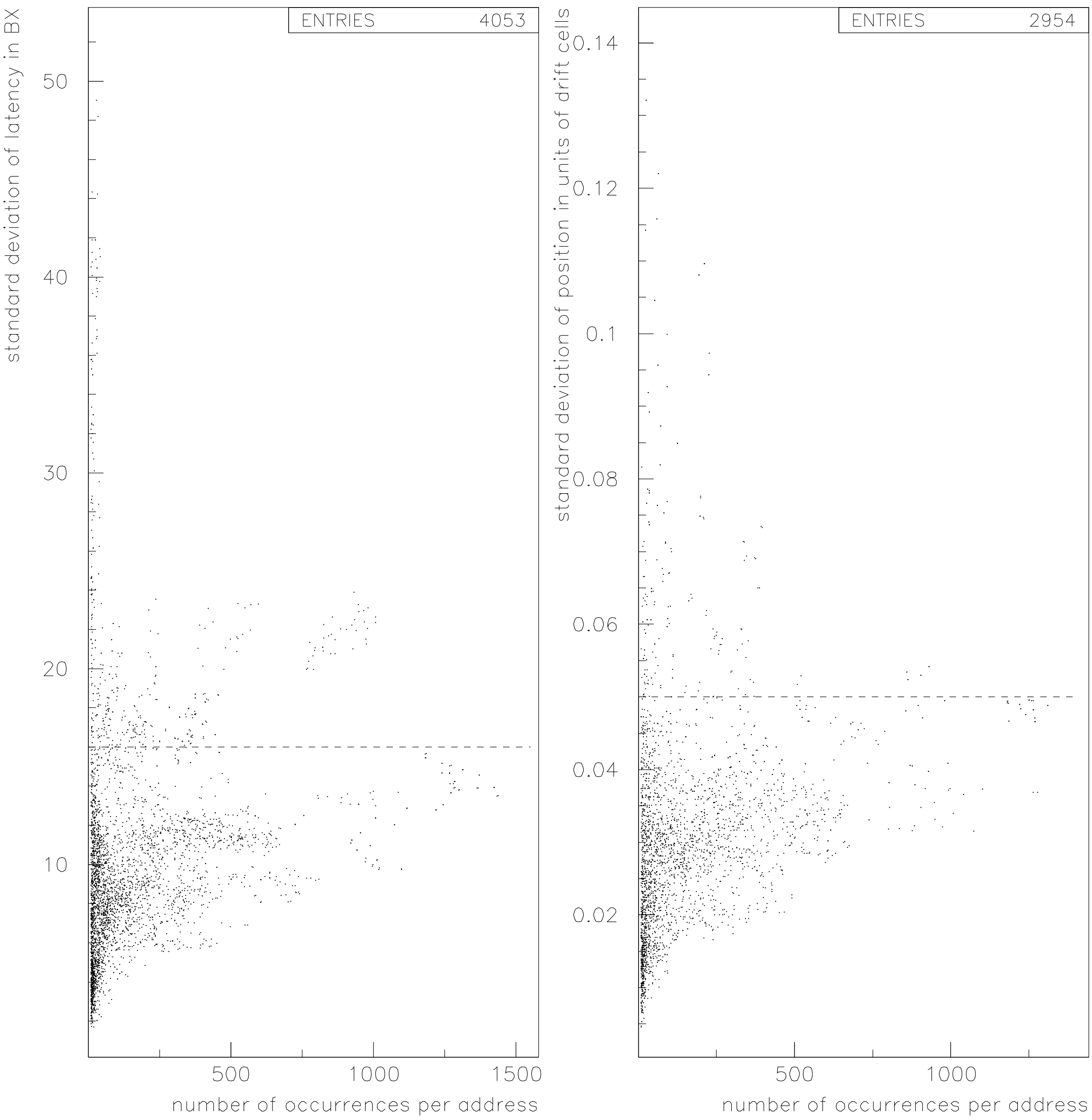

Figure 5.5: Time and position resolution of the segment finder. **Left:** Plot of the σ of the latency for an address in beam crossings versus the number of occurrences of that address in the calibration table. The dotted line indicates 16 beam crossings (67 ns). **Right:** Plot of the position resolution for an address in fractions of a drift cell versus the number of occurrences of that address. A drift cell is approximately 2 cm wide. The dotted line indicates a resolution of about 1mm.

- The ϕ position resolution for the one-shot segment finder is worse by a factor of 3 in comparison to the counter-based segment finder. This not only worsens the turn-on curve for PT discriminator, but also makes a primary z-position cut using segment finder information in Level 3 impossible (see Appendix A). Figure 5.6 illustrates the best and worst cases of position resolution for both segment finder types.
- The counter-based segment finder allows the Level 3 trigger to determine the event time accurate to 67 ns (see also Appendix A). There is no comparable algorithm available for the one-shot segment finder.

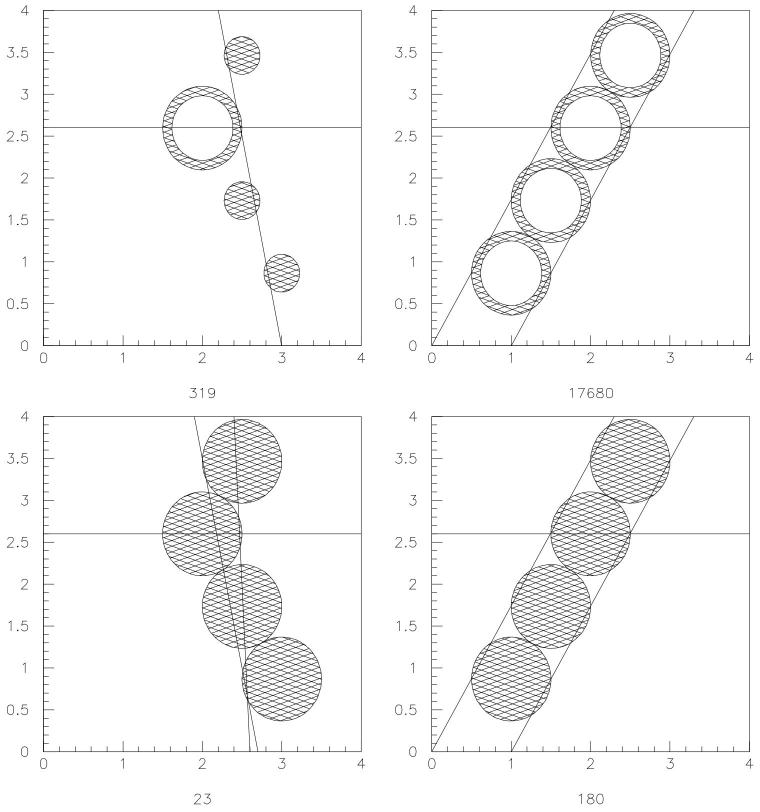

Figure 5.6: Segment patterns with good (left) and bad (right) position resolution for the counter-based segment finder (top) and the one-shot segment finder (bottom), respectively. The shaded area shows the allowed region for the track. Due to different counter values only parts of the drift cell are allowed for the counter-based segment finder. Address values under the graphs are indicated. The horizontal line indicates the pivot cell position; the calibration process measures the position of an average track through every pattern at the pivot cell level with respect to the pivot cell center.

The one-shot segment finder is simpler to build and needs less data bandwidth for the smaller size of the segment pattern addresses. On the other hand, the sampling rate of

3.7 MHz would have to be replaced with 7.4 MHz just to achieve the event time jitter of 400 ns quoted above. This doubles the bandwidth from the drift chamber endplate. The counter-based segment finder was chosen for its superior time and position resolution.

5.2.5 Priority Encoding

Since we sample the addresses at a rate of 3.7 MHz, a maximum drift time of around 600 ns (see Figure 2.5), corresponds to three ticks of the segment finder clock. Consequently, it is possible to get more than one valid address during an event (see track 3 in Figure 5.4).

We used 'priority encoded' addresses: that is, the segment finder waits until either a valid address is no longer found at a pivot cell, or the full drift time has elapsed, then picks the address that had the highest priority, i.e. the address with the best position information for the PT discriminator. Four priority levels were used for this purpose: 0 indicates no valid segment, 1 is a valid segment pattern without fine position information, 2 is a valid 3/4 segment pattern with fine position information available (see Section 5.4.1) and 3 denotes a 4/4 segment pattern with fine position available.

We adjust the transmission of each address to the subsequent algorithms such that there is a tick for which each of the priority encoded addresses coincide. Once the best addresses have been found, the addresses are stretched in time by the full 100% confidence width of the address and centered around the average latency for that address plus a fixed latency that is added for book-keeping purposes. This method is diagrammed in Figure 5.7. The algorithm runs at 7.4 MHz in order to adjust the latencies for the segments more precisely.

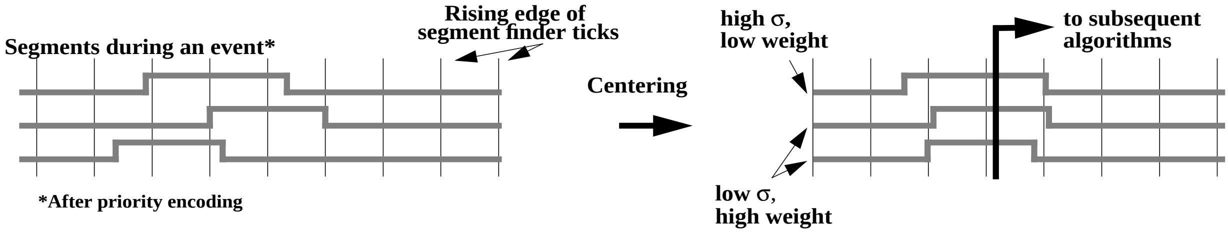

Figure 5.7: Centering of addresses assures coincidence in time. The addresses selected by the priority encoder are delayed until a fixed time and are turned on for the full 100% confidence width. These turned-on addresses are passed to subsequent algorithms.

In a final step, the latency adjusted segment hits are compressed per supercell (BLT data compress), picking latency and width of the segment with the highest weight per supercell. Fine position information is compressed in a similar way for the PT discriminator (see Section 5.4.2).

5.3 Binary Link Tracker (BLT)

5.3.1 Algorithm

The BLT uses a map of the supercell segment hits provided by the segment finder as input. Starting at the second superlayer, the BLT moves radially outward scoring segment hits per supercell when the current supercell and one of the supercells in the previous superlayer have been hit within a certain axial distance. The BLT looks for segment hits in the five closest neighbors in the previous superlayer. This accepts variations in both track curvature and dip angle where the latter leads to apparent rotation of the stereo layers. For some superlayer combinations with little difference in wire orientation, the number of neighbors to look for hits could be reduced. Operation of the BLT is shown in Figure 3.3.

To make the BLT robust against cell inefficiencies, supercell majority logic has to be applied. This is further discussed in the next subsection.

A track reaching superlayer 5 is counted as a B track and a track reaching superlayer 10 as an A track. These radial travel distances impose implicit momentum cuts on the A tracks and B tracks. With a magnetic field of 1.5 T, tracks reaching 80 cm have $p_\mathrm{t} > 180\,\mathrm{MeV}/c$ and tracks reaching 53 cm have $p_\mathrm{t} > 120\,\mathrm{MeV}/c$.

5.3.2 Impact of Cell Inefficiencies on the BLT

The studies in this section have been conducted using a non-tick-based version of the drift chamber trigger software package trgDC [trgDC 96a]. For the event generation, the simulation packages BEGET and BBSIM were used [BBSIM 96]. A slightly different drift chamber geometry and supercell division was used here. Additionally, the one-shot segment finder was used. But none of these differences affect the presented results.

Acceptance Studies of the BLT

The most suitable events to use for testing the fiducial acceptance of the BLT are single track events. Single muon events with an even distribution in ϕ, $\cos\theta$ and p_t in the range of 0 to $1\,\mathrm{GeV}/c$ were used.

The upper graph of Figure 5.8 shows the p_t turn-on curve for A tracks and B tracks[3]. The A′ tracks and the M clusters will be discussed in Section 5.4.2 and Chapter 7. Above $120\,\mathrm{MeV}/c$ for B tracks and above $190\,\mathrm{MeV}/c$ for A tracks, all tracks are found by the BLT if they satisfy $|\cos\theta| < 0.7$. In the lower graph the acceptance in θ is shown. One can see that B tracks cover a larger solid angle than A tracks because the B tracks can exit the drift chamber at superlayer 5.

---

[3] This is an updated picture using the full trigger simulation.

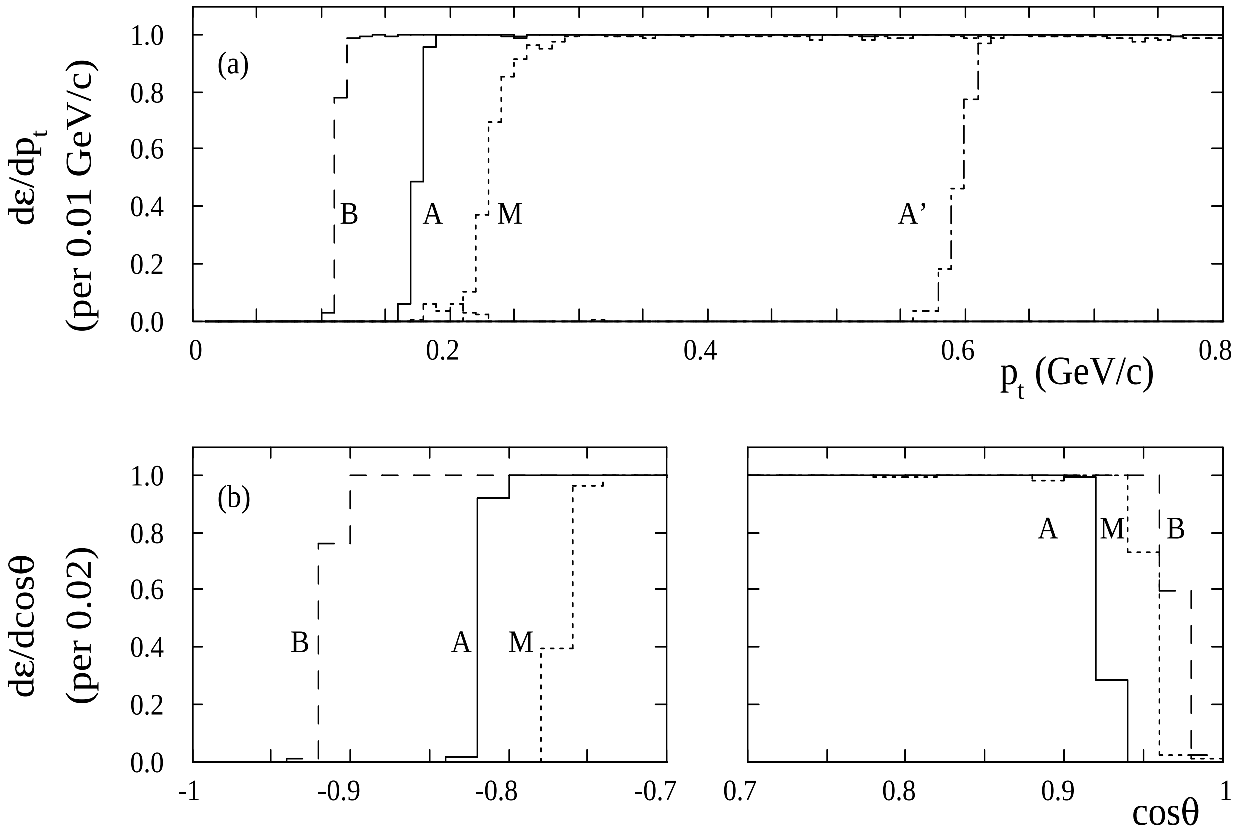

Figure 5.8: Differential efficiencies for single muons to be identified as trigger objects A, A$'$, B or M, as a function of (a) $p_{\rm t}$ with $|\cos\theta| < 0.7$ and (b) $\cos\theta$ with $p_{\rm t} > 0.4\,{\rm GeV}/c$, where 100% cell efficiency is assumed. A$'$ tracks are discussed in Section 5.4.2.

Cell Inefficiencies and BLT Performance

Making the drift chamber trigger model realistic one has to account for cell inefficiencies. A random cell inefficiency per hit has been introduced into the model. When tracks go through a cell, hits are scored once per cell and track traversal. Such hits are removed at random according to a predetermined probability (see Section 4.2.3).

One can predict the impact of cell inefficiencies on the BLT by using the binomial distribution. The probability of having a segment hit scored correctly is determined by the majority logic of the segment finder. A 3/4 or 4/4 segment pattern cause a segment hit. One can calculate the probability of failing to detect a segment hit by taking the probability to have an inefficient hit and use the binomial distribution to determine the probability of scoring a segment hit, i.e. to calculate the probability of having 3 or 4 out of 4 hits scored.

This probability is relevant for the BLT. If the BLT required all superlayers to contribute to build a track, the trigger track finding efficiency would decrease very fast with decreasing cell efficiency (see curve labeled “1 perm” in Figure 5.9). The trigger efficiency calculated here is the efficiency to detect an A track. So supercell majority logic has to be applied to the BLT. The next step is to allow one superlayer to be skipped. This results in 11 different BLTs. The first one is the BLT where superlayer 1 is skipped, second one skips superlayer 2 ... and the 11th BLT uses all superlayers. The trigger efficiency for this version is also shown in Figure 5.9, labeled “11 perm”.

In order to increase the trigger efficiency further without applying too loose a condition for B tracks, we allow 1 superlayer to be skipped in superlayers 1–5 and another superlayer in superlayers 6–10. This results in 35 different BLTs[4]. An even looser BLT that would allow 2 layers to be skipped anywhere results in 47 BLTs, if no two layers can be skipped in a row. The trigger efficiencies for these versions are also shown in Figure 5.9. The default chosen is 35 permutations [Kral 94b][5] since this version gives trigger efficiencies above about 95% for 90% cell efficiency. Also, it still requires 4 scored segments for a B track, unlike the 47-permutation version, thus making it more robust against potential backgrounds. The curves in Figure 5.9 were well reproduced using single muons in the simulation. Allowing superlayer skips also results in additional logic producing the ϕ maps for the counting layers. If the counting layer itself was skipped, the supercell from the previous superlayer has to set the bit for the counting layer (bumping).

Table 5.1 shows trigger efficiencies for the 3A trigger on a B physics benchmark process. Assuming a 90% cell efficiency (and no background), the trigger efficiency for A tracks is improved significantly allowing 2 layers to be skipped, as in the 35-permutation version.

---

[4] The permutation skipping superlayer 5 and 6 is excluded.

[5] The studies in [Kral 94b] were conducted with 36 permutations, thus allowing the combination of simultaneously skipping superlayers 5 and 6.

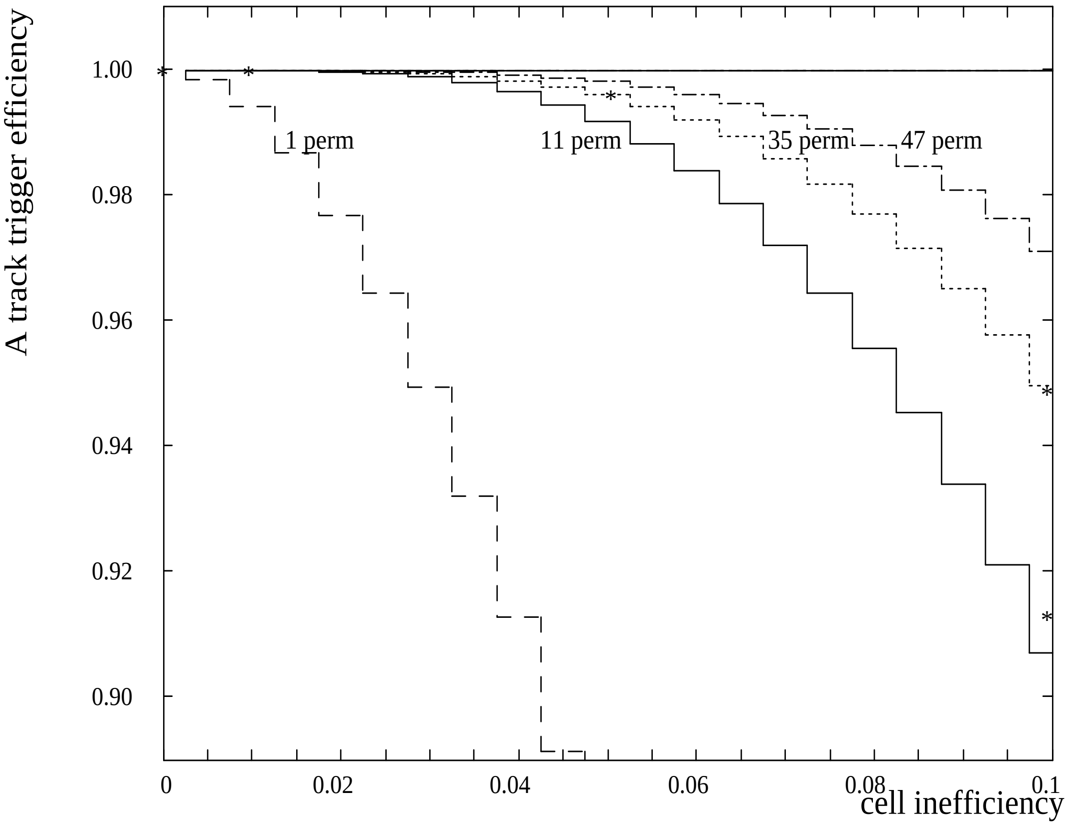

Figure 5.9: Calculated A track trigger efficiencies for various BLT versions. These curves were produced using binomial distributions. The stars (*) reflect data points using single muon events with $|\cos\theta| < 0.7$ and $p_{\rm t} > 0.3\,{\rm GeV}/c$.

Cell Efficiency:	100% (35perm)	90% (35perm)	90% (11perm)
$B^0 \to \pi^+\pi^-$, $\overline{B}^0 \to \mu$X	0.93	0.91	0.89
normalized efficiency	1.00	0.98	0.96

Table 5.1: 3A trigger efficiency for the drift chamber for two BLT versions. 1000 events were generated. Normalized efficiencies are relative to the 100% cell efficiency case, with no fiducial cuts applied.

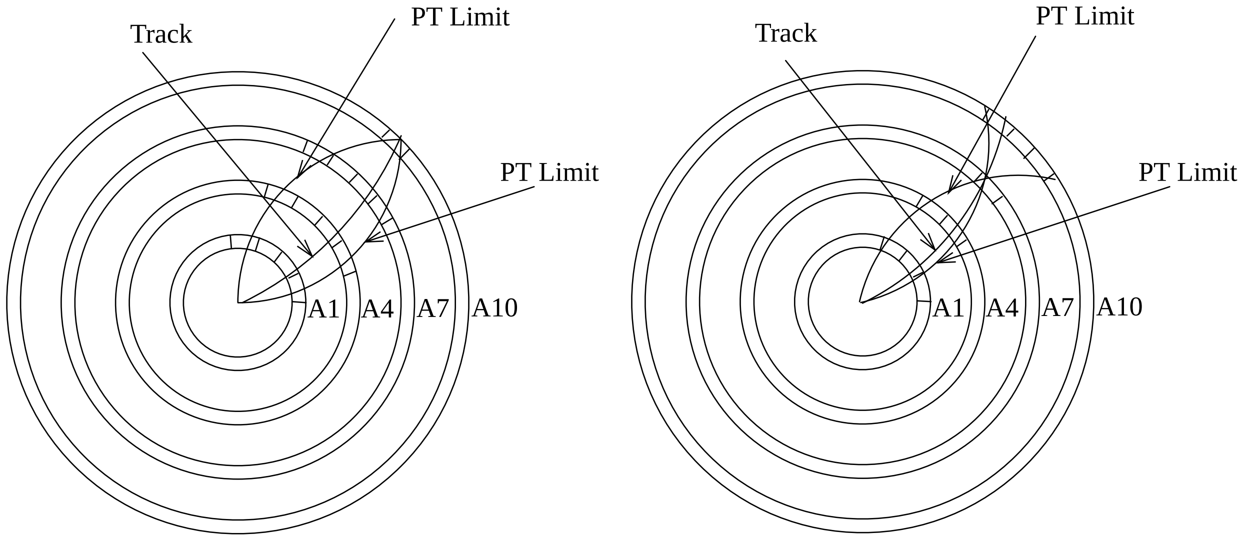

Figure 5.10: PT discriminator geometry in an x-y view of the drift chamber. In this picture, superlayer 10 (left) and superlayer 7 (right) were chosen as seed layers.

5.4 PT Discriminator

5.4.1 Basic PT Discriminator

The purpose of the PT discriminator is to determine whether the transverse momenta of found tracks are above a specified p_{t} limit or not. No pattern recognition is performed here. The basic idea to find the transverse momentum is to determine the radius of the track. Using the radius one can calculate p_{t} via $p_t = 2.998 \cdot \frac{B}{\mathrm{T}} \cdot \frac{r}{\mathrm{cm}}$ MeV/c. Energy losses in the drift chamber due to ionization (dE/dx) are well below 100 keV/cm for relevant transverse momenta and particles. Hence they can be neglected here.

In order to determine the radius of the track one takes 3 points on the arc of the track: these uniquely specify a circle. The hits in the axial superlayers deliver good spatial resolution since these wires have constant positions in the x-y-plane, unlike the stereo layers. Due to the cell geometry, trigonometric manipulations and pattern recognition would have to be applied to the stereo-layers in order to use them. Including the assumed beam vertex position, up to five points are available to determine p_{t}.

Some of the segment patterns mentioned above report calibrated axial fine positions, i.e. their position is known precisely with respect to the pivot cell. These fine positions are stored for every segment pattern to a certain accuracy (e.g. 4 bits yielding 14 different fine positions). To determine p_{t}, one takes the assumed beam vertex position, a segment in the seed layer (superlayer 10) and looks for segments in the other axial superlayers within the limits imposed by the minimum transverse momentum (see Figure 5.10). These limits are stored as a table for every fine position in the seed layer.

The implementation of the PT discriminator described so far shows a strong susceptibility to cell inefficiencies because:

- It requires a calibrated segment pattern in the seed layer and in the other axial layers.
- All fine position points in the axial superlayers must be within the bounds.

Both requirements are loosened. For the second case we introduce a looser criterion where just 2 out of the 3 superlayers in between must be within the bounds. The actual algorithm counts the number of layers with hits found within the p_t limits (scored layers) and compares it to a programmable number.

In order to avoid a preference for the seed layer, we also admit superlayer 7 as seed layer (see Figure 5.10, right picture). Otherwise a p_t discrimination is not started in case of missing fine position information in superlayer 10. As a variation, one could also admit superlayers 4 and 1 as seed layers.

A significant improvement of the trigger efficiency is achieved by admitting 3/4 segment patterns to determine p_t. One can admit these without loss in resolution provided there are calibrated 4/4 segment patterns that can be reconstructed out of the 3/4 segment patterns (see Section 5.2.3). If multiple 4/4 segment patterns can become a 3/4 segment pattern upon loss of a hit, the worst case is assumed. This means when looking at the right border, the fine position of the leftmost segment pattern is taken and vice versa. This way 3/4 patterns that are neighbors of 4/4 patterns (due to the overlap of the templates) do not admit additional points. If the pivot cell in a template is missing the actual position of a 3/4 pattern can be outside a particular pivot cell locus.

5.4.2 PT Discriminator Demonstration

Parameters for the PT Discriminator

There are six parameters that can be varied in potential PT discriminator algorithms:

- **Number of bits to store the fine position**: An increasing number of bits increases the spatial resolution and hence the p_t resolution. Every bit also doubles the size of the lookup table with the boundaries. Four bits are used in the current implementation.
- **Minimal p_t**: This denotes the threshold value above which tracks are marked as A′ tracks. The current default is 0.8 GeV/c.
- **Algorithm switch**: In order to suppress unexpectedly large backgrounds, there might be a desire to turn off the use of 3/4 segment patterns. Use of 3/4 segment patterns is the default.
- **Number of superlayers, N_{SL}**: To allow missing hits one can allow one of the superlayers to be missing, leaving two combinations of superlayers to determine p_t. The default allows one missing superlayer, i.e. requires fine position of three superlayers per A′ track.

- **Number of seed layers,** N_{seed}: Every axial superlayer can play the role of the seed layer. However, the resolution worsens when one uses the innermost axial superlayers as seed layers. As a default, only superlayers 10 and 7 are used as seed layers.
- **Compression of fine position information:** The transmission of all fine position information from all pivot cells in axial superlayers results in too much data bandwidth. Data reduction is needed. The next natural choice is just sending one fine position information per supercell. This results in a manageable data transfer rate and does not reduce the efficiency of the PT discriminator. Another scheme with even less data bandwidth would be to send one fine position for every second supercell. Studies showed a 0.5% drop in efficiency for 2-prong $\tau^+\tau^-$ events due to the fact that parts of both prongs ended in adjacent supercells. Compression per supercell was chosen as the default.

The upper graph of Figure 5.8 on page 47 shows the p_{t} turn-on curve for the default configuration of the PT discriminator, except that the p_{t} threshold was set to $0.6\,\text{GeV}/c$. The A$'$ tracks found around $0.2\,\text{GeV}/c$ are caused by loopers admitted by the fact that limited pattern recognition is applied in this PT discriminator algorithm. Particles in this momentum region have enough momentum to reach the outermost drift chamber layer but do not reach the calorimeter because the Lorentz force keeps them on a circular orbit. This causes a lot of hits in the drift chamber. Sometimes they produce a pattern that satisfies the PT discriminator condition.

The minimal p_{t} value is used to suppress background. The algorithm switch, the number of superlayers, and the number of seed layers are parameters that are useful only when cell inefficiencies are present; they are investigated in Section 5.4.3.

Choosing the Number of Bits to Store Fine Position

This section investigates the effect of varying the number of bits to store the fine position of the calibrated segment patterns. One effect is that the lookup table for the boundaries doubles its size with every bit added, leading to a desire to keep the bits few. However, the number of bits to store the fine position of the calibrated segment patterns limit the resolution and the sharpness of the turn-on curve. The calibrated ϕ positions have a standard deviation of less than about 0.05 cell widths with the counter-based segment finder. Thus a division of the cell into more than 20 fine positions does not improve the resolution much. In Table 5.2 one can see that the increase from 4 to 5 bit resolution doesn't significantly increase the sharpness of the turn-on curve.

Performance of the PT Discriminator

This section shows the performance of the PT discriminator on some physics benchmark processes and on the dominant drift chamber trigger background source, hadronic lost-particle backgrounds.

Number of bits	1	2	3	4	5
Number of ϕ slices per cell	1	2	6	14	30
${}^{90}_{10}\Delta p_{\mathrm{t}}$ (counter-based) [MeV/c]	165	90	40	30	25
${}^{90}_{10}\Delta p_{\mathrm{t}}$ (one-shot) [MeV/c]	165	110	75	62	60

Table 5.2: Change in p_{t} for a 10% to 90% rise in efficiency (${}^{90}_{10}\Delta p_{\mathrm{t}}$) for different numbers of bits to store the fine position. The turn-on curves were produced using single muon events with $|\cos\theta| < 0.7$ and found A tracks. For comparison also the values for the one-shot segment finder are included. The p_{t} cut was set to 0.6 GeV/c. The number of ϕ slices is $2^n - 2$ where n is the number of bits.

The main purpose of the PT discriminator is to discriminate background causing open drift chamber triggers against low-multiplicity physics events (mainly $\tau^+\tau^-$ events). These background events are mostly due to lost beam particles (see Section 4.2.4). The hadronic background rates quoted in this and the next subsection are lower than the simulation results shown in Chapter 7 because the hadronic events here were generated with a less detailed interaction region model. Note that the one-shot segment finder was used for these studies. The conclusions drawn from these studies also apply to the counter-based segment finder.

In Table 5.3, open trigger (D_2) and D_2' trigger efficiencies for several τ benchmark processes and hadronic background are shown. The normalized efficiency is calculated with respect to the open trigger efficiency. This number is an upper bound on how little physics is lost by applying a p_{t} cut since it is calculated with respect to the loosest trigger criterion, before fiducial cuts used in a physics analysis. From the table, one can conclude that up to a p_{t} cut of about 0.8 GeV/$c$trigger efficiency for $\tau^+\tau^-$ events is sufficiently high.

Trigger Criterion:	D_2	D_2' (0.4 GeV/c)	D_2' (0.6 GeV/c)	D_2' (0.8 GeV/c)
$\tau^+ \to e^+\nu\bar{\nu}$, $\tau^- \to \mu^-\bar{\nu}\nu$	0.81	0.79	0.75	0.72
normalized efficiency	1.00	0.97	0.93	0.89
$\tau^+ \to \pi^+\bar{\nu}$, $\tau^- \to \pi^-\nu$	0.90	0.89	0.87	0.83
normalized efficiency	1.00	0.99	0.96	0.92
Hadronic Background ×10	4670 Hz	2720 Hz	1560 Hz	980 Hz

Table 5.3: Trigger efficiencies for the drift chamber under different trigger criteria. For each benchmark process 1000 events were generated and no fiducial cuts were applied. 6000 hadronic background events passed the open trigger. The default PT discriminator was used.

5.4.3 Impact of Cell Inefficiencies on the PT Discriminator

In this section the parameters introduced in Section 5.4.2 are further discussed and their tradeoffs are shown in the face of cell inefficiencies, simulated as described in Section 4.2.3.

Using 3/4 Segment Patterns for the PT Discriminator

The algorithm switch for using 3/4 segment patterns introduced in Section 5.4.2 is very efficient. In Table 5.4 one can see that the trigger efficiency on single muons improves dramatically. On the other hand, the increase in background rate is acceptable. Therefore all further studies make use of 3/4 segment patterns.

Algorithm Switch:	use 3/4 patterns	use only 4/4 patterns
$N_{\mathrm{SL}} = 3, N_{\mathrm{seed}} = 2$	1.00	0.99
$N_{\mathrm{SL}} = 4, N_{\mathrm{seed}} = 2$	0.99	0.86
Hadronic Background ×10, $N_{\mathrm{SL}} = 3, N_{\mathrm{seed}} = 2$	1560 Hz	1460 Hz

Table 5.4: Drift chamber A′ track trigger efficiency of the PT discriminator for single muons. For the efficiency calculation, all events with $p_{\mathrm{t}} > 0.7\,\mathrm{GeV}/c$ and with $|\cos\theta| < 0.7$ contributed. The cell efficiency for the muons was set to 99%, whereas the hadronic background rates are at 100% cell efficiency. The p_{t} cut was set to $0.6\,\mathrm{GeV}/c$.

Number of Seed Layers and Number of Layers Used

This section covers the variation of the two remaining parameters of the PT discriminator. These are the required numbers of superlayers, N_{SL}, and seed layers, N_{seed}.

Table 5.5 shows the trigger efficiencies for the τ benchmark processes and for single muons at 95% cell efficiency as well as the rates for hadronic background. The normalized efficiency is relative to the trigger efficiency for the open trigger at 100% cell efficiency.

One can see that in order to achieve a normalized trigger efficiency for $\tau^+\tau^-$ events above about 95% it is necessary to require only 3 axial layers ($N_{\mathrm{SL}}= 3$) although the background rates for that case are higher. The default to use 2 seed layers ($N_{\mathrm{seed}}= 2$) was chosen to keep the background rates sufficiently low. Furthermore, it simplifies the hardware design of the PT discriminator.

If the cell efficiency turns out to be significantly above 95 % and the background rates are as high as 10 times the nominal values, the case with all 4 axial superlayers used would be interesting. This parameter is completely programmable and does not affect the electronics design of the PT discriminator.

The background rates for the cases when only 3 axial superlayers are used are so high because often there is an accidental alignment of different tracks that produce a pattern where 3 out of 4 axial superlayers report a fine position within the p_{t} bounds. This increase due to accidentals could be reduced by applying pattern recognition to the PT discriminator, thus suppressing unrelated hits (zig-zag patterns). Preliminary studies on pattern recognition showed that the reduction in background can be about 20%. But a pattern recognition algorithm built in hardware is significantly more complex, so this option is not further pursued here.

It is desirable to build a flexible PT discriminator to be able to adjust for a given background rate and cell efficiency. Like for the BLT, such flexibility increases the complexity of the PT discriminator logic.

$\tau^+ \to e^+\nu\bar{\nu}$, $\tau^- \to \mu^-\bar{\nu}\nu$	$N_{\mathrm{seed}} = 2$	$N_{\mathrm{seed}} = 3$	$N_{\mathrm{seed}} = 4$
$N_{\mathrm{SL}} = 3$	0.74	0.75	0.75
normalized efficiency	0.91	0.93	0.93
$N_{\mathrm{SL}} = 4$	0.69	0.71	0.72
normalized efficiency	0.86	0.88	0.89
$\tau^+ \to \pi^+\bar{\nu}$, $\tau^- \to \pi^-\nu$	$N_{\mathrm{seed}} = 2$	$N_{\mathrm{seed}} = 3$	$N_{\mathrm{seed}} = 4$
$N_{\mathrm{SL}} = 3$	0.86	0.86	0.87
normalized efficiency	0.95	0.95	0.96
$N_{\mathrm{SL}} = 4$	0.81	0.82	0.83
normalized efficiency	0.90	0.91	0.91
Single Muons	$N_{\mathrm{seed}} = 2$	$N_{\mathrm{seed}} = 3$	$N_{\mathrm{seed}} = 4$
$N_{\mathrm{SL}} = 3$	0.97	1.00	1.00
$N_{\mathrm{SL}} = 4$	0.92	0.94	0.95
Hadronic Background ×10	$N_{\mathrm{seed}} = 2$	$N_{\mathrm{seed}} = 3$	$N_{\mathrm{seed}} = 4$
$N_{\mathrm{SL}} = 3$	1560 Hz	1630 Hz	1910 Hz
$N_{\mathrm{SL}} = 4$	980 Hz	1080 Hz	1290 Hz

Table 5.5: Trigger efficiencies with a p_{t} cut of 0.6 GeV/c for τ benchmark processes (top), A′ trigger efficiencies for single muons (middle) and hadronic background rates (bottom). The tau and muon events were simulated with 95% cell efficiency, whereas the background rates were for 100% cell efficiency. For each τ process 1000 events were generated and used without fiducial cuts. 25000 events were generated for the single muons. 6000 events passed the open trigger for the hadronic background. Normalized efficiencies are relative to the open trigger efficiency at 100% cell efficiency.

5.4.4 Background Rejection Power of the PT Discriminator

This section demonstrates the background rejection power of the PT discriminator using the full tick-based simulation model. In addition, updated background simulations are used.

The main purpose of the PT discriminator in the drift chamber is to discriminate physics events from photoproduced hadronic background events. Putting a momentum cut on an A track proves to keep most of the physics with a p_{t} cut up to 800 MeV/c [Gehrig 96a]. In Figure 5.11, background rejection power versus p_{t} for several trigger lines is shown. `OR`-ing a higher multiplicity trigger line like 3A with a trigger condition using A′ tracks yields high trigger efficiencies and keeps the background rate low (see Section 7.3.3).

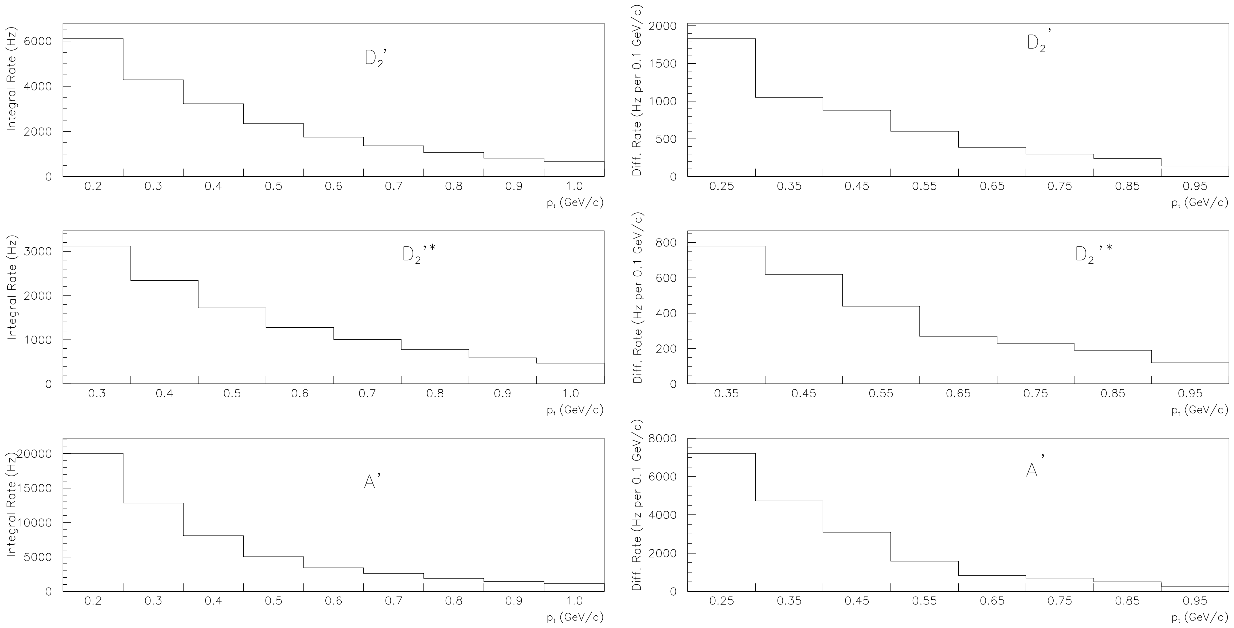

Figure 5.11: Background rates at ×11 nominal conditions (photoproduction cross sections ×10 enhanced overlayed with nominal vacuum background) for various trigger lines and different p_{t} cuts. The values for 200 MeV/c are the rates without p_{t} cut (A tracks have an implicit p_{t} cut of about 200 MeV/c). Left are integral rates, right are differential rates. Trigger lines shown are D'_2, D'^{*}_2, and A$'$ trigger, an unrealistic but instructive one-track trigger. The same 20000 events with one photoproduction interaction in each, overlayed with nominal occupancy backgrounds, were used for all runs. These data were obtained using the final algorithms and a detailed background simulation, like in the next chapter.

Chapter 6

Global Trigger Algorithms

6.1 Global Trigger Overview

The trigger decisions are made in the global trigger. Based on multiplicity and topology of an event, the global trigger accepts or rejects the event for 30 individual multiplicity or topology cuts, i.e. trigger lines.

The global trigger receives the trigger objects found by the drift chamber trigger and the calorimeter trigger. The ϕ bins are stretched based on the intrinsic jitter of each object to ensure coincidence of all trigger objects belonging to the same event for at least one 7.4 MHz tick. Using these ϕ maps the trigger objects are counted. For track-cluster-matched objects the match is performed before counting. However, the current simulation does not use track-cluster matches.

Trigger decisions are made by determining whether the multiplicity counts of the trigger objects are above a pre-set threshold for each trigger line. In a subsequent process, all trigger lines are centered in time and stretched based on their intrinsic jitter to ensure coincidence.

In a separate path, the trigger line with the best timing information is selected to send the event time estimate to the Fast Control System as a single 15 MHz tick. This whole process is illustrated in Figure 6.1.

6.2 Global Trigger Algorithms

6.2.1 Input to the Global Trigger

The input to the global trigger consists of 16 bins in ϕ for A, A$'$, and B tracks, 20 bins in ϕ for M, G, E, and X clusters, and 10 bins in ϕ for Y clusters. In addition, there is a 2-bit input line from the Instrumented Flux Return that indicates the presence of one or more tracks in the muon and neutral hadron detector. That signal could potentially be used to select cosmic rays for detector calibration studies.

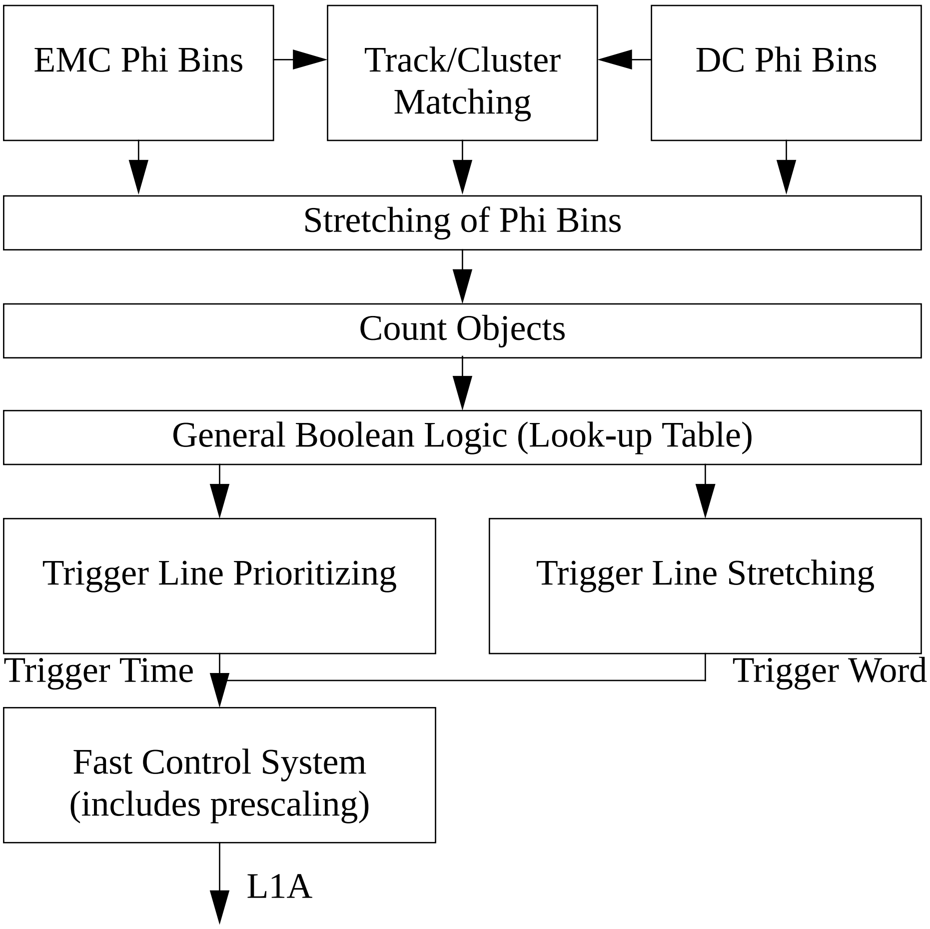

Figure 6.1: Block diagram of the functions of the global trigger.

6.2.2 Phi Map Centering and Stretching

Since the raw ϕ maps sent to the global trigger can stay on for different numbers of ticks and might also reach the trigger at different times, the ϕ maps are centered by first looking for the trailing edge of the raw ϕ maps, and then calculating the time center. These centered maps are subsequently stretched with a certain time for every type of object, to ensure coincidence among the objects for at least one tick. It is also possible to adjust the latencies in this step, if certain objects appear at different times than others. This process is very similar to the latency adjustment step in the priority encoding of the segments (see Section 5.2.5).

6.2.3 Object Counting and Matching

Drift chamber and calorimeter algorithms operate on bit maps with 32 and 40 ϕ slices, respectively. As a final step in the calorimeter, two adjacent ϕ bins are simply `OR`-ed before they are sent to the global trigger, so the counting algorithm for clusters requires one empty bin between two entries when counting entries in the ϕ map. However, in the drift chamber, a veto signal prevents turning on two ϕ bins in the 16-fold reduced map sent to the global trigger if there are 2 adjacent ϕ bins turned on in the 32-fold ϕ map (see step Compress 2:1 in Figure 5.1 on page 38). Thus, counting drift chamber objects in the global trigger does not require an empty bin between objects when counting track multiplicities.

Topology cuts are implemented with a modified counting algorithm. Instead of not requiring any ϕ bin separation in the drift chamber or only one ϕ bin separation in the calorimeter, one requires a certain number of ϕ bins between two set bins, which is equivalent to a certain angular separation. Typically topology cuts require a multiplicity count of two. Higher counts could be used to ensure an isotropic distributions of charged tracks or energy deposits in the event. Track-cluster matching is not implemented for the studies shown here. The counting algorithms mentioned above will be implemented in a memory lookup table [Jared 96].

6.2.4 Trigger Decision

The trigger decision logic is implemented in a completely programmable way as a hardware lookup table with 24 bits of object count input and 30 bits of trigger line output. Depending on the number of objects, a trigger decision is made. See Table 3.4 in Section 3.3.1 for a sample list of trigger criteria.

6.2.5 Event Time Determination

The trigger has 30 different trigger lines. After the determination whether a particular trigger line passed or failed, the event time determination logic looks for the trigger line with the highest priority to determine the event time. This search times out at the maximum allowed time jitter and is re-enabled after a higher prioritized trigger line turns on. From this trigger line, the time center is determined at a 15 MHz clock rate to accommodate "half" ticks. This signal is delayed such that it reports the Level 1 Accept signal at the maximum allowed latency for the trigger system, minus the time jitter associated with that trigger line. This reduces event-by-event hit poisoning in the silicon vertex tracker to a minimum (see Section 7.4.1).

Parallel to finding the event time, the time centers of all other trigger lines are also determined. These signals are then centered and stretched to ensure that all trigger lines belonging to an event are turned on when the trigger word is sent out. Note that this stretch is independent of the time jitter for each trigger line, so it can be done conservatively to guarantee overlaps without increasing the event time jitter. Again, the process of centering and stretching is analogous to the centering and stretching of the ϕ bins in Section 6.2.2.

6.2.6 Output from the Global Trigger

The global trigger output to the Fast Control System (FCS) consists of the trigger signals of the 30 trigger lines, in a single trigger word, which is sent for one 15 MHz tick. This constitutes the event time estimate as well. The final Level 1 Accept signal is produced in the FCS after prescaling of the trigger lines.

The FCS requires two Level 1 Accept signals to be separated by at least $2.2\,\mu$s. This incurs a deadtime of less than 0.5% at the maximum Level 1 trigger rate of 2 kHz. The Level 1 trigger system itself requires the triggers to be more than $1\,\mu$s apart, which would lead to a maximum deadtime of about 0.2% inherent in the global trigger algorithm.

Chapter 7

Results on Efficiency, Rate and Jitter

7.1 Overview

This chapter describes the simulation results using the complete tick-based model of the Level 1 trigger, including the calorimeter trigger. The next section gives error estimates on the simulation results, followed by the results on trigger efficiency and trigger rates for various scenarios. In the last section results on event time jitter are presented.

7.2 Error Estimates on Simulation Results

Since all results presented are derived from simulations no measurement errors apply. Yet there are systematic errors due to uncertainties in the simulation model and statistical errors due to limited sets of events.

7.2.1 Systematic Errors

There are three main quantities evaluated in the simulation: trigger efficiency, trigger rate and event time jitter. The trigger efficiency has only a small systematic uncertainty which is due to limitations in the detector model geometry, GEANT particle tracking accuracy and uncertainties in the predictions of the overlayed background.

The trigger rates due to bhabha scattering has a relatively small systematic error and agrees with the calculated integrated cross section taking the detector's acceptance into account (see Table 1.1). The main uncertainty for the trigger rates is the lost beam particle background, which unfortunately contributes the most to the trigger rate.

Various simulation models exist to simulate lost-particle background. For hadronic showers, several particle generators were tested and agreed to within 30% in the momentum region below $1.25\,\mathrm{GeV}/c$ [Gheri 95]. Most of the particles produced in lost-particle hadronic interactions lie below this threshold. The photoproduction model GELHAD has not been extensively compared to data and could have a large error. Comparison of experimental data of lost beam particles from the TPC experiment at SLAC and GEANT simulations showed that the triton and alpha production rates are too high in the simulation. However, the total baryonic production rate was found to be in good agreement.

Another major uncertainty is the beam-gas pressure profile for the interaction region, which scales the rate of lost beam particles.

Taking all these uncertainties into account, the results presented include worst-case studies, where the rate of lost beam particles production is multiplied by ten (Vacuum ×10) or the cross section for photoproduction interactions is multiplied by ten (Photoprod. ×11). Note that the silicon vertex tracker data taking is severely compromised by occupancy in the Vacuum ×10 scenario. Thus this is a worst-case scenario for the running of *BaBar* and consequently a useful design point for the trigger.

The event time jitter associated with physics events is based on triggered events. Hence the same systematic uncertainties as for the trigger efficiency apply. A small additional error is introduced by taking electronic noise in the front-end electronics system into account (parts of these errors are simulated and were found to have a negligible contribution).

7.2.2 Statistical Errors

Statistical errors on the trigger efficiency, $d\varepsilon$, are taken to be binomial,

$$d\varepsilon = \sqrt{\left(\frac{\varepsilon(1-\varepsilon)}{N_{\text{total}}}\right)}. \tag{7.1}$$

N_{total} is equal to the number of generated events or the number of generated events in the fiducial volume, respectively.

Statistical errors are not quoted in the tables presented here. For all physics events always at least 1000 events were generated; in most cases more than 500 events were in the fiducial acceptance. With efficiencies typically above 80% the statistical error on the trigger efficiencies quoted is less than 2%. To accommodate this error, no sub-percent values are quoted. Event time jitter results are based on at least 5000 events without fiducial cuts. Thus the quoted 99% confidence level is expected to be independent of the event set.

Statistical errors on trigger rates are proportional to $1/\sqrt{N_{\text{trig}}}$, where N_{trig} is the number of triggered events. For the hadronic background simulation with enhanced photoproduction cross-section, one event represents about 7 Hz of the trigger rate, so statistical errors are less than 10% for trigger rates above 700 Hz. For the simulation of lost beam particles, on the other hand (Vacuum ×10 and Vacuum nominal), one event represents 70 Hz, i.e. 14 ms of background was simulated. Thus the statistical errors on the trigger rates under worst-case studies can be up to 25%. Despite the high uncertainty, the systematic uncertainties still dominate.

7.3 Trigger Efficiencies and Background Rates

This section starts with studies of the impact of cell efficiencies on trigger efficiencies. For the remainder of this section trigger efficiencies and rates under different running conditions are shown. These studies include nominal running conditions, ×10 running conditions, and cases where one detector subsystem does not deliver trigger data. Trigger efficiencies for $\gamma\gamma$ physics are shown separately. Also, a special trigger strategy yielding low trigger rates is shown.

Drift chamber cell inefficiencies and backgrounds are simulated as described in Chapter 4. To promote a photon-to-hadron conversion in the simulation in worst-case studies, the cross sections of photoproduction were enhanced by a factor of 10. Events from these interactions overlayed with lost beam particle background at nominal vacuum are referred to as "Photoprod. ×11" background in the trigger rate tables.

An additional 5 Hz rate of random triggers for monitoring and an additional rate of about 15 Hz of asymmetric Bhabha triggers that triggered the Y trigger but not any other trigger criterion have to be added to the total rate quoted in the below tables.

7.3.1 Impact of Cell Inefficiencies on Trigger Efficiencies

Table 7.1 shows trigger efficiencies for $\tau^+\tau^-$ events using different drift chamber cell efficiencies. The track linker has majority logic incorporated. Hence the open trigger efficiency does not degrade as much as the D_2' trigger efficiency, since the latter uses the PT discriminator which relies on fine position information from the supercells of the drift chamber. As can be seen, a cell efficiency below 95% compromises τ physics significantly if the PT discriminator is used. Current cell and electronics simulations [Innes 96] show that the drift chamber cell efficiency should be above 99%. The default p_t cut of 0.8 GeV/c was used.

Drift Chamber Trigger Efficiencies versus Cell Efficiency

	$4\,\pi$			Fiducial volume		
$\tau^+ \to \pi^+\bar{\nu}$, $\tau^- \to \pi^-\nu$	D_2	D_2'	$\mathrm{D}_2'^*$	D_2	D_2'	$\mathrm{D}_2'^*$
Cell efficiency 99 %	0.89	0.77	0.73	0.99	0.91	0.88
Cell efficiency 95 %	0.89	0.73	0.69	0.99	0.88	0.84
Cell efficiency 90 %	0.85	0.64	0.61	0.95	0.78	0.75

Table 7.1: Trigger efficiencies for drift chamber trigger lines for the benchmark process $\tau^+ \to \pi^+\bar{\nu}$, $\tau^- \to \pi^-\nu$. The same 1000 generated events were used for each run.

7.3.2 Nominal Running and ×10 Background Conditions

Under nominal running conditions we assume that the drift chamber cells are 99% efficient [Innes 96], and that lost beam particle backgrounds are predicted by the current simulation model. Table 7.2 shows trigger efficiencies for B and τ benchmark processes and trigger rates for nominal running conditions. The simple open trigger meets and exceeds all requirements: the total trigger rate is well below 2000 Hz while the trigger efficiency is 100% for all B and τ benchmark processes.

Nominal Trigger Efficiencies

	$4\,\pi$			Fiducial volume		
Process	D_2	C_2	C_2+D_2	D_2	C_2	C_2+D_2
$B^0 \to \pi^+\pi^-$, $\overline{B}^0 \to \mu X$	1.00	0.99	1.00	1.00	0.99	1.00
$B^0 \to D^+D^-$, $\overline{B}^0 \to X$	1.00	1.00	1.00	1.00	1.00	1.00
$B^+ \to \tau^+\,\nu$, $B^- \to X$	1.00	1.00	1.00	1.00	1.00	1.00
$\tau^+ \to e^+\nu\bar{\nu}$, $\tau^- \to \mu^-\bar{\nu}\nu$	0.77	0.70	0.80	0.98	0.96	1.00
$\tau^+ \to \pi^+\bar{\nu}$, $\tau^- \to \pi^-\nu$	0.87	0.73	0.91	0.99	0.90	1.00

Nominal Trigger Rates

Process	D_2	C_2	C_2+D_2
$\Upsilon(4S)$ resonant	4 Hz	4 Hz	4 Hz
$q\bar{q}$	8 Hz	8 Hz	8 Hz
$\mu^+\mu^-$	2 Hz	2 Hz	2 Hz
$\tau^+\tau^-$	2 Hz	2 Hz	2 Hz
$\gamma\gamma$ signal	3 Hz	3 Hz	3 Hz
Bhabha	114 Hz	132 Hz	140 Hz
$\gamma\gamma$ background	50 Hz	50 Hz	50 Hz
Vacuum nominal	510 Hz	180 Hz	690 Hz
Beam-gas 10 nTorr	16 Hz	7 Hz	18 Hz
Cosmic Rays	140 Hz	500 Hz	550 Hz
Total nominal	849 Hz	888 Hz	1467 Hz

Table 7.2: Level 1 open trigger efficiencies, combining both geometric and trigger acceptances, for physics benchmark processes and trigger rates. The efficiency denominator includes **all** events generated over the full 4π solid angle (left) and all events within the geometric acceptance (right), respectively. The simulation used 1000 events for each benchmark process.

We also have a "worst-case scenario" for the trigger system since background conditions worse than ×10 compromise data taking in the silicon vertex tracker. We assume a drift chamber cell efficiency of 90% for B Physics and 95% for τ Physics. As pointed out in the previous section, triggering on τ events below 95% cell efficiency becomes challenging. Here we quote two total trigger rates: one includes the regular lost particle beam background, with beam pipe gas pressure ×10 nominal ("Vacuum ×10"), whereas the other assumes that the beam pipe gas pressure is nominal, but that the cross-section for photoproduction is ×10 nominal ("Photoprod. ×11").

Table 7.3 shows efficiencies and rates for these scenarios. The open trigger rates exceed the 2000 Hz limit by an order of magnitude. Thus tighter trigger criteria have to be applied. Here we have selected C_2'+ 2M&1A as a good candidate. The 2M&1A trigger reduces background rates by requiring a coincidence in time between drift chamber tracks and calorimeter clusters; to trigger also on all-neutral events the C_2' trigger is applied. One of the reasons for the success of this trigger line is that not all baryons and other heavy hadrons reach the calorimeter due to dE/dx losses in the DIRC. The open trigger criteria are still active under these conditions but events are collected with a high prescale factor. Note that the 2M&1A trigger is a non-orthogonal trigger criterion.

Trigger Efficiencies for ×10 Background

	4 π			Fiducial volume		
Process	2M&1A	C_2'	C_2'+ 2M&1A	2M&1A	C_2'	C_2'+ 2M&1A
$B^0 \to \pi^+\pi^-$, $\overline{B}^0 \to \mu X$	1.00	0.85	1.00	1.00	0.90	1.00
$B^0 \to D^+D^-$, $\overline{B}^0 \to X$	1.00	0.95	1.00	1.00	0.95	1.00
$B^+ \to \tau^+ \nu$, $B^- \to X$	1.00	0.85	1.00	1.00	0.86	1.00
$\tau^+ \to e^+\nu\bar{\nu}$, $\tau^- \to \mu^-\bar{\nu}\nu$	0.72	0.49	0.73	0.95	0.74	0.95
$\tau^+ \to \pi^+\bar{\nu}$, $\tau^- \to \pi^-\nu$	0.77	0.43	0.77	0.92	0.56	0.92

Trigger Rates for ×10 Background

Process	D_2	C_2	$C_2 + D_2$	2M&1A	C_2'	C_2'+ 2M&1A
Physics Signal	19 Hz	19 Hz	19 Hz	19 Hz	19 Hz	19 Hz
Bhabha	145 Hz	161 Hz	181 Hz	149 Hz	142 Hz	151 Hz
$\gamma\gamma$ Background	50 Hz	50 Hz	50 Hz	$<$ 50 Hz	$<$ 50 Hz	$<$ 50 Hz
Vacuum ×10	8490 Hz	6960 Hz	14790 Hz	1020 Hz	150 Hz	1240 Hz
Photoprod. ×11	6110 Hz	1700 Hz	6640 Hz	1410 Hz	100 Hz	1440 Hz
Beam-gas 50 nTorr	180 Hz	50 Hz	225 Hz	95 Hz	5 Hz	100 Hz
Cosmic Rays	300 Hz	730 Hz	1000 Hz	170 Hz	10 Hz	170 Hz
Vacuum ×10 total	9184 Hz	7970 Hz	16265 Hz	1503 Hz	376 Hz	1730 Hz
Photoprod. ×11 total	6804 Hz	2710 Hz	8115 Hz	1893 Hz	326 Hz	1930 Hz

Table 7.3: Level 1 trigger efficiencies, combining both geometric and trigger acceptances, for physics benchmark processes and trigger rates. The efficiency denominator includes **all** events generated over the full 4π solid angle (left) and all events within the geometric acceptance (right), respectively. The simulation used 1000 events for each benchmark process. Note that the total trigger rate can exceed the sum of the displayed trigger rates of the individual lines because the open trigger still runs with prescale factors applied.

7.3.3 Drift Chamber only under ×10 Background Conditions

In the previous section it was necessary to sacrifice the orthogonality of the drift chamber and calorimeter triggers, and requiring trigger objects in both subsystems, in order to achieve high efficiency with low background rates. The trigger should still be able to record data efficiently when one of the two subsystems does not transmit data to the trigger. Table 7.4 shows a trigger strategy using only drift chamber trigger data. While triggering on B physics is still very efficient, τ physics suffers under these conditions. Obviously any all-neutral physics mode would be lost.

Efficiencies for ×10 Background – Drift Chamber only

	4 π			Fiducial volume		
Process	D$_2'^*$	3A	D$_2'^*$ + 3A	D$_2'^*$	3A	D$_2'^*$ + 3A
$B^0 \rightarrow \pi^+\pi^-$, $\overline{B}^0 \rightarrow \mu$X	0.93	0.91	0.98	0.95	0.95	0.99
$B^0 \rightarrow D^+D^-$, $\overline{B}^0 \rightarrow$ X	0.74	0.99	0.99	0.75	0.99	0.99
$B^+ \rightarrow \ \tau^+ \ \nu$, $B^- \rightarrow \ X$	0.65	0.90	0.95	0.66	0.91	0.95
$\tau^+ \rightarrow e^+\nu\bar{\nu}$, $\tau^- \rightarrow \mu^-\bar{\nu}\nu$	0.58	0.04	0.59	0.82	0.04	0.83
$\tau^+ \rightarrow \pi^+\bar{\nu}$, $\tau^- \rightarrow \pi^-\nu$	0.69	0.13	0.71	0.85	0.14	0.86

Rates for ×10 Background – Drift Chamber only

Process	D$_2'^*$	3A	D$_2'^*$ + 3A
Physics Signal	19 Hz	19 Hz	19 Hz
Bhabha	120 Hz	8 Hz	122 Hz
$\gamma\gamma$ Background	$<$ 50 Hz	$<$ 50 Hz	$<$ 50 Hz
Vacuum ×10	730 Hz	950 Hz	1460 Hz
Photoprod. ×11	780 Hz	1020 Hz	1510 Hz
Beam-gas 50 nTorr	10 Hz	50 Hz	50 Hz
Cosmic Rays	70 Hz	40 Hz	100 Hz
Vacuum ×10 total	999 Hz	1117 Hz	1801 Hz
Photoprod. ×11 total	1049 Hz	1187 Hz	1851 Hz

Table 7.4: Level 1 drift chamber trigger efficiencies, combining both geometric and trigger acceptances, for physics benchmark processes and trigger rates. The efficiency denominator includes **all** events generated over the full 4π solid angle (left) and all events within the geometric acceptance (right), respectively. The simulation used 1000 events for each benchmark process.

7.3.4 Calorimeter only under ×10 Background Conditions

A corresponding scenario assumes that there is no drift chamber data accessible to the trigger. While the trigger efficiency for B physics is still high, trigger efficiency for τ physics drops significantly. Note the low trigger rate for the ×11 background. Most of the trigger rate in the calorimeter is due to coinciding single clusters from electromagnetic interactions of lost beam particles.

Efficiencies for ×10 Background – Calorimeter only

	$4\,\pi$			Fiducial volume		
Process	3M	C'_2	C'_2+ 3M	3M	C'_2	C'_2+ 3M
$B^0 \to \pi^+\pi^-$, $\overline{B}^0 \to \mu X$	0.97	0.85	0.98	0.98	0.90	0.98
$B^0 \to D^+D^-$, $\overline{B}^0 \to X$	0.99	0.95	1.00	0.99	0.95	1.00
$B^+ \to \tau^+ \nu$, $B^- \to X$	0.97	0.85	0.98	0.98	0.86	0.98
$\tau^+ \to e^+\nu\bar{\nu}$, $\tau^- \to \mu^-\bar{\nu}\nu$	0.19	0.49	0.55	0.25	0.74	0.80
$\tau^+ \to \pi^+\bar{\nu}$, $\tau^- \to \pi^-\nu$	0.24	0.42	0.50	0.28	0.56	0.63

Rates for ×10 Background – Calorimeter only

Process	3M	C'_2	C'_2+ 3M
Physics Signal	19 Hz	19 Hz	19 Hz
Bhabha	41 Hz	142 Hz	144 Hz
$\gamma\gamma$ Background	$<$ 50 Hz	$<$ 50 Hz	$<$ 50 Hz
Vacuum ×10	1100 Hz	150 Hz	1170 Hz
Photoprod. ×11	190 Hz	100 Hz	280 Hz
Beam-gas 50 nTorr	20 Hz	5 Hz	20 Hz
Cosmic Rays	110 Hz	10 Hz	110 Hz
Vacuum ×10 total	1340 Hz	376 Hz	1513 Hz
Photoprod. ×11 total	430 Hz	326 Hz	623 Hz

Table 7.5: Level 1 calorimeter trigger efficiencies, combining both geometric and trigger acceptances, for physics benchmark processes and trigger rates. The efficiency denominator includes **all** events generated over the full 4π solid angle (left) and all events within the geometric acceptance (right). The simulation used 1000 events for each benchmark process.

7.3.5 Trigger Efficiencies for $\gamma\gamma$ Modes

In the previous sections we covered B and τ benchmark processes; here we investigate the trigger efficiencies for the two-photon benchmark processes. All requirements are exceeded for both nominal running conditions and ×10 background conditions when both drift chamber and calorimeter contribute data to the trigger.

The first $\gamma\gamma$ benchmark, $\pi^+\pi^-$ production with invariant mass greater than $2\,\mathrm{GeV}/c^2$, has a high trigger efficiency for all scenarios. Moreover, the overlap between calorimeter and drift chamber triggers will allow precise determination of the efficiencies. By contrast, $\pi^0\pi^0$ production relies almost entirely on the calorimeter trigger, and has somewhat lower–although still acceptable–efficiency when the calorimeter trigger is present. The $\gamma\gamma^{(*)}$ benchmark with the $K^\pm K^0_s\pi^\mp$ final state yields high efficiency within the fiducial volume. The final $\gamma\gamma^{(*)}$ benchmark decaying to $\eta(550)$, with decay to the mixed state $\pi^+\pi^-\pi^0$, has a low raw efficiency as expected; within the fiducial acceptance the efficiency is high. Note that only 11 $\eta(550)$ events were in the fiducial acceptance.

7.3.6 A Safer Trigger Criterion Demonstrating Robustness

The trigger strategy introduced in Section 7.3.2 for ×10 background conditions needed no PT discriminator to yield a trigger rate below 2 kHz. For additional background rejection power one could change the 2M&1A trigger criterion to 2M&1A′. This results in a significantly reduced trigger rate, while keeping the trigger efficiencies for the benchmark processes acceptable. Table 7.7 shows the trigger efficiencies and rates for that strategy, illustrating the robustness of the trigger design.

7.4 Event Time Jitter Results

The same simulation and conditions described in Chapter 4 were used to study the event time jitter of the global trigger algorithm. A brief overview of the justification for reducing trigger jitter to levels significantly below the specification, as well as the results for inclusive B and τ decays, are given in this section.

7.4.1 Trigger Jitter and SVT Poisoning

As explained in Section 3.2.3, the specification for latency and jitter only requires that the maximum jitter be no more than $1\,\mu$s. However, there are several motivating factors for reducing the jitter of the trigger significantly below this requirement. The most important of these factors is reducing the poisoning of the silicon vertex tracker hits caused by backgrounds. With $1\,\mu$s of jitter and ×10 background, the single-hit electronics of stave 1 of the silicon vertex tracker will have 30% occupancy leading to a 15% probability of having background hits occurring **before** physics hits, which shadows the physics hit. This figure decreases approximately linearly with the jitter window, as shown in Figure 7.1.

7.4.2 Results for B and τ Physics

Fortunately, the methods described in Section 6.2.5 reduce the jitter to a much smaller time slice, and consequently the SVT poisoning is greatly diminished. In Table 7.8, the jitter results for scenarios of different background levels as previously described are summarized

Trigger Efficiencies for Two-Photon Physics

Nominal Trigger Efficiencies

	$4\ \pi$			Fiducial volume		
Process	D_2	C_2	$\mathrm{C}_2+\mathrm{D}_2$	D_2	C_2	$\mathrm{C}_2+\mathrm{D}_2$
$\gamma\gamma \to \pi^+\pi^-$,	0.83	0.74	0.87	0.98	0.89	0.99
$\gamma\gamma \to \pi^0\pi^0$,	0.07	0.77	0.78	0.07	0.98	0.99
$\gamma\gamma^{(*)} \to X(1420) \to KK\pi$	0.76	0.61	0.87	0.98	0.80	0.99
$\gamma\gamma^{(*)} \to \eta(550) \to \pi^+\pi^-\pi^0$	0.07	0.14	0.21	1.00	1.00	1.00

Trigger Efficiencies for ×10 Background

	$4\ \pi$			Fiducial volume		
Process	2M&1A	C_2'	$\mathrm{C}_2'+$ 2M&1A	2M&1A	C_2'	$\mathrm{C}_2'+$ 2M&1A
$\gamma\gamma \to \pi^+\pi^-$,	0.73	0.27	0.74	0.90	0.30	0.90
$\gamma\gamma \to \pi^0\pi^0$,	0.10	0.65	0.66	0.14	0.99	0.99
$\gamma\gamma^{(*)} \to X(1420) \to KK\pi$	0.56	0.14	0.56	0.80	0.31	0.80
$\gamma\gamma^{(*)} \to \eta(550) \to \pi^+\pi^-\pi^0$	0.07	0.03	0.07	1.00	0.91	1.00

Efficiencies for ×10 Background – Drift Chamber only

	$4\ \pi$			Fiducial volume		
Process	$\mathrm{D}_2'^*$	3A	$\mathrm{D}_2'^*$ + 3A	$\mathrm{D}_2'^*$	3A	$\mathrm{D}_2'^*$ + 3A
$\gamma\gamma \to \pi^+\pi^-$,	0.66	0.14	0.68	0.92	0.14	0.92
$\gamma\gamma \to \pi^0\pi^0$,	0.00	0.01	0.01	0.00	0.01	0.01
$\gamma\gamma^{(*)} \to X(1420) \to KK\pi$	0.19	0.28	0.33	0.41	0.55	0.64
$\gamma\gamma^{(*)} \to \eta(550) \to \pi^+\pi^-\pi^0$	0.03	0.02	0.03	0.91	0.37	0.91

Efficiencies for ×10 Background – Calorimeter only

	$4\ \pi$			Fiducial volume		
Process	3M	C_2'	$\mathrm{C}_2'+$ 3M	3M	C_2'	$\mathrm{C}_2'+$ 3M
$\gamma\gamma \to \pi^+\pi^-$,	0.19	0.27	0.39	0.19	0.30	0.42
$\gamma\gamma \to \pi^0\pi^0$,	0.33	0.65	0.67	0.33	0.99	0.99
$\gamma\gamma^{(*)} \to X(1420) \to KK\pi$	0.29	0.14	0.31	0.48	0.31	0.50
$\gamma\gamma^{(*)} \to \eta(550) \to \pi^+\pi^-\pi^0$	0.04	0.03	0.04	0.91	0.91	1.00

Table 7.6: Level 1 trigger efficiencies, combining both geometric and trigger acceptances, for $\gamma\gamma$ benchmark physics processes. The efficiency denominator includes **all** events generated over the full 4π solid angle (left) and all events within the geometric acceptance (right), respectively. The simulation used 1000 events for each benchmark process. On top the trigger lines for nominal running conditions (with 95% cell efficiency and ×10 background overlayed here) are shown, below are the trigger lines for ×10 background, first using both drift chamber and calorimeter, then only the drift chamber and lastly only the calorimeter. The first two benchmark processes were generated with $\mathrm{W}_{\gamma\gamma} > 2\,\mathrm{GeV}/c^2$.

Efficiencies for ×10 Background – “Safest” Trigger

	$4\ \pi$			Fiducial volume		
Process	2M&1A$'$	C'_2	C'_2+ 2M&1A$'$	2M&1A$'$	C'_2	C'_2+ 2M&1A$'$
$B^0 \to \pi^+\pi^-$, $\overline{B}^0 \to \mu$X	0.93	0.85	0.99	0.95	0.90	1.00
$B^0 \to D^+D^-$, $\overline{B}^0 \to$ X	0.74	0.95	0.99	0.75	0.95	0.99
$B^+ \to \tau^+ \nu$,$B^- \to X$	0.65	0.85	0.96	0.66	0.86	0.96
$\tau^+ \to e^+\nu\bar{\nu}$, $\tau^- \to \mu^-\bar{\nu}\nu$	0.58	0.49	0.63	0.82	0.74	0.88
$\tau^+ \to \pi^+\bar{\nu}$, $\tau^- \to \pi^-\nu$	0.66	0.43	0.71	0.84	0.56	0.88
$\gamma\gamma \to \pi^+\pi^-$,	0.59	0.27	0.63	0.84	0.30	0.86
$\gamma\gamma \to \pi^0\pi^0$,	0.01	0.65	0.65	0.01	0.99	0.99
$\gamma\gamma^{(*)} \to X(1420) \to KK\pi$	0.18	0.14	0.21	0.42	0.31	0.43
$\gamma\gamma^{(*)} \to \eta(550) \to \pi^+\pi^-\pi^0$	0.03	0.03	0.03	1.00	0.91	1.00

Rates for ×10 Background – “Safest” Trigger

Process	2M&1A$'$	C'_2	C'_2+ 2M&1A$'$
Physics Signal	19 Hz	19 Hz	19 Hz
Bhabha	131 Hz	142 Hz	147 Hz
$\gamma\gamma$ Background	$<$ 50 Hz	$<$ 50 Hz	$<$ 50 Hz
Vacuum ×10	220 Hz	150 Hz	370 Hz
Photoprod. ×11	450 Hz	100 Hz	520 Hz
Beam-gas 50 nTorr	3 Hz	5 Hz	$<$ 8 Hz
Cosmic Rays	20 Hz	10 Hz	$<$ 30 Hz
Vacuum ×10 total	443 Hz	376 Hz	624 Hz
Photoprod. ×11 total	673 Hz	326 Hz	774 Hz

Table 7.7: Level 1 “safest” trigger efficiencies, combining both geometric and trigger acceptances, for physics benchmark processes and trigger rates. The efficiency denominator includes **all** events generated over the full 4π solid angle (left) and all events within the geometric acceptance (right), respectively. The simulation used 1000 events for each benchmark process.

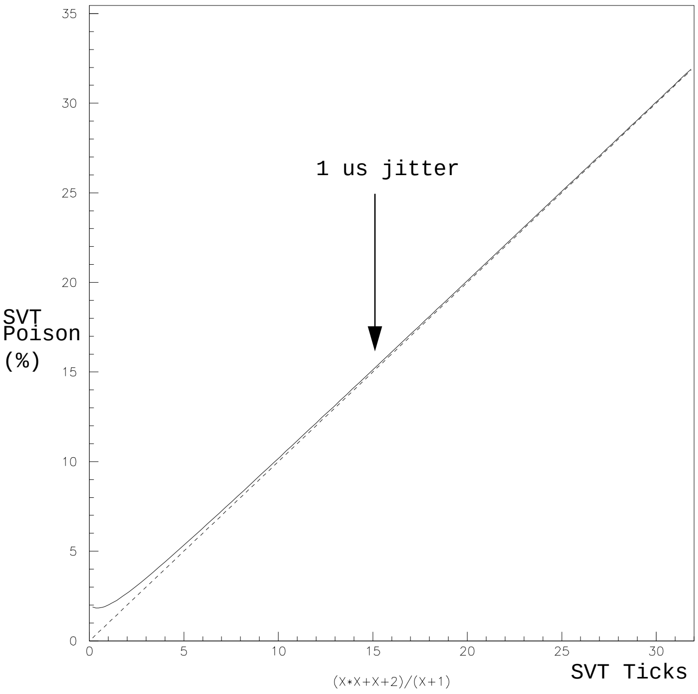

Figure 7.1: SVT hit poisoning in stave 1 under ×10 background conditions, as a function of the trigger jitter window, in units of SVT ticks at 15 MHz.

for inclusive $B^0\overline{B}^0$ and $\tau^+\tau^-$ events. Note that even at ×10 background and 90% cell efficiency, we still achieve a jitter of only 181 ns[1] for inclusive $B^0\overline{B}^0$ events, as shown in Figure 7.2. A small jitter directly leads to higher statistical $B^0\overline{B}^0$ *CP* reach under bad running conditions, by lowering the inefficiency due to hit poisoning in the SVT. A jitter of 181 ns, compared to 1 μs, reduces the hit poisoning in stave 1 of the SVT from 15% to 3% under ×10 background conditions. For τ physics, high efficiency in SVT layer 1 is not as crucial as for $B^0\overline{B}^0$ *CP* physics that requires excellent vertexing.

For the $\tau^+\tau^-$ events, approximately 1% of the triggers were due to background events, close in time to the physics event. These give a skewed time distribution, producing outlying estimated times and thus a worse 99% confidence level. A 98% confidence level, as shown in Figure 7.3, is more representative of the true jitter of the trigger for $\tau^+\tau^-$ events.

Another effect producing outlying estimated times are triggers due to background, where the physics event itself would not trigger. $B^0\overline{B}^0$ events with their relatively larger multiplicity, suffer less from these effects. In Table 7.9, the jitter results for two lines from the drift chamber and two lines from the calorimeter are shown. Note that the drift chamber produces the better results, and that higher-multiplicity lines do better than lines with lower multiplicities.

---

[1] The event time jitter quoted here deviates slightly from [Gehrig 96c] because **all** triggered events contribute here, whereas a few outlying events were neglected in [Gehrig 96c].

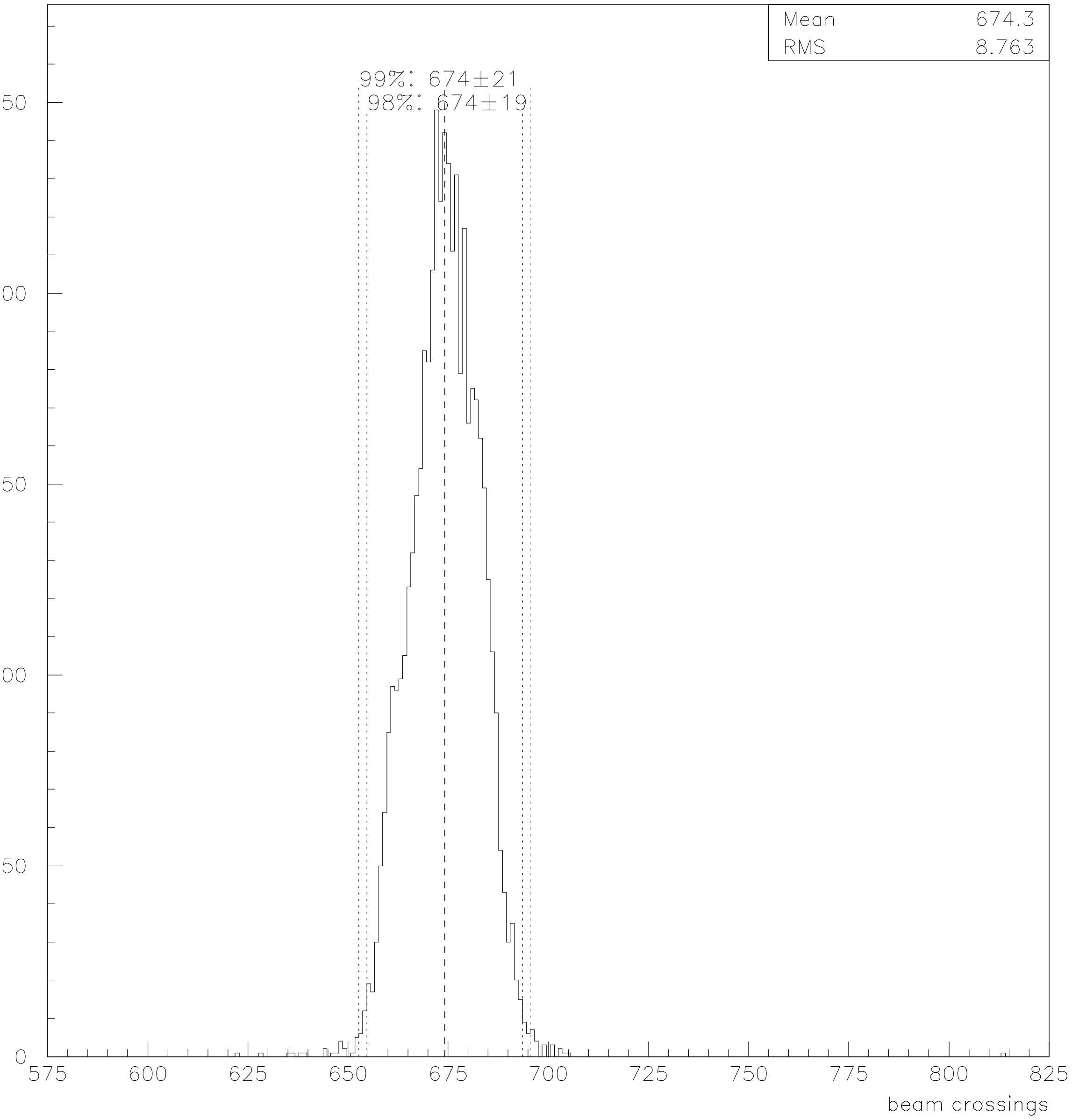

Figure 7.2: Event time jitter distribution for 5000 $B\overline{B} \rightarrow X$ events, at 90% cell efficiency, ×10 background, with both the drift chamber and the calorimeter running. Note that the RMS and confidence intervals are in beam crossings (1 BX = 4.2 ns). Occasional outlying event times are triggers due to a background event close in time to the physics event. No fiducial cuts were made.

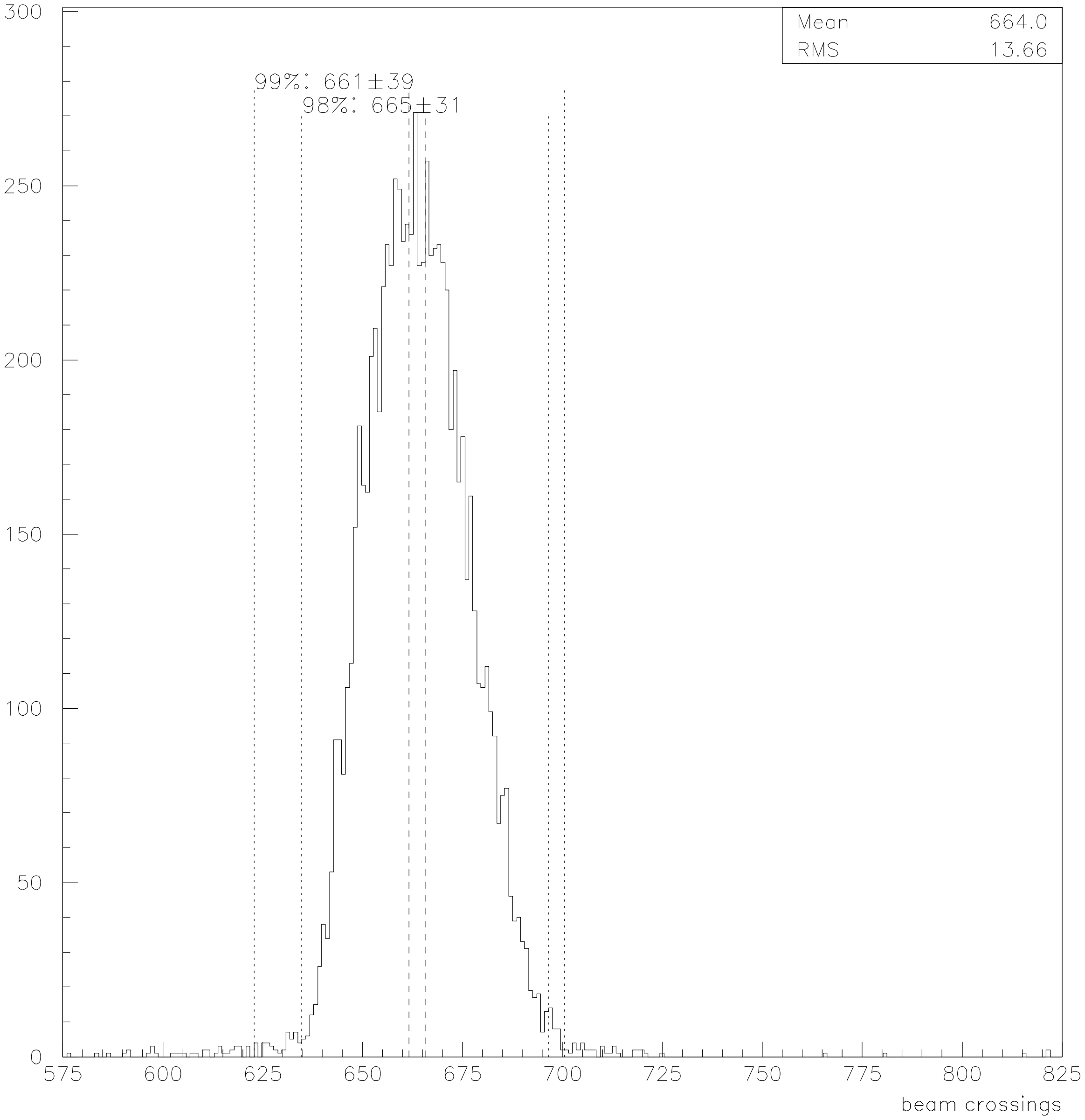

Figure 7.3: Event time jitter distribution for 10000 $\tau^+\tau^- \to X$ events, at 95% cell efficiency, ×10 background, with both the drift chamber and the calorimeter running. Note that the RMS and confidence intervals are in beam crossings (1 BX = 4.2 ns). Many of the outlying event times are triggers due to a background event close in time to the physics event. No fiducial cuts were made.

$B\overline{B} \to X$

Conditions				Jitter (ns)		
Background	Detectors	Cell Efficiency	Main Trigger	98% conf.	99% conf.	RMS
nominal	DC and EM	99% Cell Eff.	$C_2 + D_2$	147	164	34
×10	DC and EM	90% Cell Eff.	C_2'+ 2M&1A	164	181	37
×10	DC only	90% Cell Eff.	$D_2'^*$ + 3A	164	176	39
×10	EM only	N/A	C_2'+ 3M	210	235	42

$\tau^+\tau^- \to X$

Conditions				Jitter (ns)		
Background	Detectors	Cell Efficiency	Main Trigger	98% conf.	99% conf.	RMS
nominal	DC and EM	99% Cell Eff.	$C_2 + D_2$	223	248	50
×10	DC and EM	95% Cell Eff.	C_2'+ 2M&1A	273	340	57
×10	DC only	95% Cell Eff.	$D_2'^*$ + 3A	231	261	60
×10	EM only	N/A	C_2'+ 3M	311	378	57

Table 7.8: Level 1 trigger jitter. These data were taken from runs of 5000 ($B\overline{B}$) or 10000 ($\tau^+\tau^-$) events each. No fiducial cuts were made. Note that the "DC only" and "EM only" jitter statistics contain fewer events (only events that trigger the respective detector), and thus can have a smaller jitter window due to reduced efficiency. Note also that "Main Trigger" denotes the trigger line that was not prescaled, and thus was the trigger which ensured the high efficiency with low background rates. However, all trigger lines listed in Table 3.4 contributed to the time jitter results through the trigger line prioritizing logic shown in Figure 6.1, unless trigger data for these lines were missing.

$B\overline{B} \to X$

Conditions			Jitter (ns)	
Background	Cell Efficiency	Main Trigger	99% confidence	RMS
nominal	99% Cell Eff.	D_2	193	37
nominal	99% Cell Eff.	3A	160	34
nominal	N/A	C_2	197	39
nominal	N/A	3M	185	35
×10	90% Cell Eff.	D_2	235	54
×10	90% Cell Eff.	3A	172	39
×10	N/A	C_2	298	51
×10	N/A	3M	227	40

Table 7.9: Level 1 trigger jitter for individual lines which constitute part of a global trigger algorithm. These lines (and others) are `OR`-ed together. The data were taken from runs of 5000 ($B\overline{B}$) events each. No fiducial cuts were made.

Chapter 8

Conclusions

The simulation results presented in this thesis show that the current BaBar Level 1 trigger design meets all physics requirements, except for the physics benchmark process $\tau^+ \to \pi^+\bar{\nu}$, $\tau^- \to \pi^-\nu$ under worst-case running conditions (92% instead of 95% trigger efficiency). The total trigger rates for all scenarios shown are below the 2 kHz limit imposed by the limited data acquisition bandwidth. Note that the Level 1 global trigger strategies shown here are **not** final, e.g. the 2M&1A trigger could be replaced with a trigger like 1G&D'_2 + 1M&3A, which showed very good background rejection power in preliminary studies while keeping physics efficiencies very high. The programmable nature of the trigger design allows any adaptation to the trigger strategy, even on a run-by-run basis (see Chapter 6).

The event time estimate of the Level 1 trigger is also well within the 1 μs requirement, which enables the data acquisition system to read out the complete data belonging to an event from the detector buffers.

In addition, all parts of the Level 1 drift chamber trigger were studied, exploring the parameter spectrum of these algorithms. Many of these parameters for the drift chamber trigger are programmable and could be adjusted to adapt to changing conditions, like in the Level 1 global trigger.

The electronics implementation of the Level 1 trigger presented here is currently in progress at Lawrence Berkeley National Laboratory and in England. Preliminary functional descriptions can be found in [Jared 96].

Trigger strategy issues including the existence of a Level 2 trigger and the choice of algorithms in the Level 3 trigger will be refined when background data become available at the PEP-II collider ring.

Appendix A

Uses of Segment Finder Data in Level 3

A.1 Primary Vertex Cuts using Level 1 Segments

The ϕ position resolution of the segment patterns is shown in Figure 5.5. Typically, the position resolution is about 0.05 drift cell widths which is equivalent to 1mm. Using the position information of the stereo superlayers and taking the stereo angle and the rotation of the layers into account, one can calculate the track vertex of tracks traversing the whole drift chamber to an RMS of about 3 cm in z [Kral 96b]. Since the main background sources usually originate 20 cm off the interaction point (see Section 4.2.4), a good means of background discrimination is available.

A.2 Event Time Algorithm

One of the main functions of the trigger system is to determine the event time. A more refined event time determination in the Level 3 trigger is beneficial because independent background events close in time to physics events can be better separated. Also the speed of algorithms in Level 3 is often proportional to the event time jitter (see e.g. [Grace 95]), since most hits in an event under bad background conditions are from beam-induced occupancy.

A.2.1 Inverse Sigma Squared

From the calibration of the segment pattern addresses (Section 5.2.3) there is information available on the average (t_i) and the standard deviation (σ) of the latency of every commonly occurring segment pattern address. The average latency is the time span that passed between the true event time and the time when the segment pattern occurred in the drift chamber trigger, as measured in beam crossings. We use σ as a measure of the quality of the time information encoded in a segment. To determine the tick with the most time information, we evaluate $\sum_{i=1}^{n} \frac{1}{\sigma_i^2}$ every tick, where n is the number of segments. When this sum reaches a local maximum value, we have identified the tick with the most time information available.

A.2.2 Weighted Latency Method

In Section 5.2.3 some segment addresses were shown to have a very small latency uncertainty. These segments contain the best time information. We could simply subtract the average latencies for these pattern addresses from the current time to determine the event time. However, in our algorithm we have chosen to use the information available from **all** segments, using a weighted average latency,

$$\overline{T} = \frac{\sum\limits_{i=1}^{n} t_i \cdot \frac{1}{\sigma_i^2}}{\sum\limits_{i=1}^{n} \frac{1}{\sigma_i^2}}, \tag{A.1}$$

where $\overline{T}$ denotes the weighted latency. By allowing all occurring segments[1] to contribute, we ensure that this method is quite robust against accidental background hits that might produce event-unrelated segments. This sum could be evaluated at every tick for all segments occurring at that tick. The best estimate is typically evaluated at the tick with the most time information available (see previous section); this is what we use in measuring the event time.

Figure A.1 shows the time evolution for the quantities described above of a typical $\tau^+\tau^-$ event (see Figure 5.3). Note that priority encoding and centering is used. This displaces all the segment-related information to higher tick numbers than the related hits.

Evaluating Equation A.1 involves a sum of multiplications. To facilitate the multiplications when using this algorithm as a possible upgrade to the Level 1 trigger, one can digitize σ logarithmically, which turns the multiplications into simple bit shifting operations that are ideal for hardware implementation. A digitization scheme with the inverse squared weights $2^0, 2^1, ..., 2^7$ (three bits) and the average latencies $0, 8, 16, ..., 255$ (five bits) could be used to pass information to the algorithm. The calibration table stores the average latencies in units of beam crossings. Negligible event time resolution is lost compared to using 32-bit floating-point operations. It is advantageous to set a saturation point, assigning the largest possible weight to all segment pattern addresses that have a σ of less than seven beam crossings. Patterns with a higher value of σ are appropriately assigned smaller weights.

A.3 Performance of the Event Time Algorithm

This section describes results of the algorithm introduced above. First a verification of the calibration is done and a test on single tracks is performed. Then results of the event time jitter of $B^0\overline{B}^0$ events and $\tau^+\tau^-$ events are presented.

---

[1] There are at least 12 segments in events that satisfy the open trigger condition.

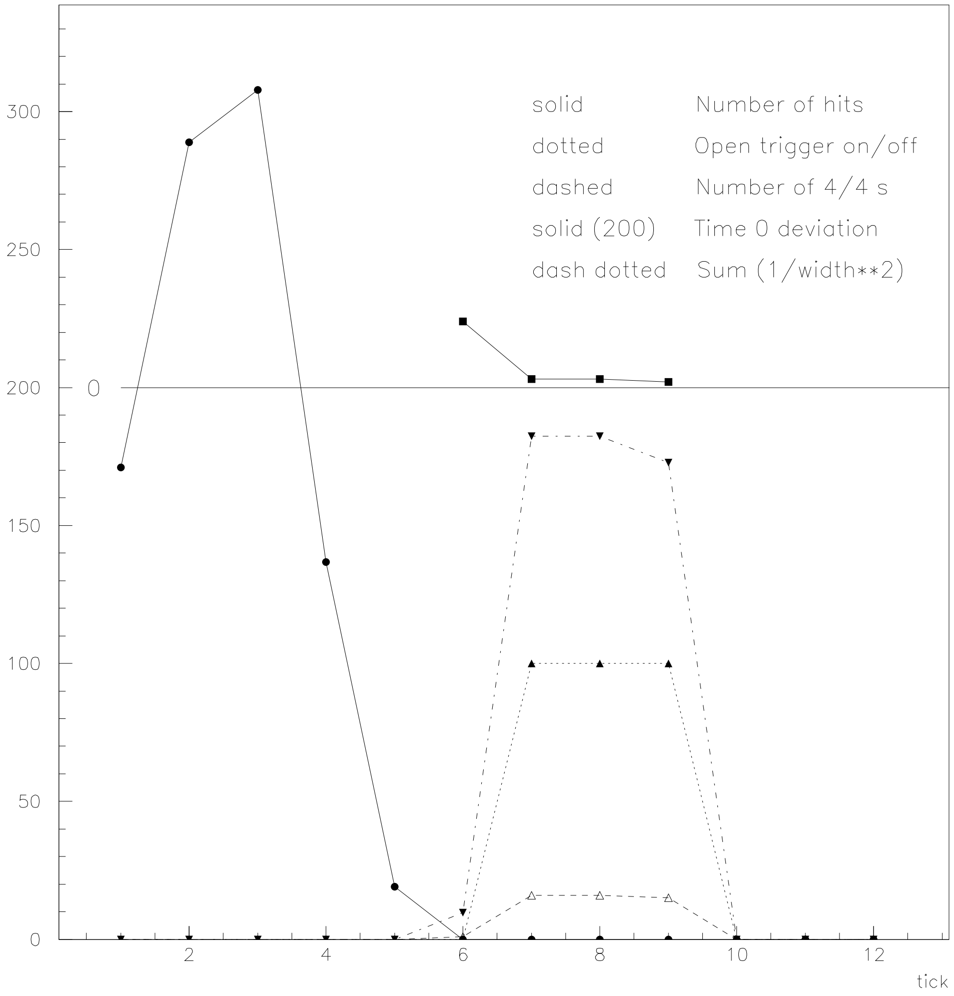

Figure A.1: Tick histogram for a typical $\tau^+\tau^-$ event like the one shown in Figure 5.3. The y-axis shows the number of hits times 3.8 (solid with circles), the number of segments times 1 (dashed) and the inverse sigma squared sum times 0.015 (dash dotted). The trigger decision is set to 100 for trigger on and to 0 for trigger off (dotted). The event time estimate is calculated in units of beam crossings for every 269 nstick and offset by 200 (solid with squares). Note that the event time estimates at tick 7, 8 and 9 are acceptable, indicating that the algorithm is quite robust against uncertainties in the choice of the best tick.

A.3.1 Verification of the Event Time Algorithm

The event time algorithm depends on the quality of the calibrated segment finder data. To verify the statistical distribution of the calibrated data we calculated the χ^2 per degree of freedom for every event. As expected the average number was approximately 1, indicating that the calibrated values of σ were properly normalized.

In addition, we investigated the event time algorithm running on a different sample of 25000 single-muon events from the sample used to fill the segment finder calibration tables. The timing results in this section show an offset of about 4 beam crossings from beam crossing 0 where the event takes place. This is due to the fact that the calibration took all segments into account for calibration, whereas real events are composed of priority encoded segments. The event time jitter is not affected by this offset.

When requiring a minimum number of segments, e.g. the four which are necessary to produce a B track, the resolution of the event time estimate was roughly independent of the transverse momentum p_{t} and the angle between the track and the beam line, θ. Figure A.2 shows the time jitter versus p_{t} and $\cos\theta$. It shows that one single track can be used to determine the event time to an RMS of 17 ns. This is an accurate and minimally biased way to ensure a small event time jitter for any type of event that contains silicon vertex tracker information.

A.3.2 Results

It is desirable for the event time determination algorithm to produce measurements that are as insensitive to the type of event as possible. However, using any realistic algorithm, it is unavoidable that the means and widths of the distributions of measured event times differ for different data samples. To investigate the effect of different physics event topologies on the algorithm, inclusive $\tau^+\tau^-$ and $B^0\overline{B}^0$ events were used in the performance studies.

The more segments in the drift chamber, the better the time estimate. Hence $B^0\overline{B}^0$ events yield a better time determination than $\tau^+\tau^-$ events since $\tau^+\tau^-$ events are dominated by 2-prong topologies whereas B events of interest always contain three or more tracks. We evaluated the performance with the segment finder running at 3.7 MHz and the rest of the trigger running at 7.4 MHz.

Figure A.3 shows the distribution of reconstructed event time for $B^0\overline{B}^0$ events and $\tau^+\tau^-$ events for nominal running conditions (99% cell efficiency, nominal background). The time jitters at 98%, 99% and 99.5% confidence levels, the RMS, and the width of a Gaussian fit are listed in Table A.1. As expected, $B^0\overline{B}^0$ events have smaller time jitters than $\tau^+\tau^-$ events.

The effect of drift chamber cell inefficiency on event time determination was studied in [Gehrig 96b]. A comparison between the RMS of the event time measured for inclusive $\tau^+\tau^-$ events with 95% cell efficiency and the RMS with 100% cell efficiency showed that there is a degradation of about 10% in the inefficient case. This effect is even less apparent

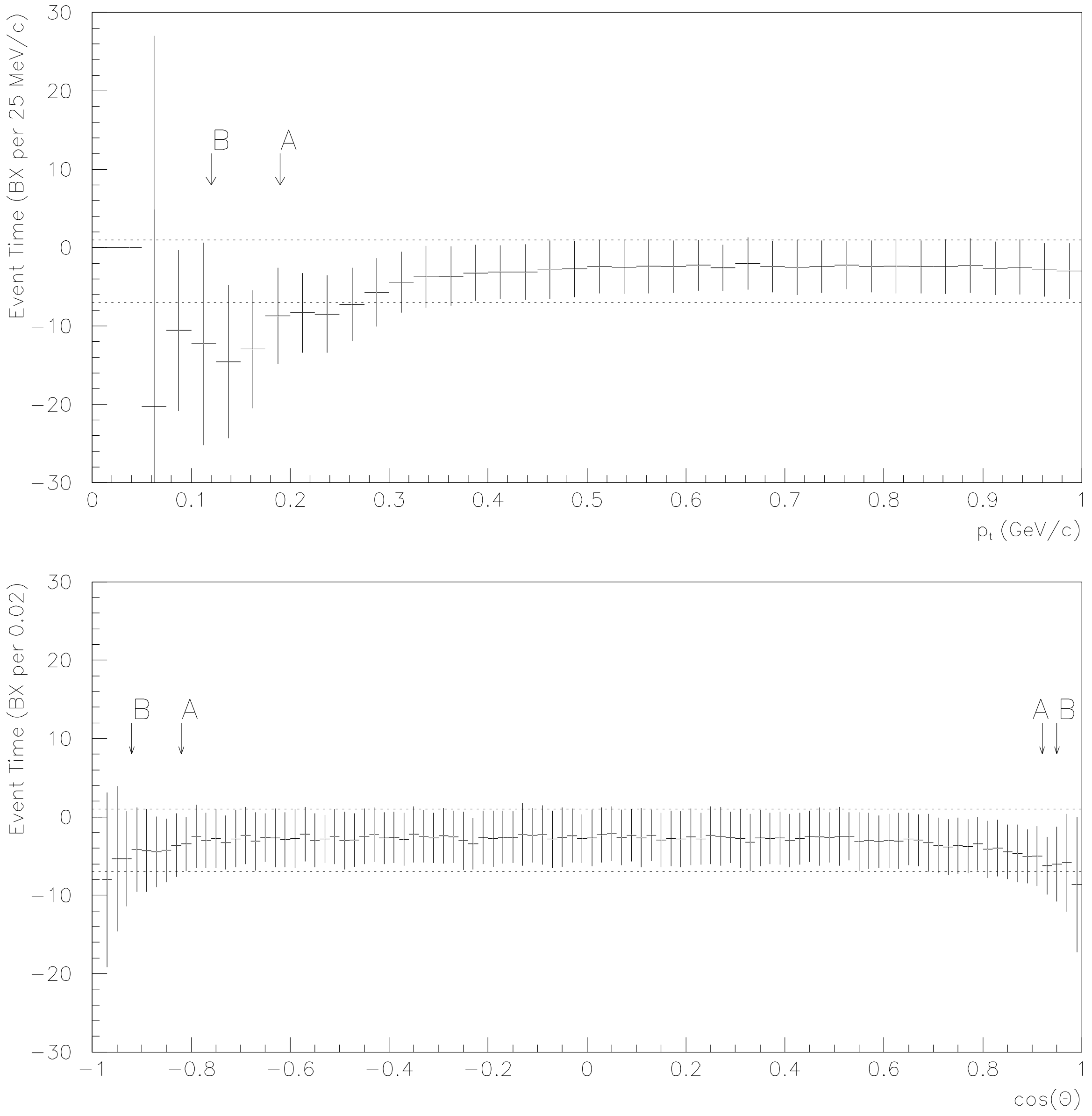

Figure A.2: Event time determination for single-muon events. 100% cell efficiency is assumed. One beam crossing is equivalent to 4.2 ns. The top graph shows event time estimate versus p_t, the bottom graph shows event time estimate versus $\cos\theta$. The error bars indicate the RMS. The arrows in the graphs show the fiducial acceptance limits ($>$ 95% efficiency) for A tracks and B tracks, respectively. 25000 single-muon events were generated over the full 4π solid angle, with uniform distributions in p_t, ϕ, and $\cos\theta$. The dotted horizontal lines indicate an RMS of 16 ns.

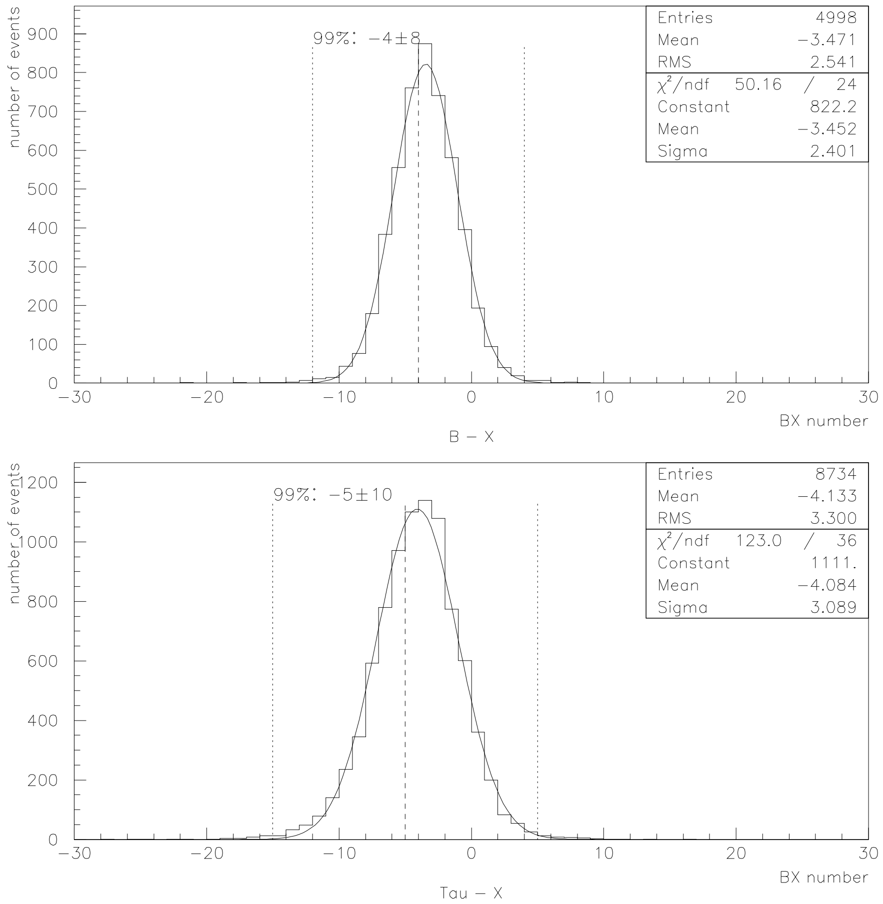

Figure A.3: Event Time Measurement for $B^0\overline{B}^0$ events (top) and $\tau^+\tau^-$ events (bottom) under nominal running conditions. One beam crossing is equivalent to 4.2 ns. 5000 $B^0\overline{B}^0$ events and 10000 $\tau^+\tau^-$ events were generated over the full 4π solid angle. Two of the $B^0\overline{B}^0$ events and 1266 of the $\tau^+\tau^-$ events failed the open drift chamber trigger. The dotted vertical lines indicate the 99% confidence limits, centered at the dashed line, not including nine $\tau^+\tau^-$ events outside the 60 beam crossing window.

Time jitter (98% confidence level)	$B^0 \to$ X, $\overline{B}^0 \to$ X	$\tau^+ \to$ X,$\tau^- \to$ X
nominal background	55 ns	71 ns
×10 background	76 ns	109 ns

Time jitter (99% confidence level)	$B^0 \to$ X, $\overline{B}^0 \to$ X	$\tau^+ \to$ X,$\tau^- \to$ X
nominal background	67 ns	84 ns
×10 background	88 ns	172 ns

Time jitter (99.5% confidence level)	$B^0 \to$ X, $\overline{B}^0 \to$ X	$\tau^+ \to$ X,$\tau^- \to$ X
nominal background	80 ns	101 ns
×10 background	109 ns	609 ns

RMS	$B^0 \to$ X, $\overline{B}^0 \to$ X	$\tau^+ \to$ X,$\tau^- \to$ X
nominal background	11 ns	27 ns
×10 background	14 ns	64 ns

Width from Gaussian fit	$B^0 \to$ X, $\overline{B}^0 \to$ X	$\tau^+ \to$ X,$\tau^- \to$ X
nominal background	10 ns	18 ns
×10 background	13 ns	19 ns

Table A.1: Time jitter at the 98%, 99% and 99.5% confidence level, RMS and width of a Gaussian fit for $B^0\overline{B}^0$ and $\tau^+\tau^-$ events. 5000 $B^0\overline{B}^0$ events were generated and 10000 $\tau^+\tau^-$ events were generated. The distributions are shown in Figures A.3 and A.4. **All** events that satisfied the open drift chamber trigger contributed.

for $B^0\overline{B}^0$ events (higher multiplicity). When well-calibrated segments are missing due to inefficient drift chamber cells, there is a sufficient amount of segment data per event, even in low-multiplicity events, to reconstruct event times with adequate resolution.

The mixing of background on top of the physics event has an impact on the event time determination since additional segments with wrong time information are produced. Figure A.4 shows event time determination results for worst-case running conditions (90% cell efficiency for $B^0\overline{B}^0$ events, 95% for $\tau^+\tau^-$ events, both with ×10 background). The differences of Figures A.3 and A.4 are mainly due to background. All studies shown here required segments to be part of a track. Event time determination of $B^0\overline{B}^0$ events is not much affected by background. For $\tau^+\tau^-$ events, on the other hand, additional tracks from a background event can lead to a skewed event time determination. Extremely outlying event times can be produced if a background event is close in time to the $\tau^+\tau^-$ event but has a higher multiplicity. Also, background events overlayed with a $\tau^+\tau^-$ event that does not trigger by itself also contribute to the confidence levels quoted above. Hence the 98% confidence level for $\tau^+\tau^-$ events at ×10 background is more representative for the true jitter than the 99% confidence level.

The time jitters at 98%, 99% and 99.5% confidence levels, the RMS, and the width of a Gaussian fit for ×10 background conditions are listed in Table A.1.

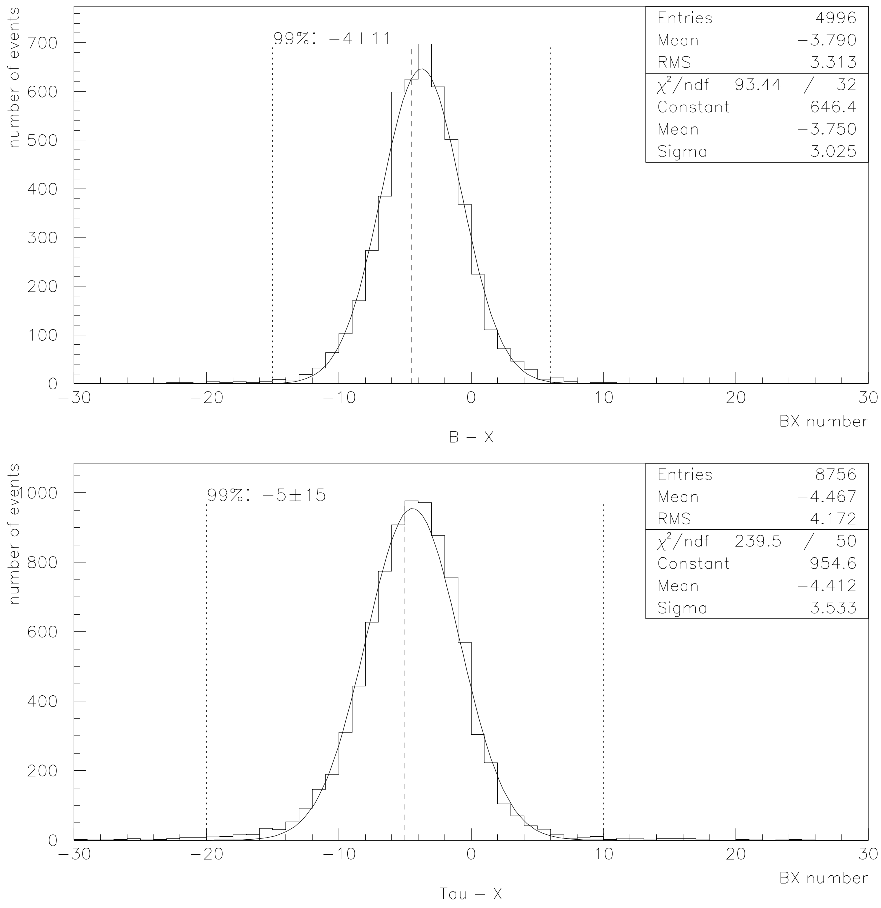

Figure A.4: Event Time Measurement for $B^0\overline{B}^0$ events (top) and $\tau^+\tau^-$ events (bottom) under worst-case running conditions. One beam crossing is equivalent to 4.2 ns. 5000 $B^0\overline{B}^0$ events and 10000 $\tau^+\tau^-$ events were generated over the full 4π solid angle. Four of the $B^0\overline{B}^0$ events and 1244 of the $\tau^+\tau^-$ events failed the open drift chamber trigger, where at least 22 events were triggers due to background and 61 events fell outside the 60 beam crossing window. The dotted vertical lines indicate the 99% confidence limits, centered at the dashed line, **not** including the events outside the 60 beam crossing window.

Bibliography

[BELLE 95] The BELLE Collaboration, M. T. Cheng et al., Technical Design Report, KEK-Report95-1, April 1995.

[BBSIM 96] Software Release Tools, Version 1.1.2, August 1996, contains BEGET, the event generator, and BBSIM, the GEANT model of the *BaBar* detector [TDR 95].

[Burchat 91] P. R. Burchat, "Physics at an Asymmetric-Energy B Meson Factory," *BaBar Note* # 68, June 1991.

[Butler 96] J. N. Butler, D. Quarrie, *Physics Today*, **Vol. 49 No. 10** (1996) 50.

[CERN 95] GEANT Detector Description and Simulation Tool, Version 3.21, CERN Program Library, CERN (1995)

[Chiam 95] K. H. Chiam, J. F. Kral, "Determination of Event Time in the Level 1 Drift Chamber Trigger," *BaBar Note* # 250, September 1995.

[Christenson 64] J. H. Christenson, J. W. Cronin, V. L. Fitch, R. Turlay, *Phys. Rev. Lett.* **13** (1964) 138.

[CLEO 91] The CLEO II Collaboration, C. Bebek et al., *Nucl. Instr. Methods* **A302** (1991) 261.

[Dauncey 96a] P. D. Dauncey, "Status of EM Studies", http://www.slac.stanford.edu/BFROOT/doc/Trigger/96/dauncey-studies-aug27/, August 1996.

[Dauncey 96b] P. D. Dauncey, J. G. Dowdell, D. Price, "*BaBar* Calorimeter Level 1 Trigger Prototype Design," http://www.slac.stanford.edu/BFROOT/doc/Trigger/96/Workshop/, October 1996. This is a draft of a forthcoming *BaBar* note.

[Gehrig 96a] S. K. Gehrig and J. F. Kral, "Impact of Cell Inefficiencies on Drift Chamber Trigger Track Finding and PT Discrimination," *BaBar Note* # 314, July 1996.

[Gehrig 96b] S. K. Gehrig, R. C. Jared, J. F. Kral, M. E. Levi, A. H. Montgomery, "Measuring Event Time to an RMS of 10 ns using Drift Chamber Segments," *BaBar Note* # 319, August 1996.

[Gehrig 96c] S. K. Gehrig, J. F. Kral, A. H. Montgomery, "Level 1 Global Trigger Efficiency, Rate and Event Time Jitter," *BaBar Note* # 338, December 1996.

[Gheri 95] A. Gheri, M. G. Pia, "Comparison of GEANT Physics Hadronic Packages," *BaBar Note* # 305, July 1995.

[Grace 95] C. Grace, M. Levi, "A Fast Silicon Vertex Detector Software Trigger Algorithm," *BaBar Note* # 265, September 1995.

[H1 92] The H1 Collaboration, Th. Wolff et al., *Nucl. Instr. Methods* **A323** (1992) 537.

[Innes 96] W. Innes, "Efficiency and Time vs. Distance in the *BaBar* Drift Chamber," *BaBar Note* # 329, October 1996.

[Jared 96] R. C. Jared, K. M. Marks, F. A. Kirsten, J. F. Kral, S. K. Gehrig, A. H. Montgomery, "*BaBar* Level 1 Trigger Implementation Model," http://www.slac.stanford.edu/BFROOT/doc/Trigger/96/Workshop/, October 1996. This is a draft.

[Kinoshita 89] K. Kinoshita, *Nucl. Instr. Methods* **A276** (1989) 242.

[Kral 94a] F. Kral, "GEANT Simulation Results for a Fast Calorimeter Trigger," *BaBar Note* # 133, April 1994.

[Kral 94b] J. F. Kral and D. Worledge, "Initial Design and GEANT Simulation of a Fast Drift Chamber Trigger," *BaBar Note* # 162, September 1994.

[Kral 96a] J. F. Kral, "Level 1 Latency and Jitter", http://www.slac.stanford.edu/BFROOT/doc/Trigger/96/latency-jitter/, September 1996.

[Kral 96b] J. F. Kral, S. Schaffner "Reconstructed Z0 from Level 1 Segments for Single Muons", http://www.slac.stanford.edu/BFROOT/doc/Trigger/96/, September 1996.

[Levi 94] M. Levi, "Obituary for the Prompt Silicon Trigger," Netnews Item *slac.b-factory.vertex #54*, (1994).

[Lynch 89] G. R. Lynch, "Review of *dE/dx* for Particle Identification", Proceedings of the Symposium on Particle Identification at High Luminosity Hadron Colliders April 5 – 7 (pp. 485), FNAL, April 1989.

[MAC 87] The MAC Collaboration, E. Fernandez et al., *Phys. Rev. Lett.* **51** (1987) 1022.

[Nir 92a] Y. Nir, “CP Violation,” SLAC–PUB–5874, September 1992.

[Nir 92b] Y. Nir, H. R. Quinn, *Ann. Rev. Nucl. Science* **42** (1992) 211.

[PDG 96] The Particle Data Group, “Particles and Fields,” *Phys. Rev. D*, **D54**, July 1996.

[Ronan 96] M. T. Ronan, personal communication

[SLAC 93] “Status Report on the Design of a Detector for the Study of *CP* Violation at PEP-II at SLAC,” SLAC–419 (1993).

[SRT 96] Software Release Tools, Version 1.2.3, October 1996, contains the *BaBar* simulation software.

[TDR 95] The *BaBar* Collaboration, D. Boutigny et al., Technical Design Report, SLAC–R–95–457, March 1995.

[trgDC 96a] trgDC, Version V00-01-39, June 1996, a simulation of the *BaBar* drift chamber trigger, used together with Software Release Tools version 1.0.0.

[trgDC 96b] trgDC, Version TIW-03-08, November 1996, a simulation of the *BaBar* drift chamber trigger, used together with Software Release Tools version 1.2.3 [SRT 96].

[trgEM 96] trgEM, Version tag FcsSim, November 1996, a simulation of the *BaBar* calorimeter trigger, used together with Software Release Tools version 1.2.3 [SRT 96].

[trgFrame 96] trgFrame, Version V00-02-01, September 1996, a simulation of the *BaBar* Level 1 trigger, used together with Software Release Tools version 1.2.3 [SRT 96].

[Trigger 96] The Trigger Group, “*BaBar* Level 1 Trigger Design Requirements,” February 1996.

[UA1 87] The UA1 Collaboration, C. Albajar et al., *Phys. Rev. Lett.* **186B** (1987) 247.

[ZEUS 92] The ZEUS Collaboration, G. P. Heath et al., *Nucl. Instr. Methods* **A315** (1992) 431.